To the Graduate Council:

I am submitting herewith a dissertation written by Myvizhi Esai Selvan entitled "Molecular-Level Modeling of Proton Transport in Aqueous Systems and Polymer Electrolyte Membranes: A Reactive Molecular Dynamics Study." I have examined the final electronic copy of this dissertation for form and content and recommend that it be accepted in partial fulfillment of the requirements for the degree of Doctor of Philosophy, with a major in Chemical Engineering.

David J. Keffer
Major Professor

Stephen J. Paddison
Major Professor

We have read this dissertation
and recommend its acceptance:

Brian J. Edwards

Shengting Cui

Jimmy Mays

Accepted for the Council:

Carolyn R. Hodges
Vice Provost and Dean of the Graduate School

(Original signatures are on file with official student records.)

# MOLECULAR-LEVEL MODELING OF PROTON TRANSPORT IN AQUEOUS SYSTEMS AND POLYMER ELECTROLYTE MEMBRANES: A REACTIVE MOLECULAR DYNAMICS STUDY

A Dissertation
Presented for the
Doctor of Philosophy
Degree
The University of Tennessee, Knoxville

Myvizhi Esai Selvan
December 2010

# Dedication

*To my Father*

## Acknowledgements

I wish to thank my advisor, Dr. David Keffer for his great guidance, continual support, and invaluable advice. His enthusiasm and tireless encouragement played an important role in helping me meet the requirements of my Doctor of Philosophy degree. I would also like to thank my co-advisors, Dr. Stephen Paddison and Dr. Edwards for their unique ideas that helped me on many occasions to overcome stumbling blocks in my research. Their participation in the research provided a thought provoking environment. I express special thanks to Dr. Shengting Cui for his active participation, support, and insightful feedback at various stages of this research. I sincerely thank all the above for providing a wonderful learning experience and opportunity to work with them. I express my gratitude to Dr. Jimmy Mays for serving on my committee. I also wish to express my gratitude to the department administrative assistants, Ms. Lori Daniels and Ms. Cristina Wilson, for their sincerely kind help in dealing with any official matter. Finally, I greatly appreciate the support and encouragement from my family and friends.

# Abstract

Proton exchange membrane (PEM) fuel cells are an eco-friendly power source that has great potential to reduce our oil dependence for our stationary and transportation applications. In order to make PEM fuel cells an economically viable option, further effort is needed to improve proton conduction under wide operating conditions and reduce the cost of production. Design and synthesis of novel membranes that have superior characteristics require a fundamental molecular-level understanding of the relationship between the polymer chemistry, water content and proton conduction. The performance of a fuel cell is influenced by the electrochemical and molecular/proton transport processes that occur at the catalytic sites in the electrode/electrolyte interface. Therefore, understanding the molecular-level details of proton transport and structure of the multi-phase interfaces is critical.

This work is subdivided into two main tasks. The first task is to model membrane/water vapor interfaces and to study their morphology and the transport properties of water and hydronium ions. Classical molecular dynamics simulation is used as the modeling tool for the characterization of the interface. The second task is to model proton transport through the aqueous domains of PEM. Such a model is inherently challenging since proton transport occurs through a combination of structural and vehicular diffusions that are associated with disparate time scales. Toward this end, we have developed and implemented a new reactive molecular dynamics algorithm to model the structural diffusion of proton that involves breaking and forming of covalent bonds. The proton transport through aqueous channels in PEM is governed by acidity and confinement. Therefore, systems in which the acidity and confinement can be independently varied, including bulk water, aqueous hydrochloric acid solutions and water confined in carbon nanotubes are also examined in addition to the application in PEM.

We have developed an understanding of how acidity and confinement independently impact proton transport. The correlation between the two components of charge diffusion and their contribution to the total charge diffusion has also been explored for a basic understanding of the proton transport mechanisms. These studies will eventually help us establish the correlation between the morphology of the membrane and proton conduction.

# Table of Contents

# List of Tables

**Chapter 5**

# List of Figures

**Chapter 3**

**Chapter 4**

**Chapter 5**

# CHAPTER 1

# Introduction

Compared to conventional methods of power generation, fuel cells that produce electric power via electrochemical reaction attract great interest because of their high conversion efficiency and zero carbon emissions [1]. A fuel cell in its simplest form consists of an electrolyte placed between an anode and cathode. Classification of the fuel cells are based on the type of electrolyte employed since they define the type of chemical reactions that take place, catalyst, operational temperature range and other critical factors which in turn dictate the potential applications and limitations of the fuel cell [2]. Of various existing fuel cell systems, the proton exchange membrane (PEM) fuel cell is considered as the most promising power source for stationary, vehicular and portable power applications due to their low operating temperature (< 80 °C) range, quick start up time, low sensitivity to orientation and high-power density that makes them compact and light weight [3,4]. In a PEM fuel cell, the fuel (usually $H_2$/$CH_3OH$) is catalytically oxidized (dissociates into protons and electrons) at the anode and the oxidant is catalytically reduced (combines with protons and electrons) at the cathode. While separating the two electrodes, the polymer electrolyte membrane also provides the structural framework of the cell and serves as a transport medium for the protons from anode to cathode while the electrons are forced to induce a current through an external circuit. Though the PEM fuel cell shows great potential to replace fossil fuels, from a commercialization point of view tremendous effort is required in improving the cost, water and heat management, durability, conductivity, and high operational temperature. Therefore, an ideal PEM is expected to have mechanical strength, thermo and chemical stability, long term durability, high ionic conductivity at extreme operating conditions of low humidity or high temperature, and low cost of production. No existing membranes satisfy all the above characteristics. Perfluorosulfonic acid (PFSA) membranes are currently the most popular electrolyte because of their chemical inertness, low relative permittivity, and high selectivity and Nafion, a PFSA membrane developed and produced by the E. I. Dupont Company is employed as an industrial standard electrolyte [5].

A PFSA membrane has a perfluorinated backbone and side chains terminated with charged end groups (usually $SO_3H$). Presence of water is essential for the PEM fuel cell operation and proton conduction. When hydrated, the morphology of the membrane undergoes spontaneous nanoscale segregation into two phases: hydrophobic matrix (perfluorinated backbone) and a hydrophilic region. The hydrophilic domains that consist of water, protons

(dissociated from sulfonic acid groups upon sufficient water uptake) and pendant side chains are responsible for the conduction of protons from anode to the cathode. While extensive research has been done to understand the hydrated membrane morphology using phenomenological approaches [6,7] based on experimental findings, atomistic modeling [8-12], and mesoscale modeling [13-15] the precise morphology of the membrane at molecular-level has not been definitely characterized and continues to be the subject of intense debate. Based on the aqueous domain shape, size, and connectivity several morphological models have been proposed: spherical inverted-micelle water clusters [16], layered structures [17], channel networks [18,19], polymer bundles [20], and parallel water channels in cylindrical inverted micelles [21]. A combination of results from the experimental studies at macro/micro-scale and simulation at molecular level would enable the exact characterization of the morphology of the membrane. The morphology (size, shape and connectivity) of the hydrophilic regions which governs the proton conduction is highly dependent on the polymer architecture [8,22-24] and water content [9,25-27].

The water distribution defined in terms of size and shape of the hydrophilic regions is important because it dictates the degree of confinement and concentration of the ions within the domains. In addition, they contribute to the formation of a continuous path for proton conduction based on water uptake [18]. Locally, the proton transport in an aqueous system is affected by the presence of anions [28,29] and confinement [30-33] while the overall conductance of the fuel cell is also dependent on the connectivity of the clusters [34,35]. In larger clusters, there may be a core of water molecules that enables the diffusion of protons by a mechanism similar to that of bulk water, while in smaller clusters or more elongated clusters, the protons are in close proximity to the hydrophobic/hydrophilic interface and the presence of $SO_3^-$ modifies the proton conduction mechanism. In general, proton conductivity is found to increase with water content [36] but at high hydration level excess of water can flood the catalyst and porous transport layers impeding the transport of fuel to the catalyst.

To overcome the short-comings of Dupont's Nafion such as high production cost and narrow operating conditions, other PFSA membranes including Asahi Glass's Flemion, Asahi Kasei's Aciplex, Dow's short side-chain (SSC) PFSA membrane (now manufactured by Solvay Solexis as Aquivion), 3M PFSA membrane and many more novel membranes have been

synthesized [37,38]. The polymer chemistry of these membranes differs from each other. The polymer structure or chemistry determined by the equivalent weight , molecular weight, length of the side-chain and aromatic or heterocyclic groups can affect the morphology of the membrane, water uptake and performance of the fuel cell [8,15,23,39,40].

Therefore, a fundamental molecular-level understanding of the correlation between the polymer architecture, water distribution, and proton transport is needed for the design of novel PEMs with superior performance and for improving the efficiency and/or operating range of PEM fuel cells. In addition to characterizing the morphology of membrane based on water content and polymer chemistry, it is also important to discern how this morphology changes at the interface of the electrolyte with the electrode. Optimizing the PEM fuel cells conduction involves molecular-scale understanding of structure and proton/molecular transport across the electrode/electrolyte interface because the electrochemical; electrocatalytical phenomena at these interfaces are related the performance of membrane electrode assembly (MEA) [41]. Typical MEA in a PEM fuel cell consists of an electrolyte membrane sandwiched between two gas diffusion layers and two catalyst layers where the catalyst (Pt or Pt-based alloy supported on carbon) is deposited on either the electrode or the PEM. The nanoscale structure of the electrode/electrolyte interface is a function of the manufacturing process and composition of catalyst zone and can lead to a variety of two- or three-phase interfaces such as PEM/vapor, PEM/water, PEM/catalyst, and PEM/catalyst/support depending on the area of observation and water content. When the catalyst particle has interfaces with three phases namely, $H_2$ gas phase, solid phase of the support and the hydrated ionomer phase, the particle would be effectively utilized by participating in three transport functions: (i) adsorbing gaseous $H_2$, (2) conducting electrons through the catalyst support, and (3) conductting the protons via the hydrated ionomer. Thus the ultimate performance of a fuel cell is controlled by the nature of two- and three-phase interfaces present within the catalyst layer [42].

In this work, we have studied the hydrated membrane/water vapor interface and analyzed the dynamical properties of $H_2O$ and $H_3O^+$ ions through MD simulations. Although the above interface does not actively influence the conduction of protons from the anode to the electrolyte, we can use it to identify the presence of any resistance to the transport of $H_2O$ and $H_3O^+$ ions across the interface and understand the morphology of the membrane.

Protons play a vital role in energy transfer in PEM fuel cells and other areas such as acid-base reactions [43] or enzymatic catalysis [44,45] because of their anomalously high mobility compared to other cations of similar size in aqueous media [46]. Proton diffusion in bulk water occurs through a combination of vehicular diffusion (conventional mass diffusion) and structural diffusion (displacement of proton along a network of hydrogen-bonded water molecules) [47,48]. The structural diffusion or Grotthuss mechanism involves continual transformation between the structures of Zundel cation (proton shared between two water molecules) and Eigen cation (hydronium ion surrounded by three water molecules) accompanied by the reorganization of the hydrogen-bonded network. While significant progress has been made toward understanding the proton transport mechanism in bulk water [49], our knowledge is considerably less when it comes to proton transport through aqueous domains in PFSA membrane. The aqueous domains differ from the bulk water by the confinement into domains that are only a few nanometers in dimension and by the acidity of the protogenic groups. Due to the inability of experiments to capture molecular level details of proton transport within a complex heterogeneous system, we have to rely on modeling studies to accurately describe the process.

Molecular-level modeling of proton transport has been reviewed by Elliott and Paddison [50]. Electronic structure calculations [51,52], nonequilibrium statistical models [53,54], *ab initio* molecular dynamics [55,56] and meta-dynamics [57], empirical valence bond (EVB) models [11,12,58], and Q-HOP MD [34] have been applied to study the proton dissociation, proton diffusion rates, and proton transport. Classical MD simulation [23,27,59,60] has also been applied to proton dynamics but the protons are allowed to undergo only vehicular diffusion as $H_3O^+$ ions.

In this work, we have developed a novel reactive molecular dynamics (RMD) algorithm to model the proton transport through the hydrophilic domains of a PEM in a classical MD simulation. The algorithm was validated by reproducing the transport property of protons at various temperatures by fitting the reaction kinetics in bulk water to experimental values. The individual effects of confinement and acidity on the structural diffusion of protons were investigated by applying it to aqueous hydrochloric acid (HCl) solutions and water confined in carbon nanotubes (CNT), respectively, before implementing the algorithm into the proton

transport through the confined and highly acidic aqueous domains in a PEM. Correlation between the two mechanisms of proton transport and their contribution to the overall proton conductivity has been investigated. This leads to the initial stage of gaining knowledge of the structure-transport relationship. In summary, two main tasks are focused here. Chapter 2 discusses the structural and dynamical properties in a membrane/water vapor interface. The development and applications of the RMD algorithm to (i) water, (ii) aqueous HCl, (iii) water confined in CNTs, and (iv) PEM are presented in Chapters 3-5. The dissertation is organized as described below

In Chapter 2, the structural and dynamical behavior of $H_2O$ and $H_3O^+$ ions at the membrane/vapor interface in the MEA of a PEM fuel cell are investigated at various water contents via classical MD simulations. The objective of the work is to determine if there is any resistance to the mass transport of $H_2O$ and $H_3O^+$ ions across the membrane/vapor interface. Nafion is the PFSA PEM studied here, since it is the most widely studied and archetypal membrane used in fuel cells. A theory is developed and employed to determine the perpendicular and parallel components of the vehicular diffusivity of $H_2O$ and $H_3O^+$ ions in the interfacial region. The entire system is divided into four regions namely (i) membrane, (ii) membrane side interface, (iii) vapor side interface, and (iv) bulk vapor to capture the individual effect of each region on the structural and transport properties. The structural measurements such as radial distribution function, $H_3O^+$ ion hydration histograms, $H_3O^+$ ion orientation at the interface, and density distribution functions are examined at different hydration levels in all the regions. Additionally, this study also lays ground work for the application of RMD algorithm in future to understand the actual process involved in the transport of proton across the interfacial regions in the MEA.

In Chapter 3, a novel RMD algorithm to model structural diffusion of proton in aqueous systems as a chemical reaction is presented. The algorithm implements reactivity in classical MD simulations by three steps (i) satisfaction of the trigger, (ii) instantaneous reaction (iii) local equilibration. Triggers are used to check whether the reactants are in a reactive configuration and they are defined based on the transition state and ground state structures of the reactants and products. Local equilibration is done to get the correct ending configuration of products after the instantaneous reaction and to satisfy the heat of reaction of the considered reaction. The triggers

in the algorithm are parameterized to fit the rate constant of the structural diffusion proton transport in bulk water and later extended to an aqueous HCl system. In bulk water, the rate constant for the proton transfer reaction, water diffusion coefficients, the total charge diffusion coefficient and its decomposition into structural and vehicular components are examined as functions of temperature. The sensitivity of the method to its environment has been studied by applying the algorithm to aqueous HCl solutions and by calculating the total charge diffusion as a function of molarity. In short, this work confirms the validity of the algorithm and its adaptability to physical conditions (temperature) and other environmental factors (pH).

In Chapter 4, proton transport through water confined in CNTs of varying radii at infinite dilution is investigated by means of classical MD simulations with the structural diffusion modeled by the RMD algorithm parameterized for bulk water. The effect of confinement within CNTs on the physical (radial density profile, orientation) and transport properties (diffusion coefficients, reaction rate) of the proton and water are discussed as functions of CNT radius. The RMD scheme successfully captured the essential features of the structural diffusion under confinement (increase in structural diffusion with decrease in confinement).

In Chapter 5, the dynamical properties of water and protons in Nafion are studied using the recently developed RMD algorithm at various water contents. The structural diffusion of a proton along the aqueous domains is modeled via a mechanism similar to that observed in bulk aqueous systems. The algorithm demonstrated capability to qualitatively capture the transport properties of water and protons in complex system whose aqueous regions are influenced by both acidity and confinement.

Finally, in Chapter 6, the main conclusions from each work described in this dissertation are summarized and an overall impact of the current achievement is discussed.

# References

[1] Song, C. S., *Catal. Today* **77**, 17 (2002).

[2] Steele, B. C. H. and Heinzel, A., *Nature* **414**, 345 (2001).

[3] Gottesfeld, S. and Zawodzinski, T. A., Polymer Electrolyte Fuel Cells in: *Adv. Electrochem. Sci. Eng.*, Wiley VCH, Weinheim, 1997, p. 195.

[4] Mehta, V. and Cooper, J. S., *J. Power Sources* **114**, 32 (2003).

[5] Mauritz, K. A. and Moore, R. B., *Chem. Rev.* **104**, 4535 (2004).

[6] Hsu, W. Y. and Gierke, T. D., *J. Membr. Sci.* **13**, 307 (1983).

[7] Yarusso, D. J. and Cooper, S. L., *Macromolecules* **16**, 1871 (1983).

[8] Jang, S. S.; Molinero, V.; Cagin, T. and Goddard, W. A., *J. Phys. Chem. B* **108**, 3149 (2004).

[9] Urata, S.; Irisawa, J.; Takada, A.; Shinoda, W.; Tsuzuki, S. and Mikami, M., *J. Phys. Chem. B* **109**, 4269 (2005).

[10] Vishnyakov, A. and Neimark, A. V., *J. Phys. Chem. B* **105**, 9586 (2001).

[11] Spohr, E.; Commer, P. and Kornyshev, A. A., *J. Phys. Chem. B* **106**, 10560 (2002).

[12] Petersen, M. K. and Voth, G. A., *J. Phys. Chem. B* **110**, 18594 (2006).

[13] Mologin, D. A.; Khalatur, P. G. and Kholhlov, A. R., *Macromol. Theory Simul.* **11**, 587 (2002).

[14] Yamamoto, S. and Hyodo, S. A., *Polym. J.* **35**, 519 (2003).

[15] Wu, D. S.; Paddison, S. J.; Elliott, J. A. and Hamrock, S. J., *Langmuir* **26**, 14308 (2010).

[16] Gierke, T. D.; Munn, G. E. and Wilson, F. C., *J. Polym. Sci. Polym. Phys. Edn* **19**, 1687 (1981).

[17] Starkweather, H. W., *Macromolecules* **15**, 320 (1982).

[18] Kreuer, K. D.; Paddison, S. J.; Spohr, E. and Schuster, M., *Chem. Rev.* **104**, 4637 (2004).

[19] Kim, M. H.; Glinka, C. J.; Grot, S. A. and Grot, W. G., *Macromolecules* **39**, 4775 (2006).

[20] Rubatat, L.; Rollet, A. L.; Gebel, G. and Diat, O., *Macromolecules* **35**, 4050 (2002).

[21] Schmidt-Rohr, K. and Chen, Q., *Nat. Mater.* **7**, 75 (2008).

[22] Hristov, I. H.; Paddison, S. J. and Paul, R., *J. Phys. Chem. B* **112**, 2937 (2008).

[23] Liu, J. W.; Suraweera, N.; Keffer, D. J.; Cui, S. T. and Paddison, S. J., *J. Phys. Chem. C* **114**, 11279 (2010).

[24] Kreuer, K. D., *J. Membr. Sci.* **185**, 29 (2001).

[25] Cui, S. T.; Liu, J. W.; Esai Selvan, M.; Keffer, D. J.; Edwards, B. J. and Steele, W. V., *J. Phys. Chem. B* **111**, 2208 (2007).

[26] Fujimura, M.; Hashimoto, T. and Kawai, H., *Macromolecules* **14**, 1309 (1981).

[27] Devanathan, R.; Venkatnathan, A. and Dupuis, M., *J. Phys. Chem. B* **111**, 8069 (2007).

[28] Esai Selvan, M.; Keffer, D. J.; Cui, S. T. and Paddison, S. J., *J. Phys. Chem. C* **114**, 11965 (2010).

[29] Dippel, T. and Kreuer, K. D., *Solid State Ionics* **46**, 3 (1991).

[30] Mann, D. J. and Halls, M. D., *Phys. Rev. Lett.* **90**, 4 (2003).

[31] Esai Selvan, M.; Keffer, D. J.; Cui, S. and Paddison, S. J., *Mol. Sim.* **36**, 568 (2010).

[32] Brewer, M. L.; Schmitt, U. W. and Voth, G. A., *Biophys. J.* **80**, 1691 (2001).

[33] Dellago, C.; Naor, M. M. and Hummer, G., *Phys. Rev. Lett.* **90**, (2003).

[34] Devanathan, R.; Venkatnathan, A.; Rousseau, R.; Dupuis, M.; Frigato, T.; Gu, W. and Helms, V., *J. Chem. Phys. B* **114**, (2010).

[35] Costamagna, P.; Grosso, S. and Di Felice, R., *J. Power Sources* **178**, 537 (2008).

[36] Kreuer, K. D., *Solid State Ionics* **97**, 1 (1997).

[37] Souzy, R. and Ameduri, B., *Prog. Polym. Sci.* **30**, 644 (2005).

[38] Hamrock, S. J. and Yandrasits, M. A., *Polym. Rev.* **46**, 219 (2006).

[39] Paddison, S. J. and Elliott, J. A., *J. Phys. Chem. A* **109**, 7583 (2005).

[40] Jalani, N. H. and Datta, R., *J. Membr. Sci.* **264**, 167 (2005).

[41] Marr, C. and Li, X. G., *J. Power Sources* **77**, 17 (1999).

[42] Scherer, G. G., *Solid State Ionics* **94**, 249 (1997).

[43] Eigen, M., *Angew. Chem. infernat. Edit* **3**, 1 (1964).

[44] Warshel, A., *Biochemistry* **20**, 3167 (1981).

[45] Braun-Sand, S.; Strajbl, M. and Warshel, A., *Biophys. J.* **87**, 2221 (2004).

[46] Robinson, R. A. and Stokes, R. H., *Electrolyte Solutions*, Butterworths, London (1959).

[47] Agmon, N., *Chem. Phys. Lett.* **244**, 456 (1995).

[48] Tuckerman, M.; Laasonen, K.; Sprik, M. and Parrinello, M., *J. Chem. Phys.* **103**, 150 (1995).

[49] Markovitch, O.; Chen, H.; Izvekov, S.; Paesani, F.; Voth, G. A. and Agmon, N., *J. Phys. Chem. B* **112**, 9456 (2008).

[50] Elliott, J. A. and Paddison, S. J., *Phys. Chem. Chem. Phys.* **9**, 2602 (2007).

[51] Paddison, S. J., *J. New Mater. Electrochem. Syst.* **4**, 197 (2001).

[52] Eikerling, M.; Paddison, S. J. and Zawodzinski, T. A. J., *J. New Mater. Electrochem. Sys.* **5**, 15 (2002).

[53] Eikerling, M.; Kornyshev, A. A.; Kuznetsov, A. M.; Ulstrup, J. and Walbran, S., *J. Phys. Chem. B* **105**, 3646 (2001).

[54] Paddison, S. J.; Paul, R. and Zawodzinski, T. A., *J. Chem. Phys.* **115**, 7753 (2001).

[55] Roudgar, A.; Narasimachary, S. P. and Eikerling, M., *Chem. Phys. Lett.* **457**, 337 (2008).

[56] Choe, Y. K.; Tsuchida, E.; Ikeshoji, T.; Yamakawa, S. and Hyodo, S., *Phys. Chem. Chem. Phys.* **11**, 3892 (2009).

[57] Glezakou, V. A.; Dupuis, M. and Mundy, C. J., *Phys. Chem. Chem. Phys.* **9**, 5752 (2007).

[58] Seeliger, D.; Hartnig, C. and Spohr, E., *Electrochim. Acta* **50**, 4234 (2005).

[59] Elliott, J. A.; Hanna, S.; Elliott, A. M. S. and Cooley, G. E., *Phys. Chem. Chem. Phys.* **1**, 4855 (1999).

[60] Brandell, D.; Karo, J.; Liivat, A. and Thomas, J. O., *J. Mol. Model.* **13**, 1039 (2007).

# CHAPTER 2

## Molecular Dynamics Study of Structure and Transport of Water and Hydronium Ions at the Membrane/Vapor Interface of Nafion

This chapter is a slightly revised version of a paper by the same title published in the *Journal of Physical Chemistry C* in 2008 by Myvizhi Esai Selvan, Junwu Liu, David J. Keffer, Shengting Cui, Brian J. Edwards, and William V. Steele:

Esai Selvan, M.; Liu, J.; Keffer, D. J.; Cui, S. T.; Edwards, B. J.; and Steele, W. V., "Molecular dynamics study of structure and transport of water and hydronium ions at the membrane/vapor interface of Nafion", *J. Phys. Chem. C* **112**, 1975 (2008).

The use of "we" in this part refers to the co-authors and the author of this dissertation. My primary contributions to this paper include (1) all of the simulation work (2) analysis of data, and (3) most of the writing



**Abstract**

Through the use of molecular dynamics simulation, we examine the structural and transport properties of water and hydronium ions at the interface of a Nafion polymer electrolyte membrane and a vapor phase. The effect of humidity was studied by examining water contents of 5%, 10%, 15%, and 20% by weight. We observe a region of water depletion in the membrane near the vapor interface. We report the vehicular diffusion of hydronium ions and water as components parallel and perpendicular to the interface. In the interfacial region, for hydronium ions, we find that the component of the vehicular diffusivity parallel to the interface is largely unchanged from that in the bulk hydrated membrane, but the component perpendicular to the interface has increased, due to local decrease in density. We find similar behavior with water in the interfacial region. On the basis of these diffusivities, we conclude that there is no observable additional resistance to mass transport of the vehicular component of water and hydronium ions due to the interface. In terms of structure at the interface, we find that there is a decrease in the fraction of fully hydrated hydronium ions. This translates into a lower probability of forming Eigen ions, which are necessary for structural diffusion. Finally, we observe that the hydronium ions display a preferential orientation at the interface with their oxygen atoms exposed to the vapor phase.

## 2.1 INTRODUCTION

In order to have a well-founded scientific basis for fuel cell design, one would benefit from a molecular-level understanding of the transport processes governing the movement of hydrogen, oxygen, water, and protons in the fuel cell [1]. Perhaps one of the least understood molecular-level process in the fuel cell involves the catalyst particle [2,3]. On the anode, the particle must participate in three transport functions: (1) adsorbing molecular hydrogen, (2) conducting electrons to the electrode via the catalyst support, and (3) transport of protons into the hydrated polymer electrolyte membrane (PEM). If the molecular hydrogen arrives in the vapor phase within a pore of the electrode, then the catalyst particle must have interfaces with three phases: the vapor phase, the solid phase of the support, and the hydrated membrane phase.

The nanoscale structure of the electrode/electrolyte interface is a function of the manufacturing process, including the amount of recast Nafion used in the electrode and the manner in which the catalyst particles are deposited. In Figure 2.1, we present an idealized graphic representing a small portion of the membrane electrode assembly (MEA) at the interface of the electrode and the PEM. In this graphic, molecular hydrogen diffuses in the vapor phase through a pore in the midst of the carbon support. We can identify four subsystems of interest in terms of proton transport: (1) the "bulk" hydrated PEM, (2) the membrane/vapor interface, (3) the membrane/vapor/support interface, and (4) the membrane/vapor/catalyst interface. The geometry of the schematic in Figure 2.1 is certainly idealized, but the presence of the four systems containing the PEM is relevant, regardless of the larger scale geometry.

There has been significant progress toward understanding the proton transport mechanism within the bulk hydrated membrane (region 1 in Figure 2.1) from experiment [4-6], molecular-level simulation [1,7-28], and macroscopic models [29-31]. What has emerged from this body of work is a partial understanding that the Grotthuss mechanism responsible for structural diffusion of protons is perturbed within the confined and highly acidic environment of a proton exchange membrane. This understanding is not as yet sufficiently developed to allow for the theoretical prediction of the relationship between proton conductivity and polymer electrolyte architecture.

The other three regions in Figure 2.1 have received substantially less attention [32]. While there are modeling studies describing the water transport phenomena in the gas diffusion

layer (GDL), catalyst layer (CL) and PEM [33,34], they do not provide a molecular-level mechanism for proton transport. In this work, we focus on a description of the membrane/vapor interface, examining structural and transport properties. We model Nafion because it is the prototypical PEM used in fuel cells. Our objective is to determine if there is intrinsic resistance to mass transport of water and hydronium ions across the membrane/vapor interface. A complementary molecular dynamics study of regions 3 and 4 in Figure 2.1 is currently under review [35].

The remainder of the paper is organized as follows. In Sec. 2.2, we review the theory we employ to determine perpendicular and parallel components of vehicular diffusivity of water and hydronium in the interfacial region. Sec. 2.3, describes our model parameters and simulation technique. In Sec. 2.4, we present our results and discussion of the structural and transport properties of water and protons at the membrane/vapor interface. Finally, we summarize our conclusions in Sec. 2.5.

## 2.2 INTERFACIAL DIFFUSIVITIES

The measurement of the self-diffusivities of components in mixtures via equilibrium molecular dynamics (MD) simulation is a standard procedure when the mixture is homogeneous [36,37]. Based on the theory of time correlation functions [38,39], one can write expressions for the self-diffusivity in terms of a Green-Kubo velocity auto-correlation function (VACF) or equivalently using the Einstein relation in terms of the mean square displacement (MSD). In a mixture, we understand that the self-diffusivity corresponds not to a pure component property, but rather to a gradient-free asymptote; i.e., where each component has a distinct self-diffusivity which is a function of the thermodynamic state, including composition [40]. Through the Darken equation [41], one can relate self-diffusivities to Fickian diffusivities, which can be used in macroscopic transport equations that describe mass transfer. There are advantages to obtaining the self-diffusivity in MD, primarily due to the fact that it is a single-particle correlation function (as opposed to the Fickian diffusivity, which is an all-particle correlation function). Consequently, these can be obtained with far greater statistical reliability [42]. If proper care is taken to ensure that the same reference frame is applied to diffusion in the molecular simulation

and the macroscopic model, then the diffusivities obtained from MD are immediately applicable at the coarser scale [43].

The measurement of self-diffusivities in a heterogeneous system deserves separate treatment. Before we begin, we should clearly define when we shall consider a system homogeneous or heterogeneous. There are two distinct phases in hydrated Nafion: a hydrophobic phase composed of the polymer backbones; and a hydrophilic phase consisting of hydrated sulfonic acid groups bound to the end of the polymer side chains, hydrated protons and water. Our previous simulation of the bulk hydrated Nafion [14] shows morphology of a tortuous aqueous nanonetwork distributed within the polymer. This system is heterogeneous at the nanoscale. However, the water molecules are considered to be located exclusively in the hydrophilic phase. Therefore, from the point of view of a water molecule, there is only one phase, deformed into a dynamic morphology by a region of inaccessible volume. As a result, in this work we can treat the bulk hydrated membrane as a homogeneous system with respect to the transport properties of the water molecules and hydronium ions.

When we introduce a microscopic interface between the PEM and a vapor phase, a water molecule can reside in a variety of environments ranging from the aqueous component of the bulk membrane, through the interface and into the bulk vapor. This environment changes sharply but continuously. For simplification of description, we shall consider this system to be composed of three regions: (1) bulk membrane, (2) interface, and (3) bulk vapor.

An instantaneous property like the density distribution can be straightforwardly determined from an MD simulation by knowledge of the instantaneous position of each particle. Therefore, with relative ease one can generate densities of water in each of the phases, bulk membrane, interface, and bulk vapor. However, a time correlation function, which relies on trajectories evolving over time, cannot unambiguously be assigned to a particular region of the system. The trajectory of a single particle can move through various regions. If one uses either the VACF or MSD to compute the self-diffusivity, one is required to examine the behavior in the infinite time limit. Because particles can move between phases before this limit is reached, one cannot obtain region-specific self-diffusivities, unless one limits the analysis to molecules that spend the entire duration of the simulation in a single phase; however, this amounts to throwing away the information from many of the particles in the simulation. In Figure 2.2, we provide a conceptual

example of a trajectory that moves through many phases without reaching the infinite-time limit in any one individually. Certainly, one can use the conventionally VACF or MSD to obtain the self-diffusivity of the total system, averaged over all regions.

In this work, we rely on the knowledge of the behavior of transport properties in series and in parallel. In Figure 2.3, we show a schematic of a system with a planar interface. The three phases, bulk membrane (BM), interface (I), and bulk vapor (BV), present three resistances to mass transport, which are in series in the z dimension and which are in parallel in the x and y dimensions.

We begin the analysis with Fick's law for a binary, isothermal system with variation in one-dimension,

$$j_{\mathrm{A}} = -\rho D \frac{\mathrm{d}w_{\mathrm{A}}}{\mathrm{d}z} \tag{1}$$

where $j_{\mathrm{A}}$ is the diffusive mass flux of component A relative to the center-of-mass motion of the system, $\rho$ is the mass density, $w_{\mathrm{A}}$ is the mass fraction of component A, $z$ is the spatial coordinate, and $D$ is the diffusivity. For the binary case, under the assumptions listed above, there is only one diffusivity, $D = D_{\mathrm{A}} = D_{\mathrm{B}}$.

In the case of mass transfer in parallel, $\mathrm{d}w_{\mathrm{A}}/\mathrm{d}z$ the driving force is the same in each region as there can be no mass accumulation in any region at steady state and also each region shares a common boundary with the other (i.e. the final boundary of the bulk membrane is the initial boundary of the interface). If we write Eq. (1) for each of the three phases, as well as for the total system (T), and equate the gradients, we have

$$\left.\frac{\mathrm{d}w_{\mathrm{A}}}{\mathrm{d}z}\right|^{\mathrm{T}} = \left.\frac{\mathrm{d}w_{\mathrm{A}}}{\mathrm{d}z}\right|^{\mathrm{BM}} = \left.\frac{\mathrm{d}w_{\mathrm{A}}}{\mathrm{d}z}\right|^{\mathrm{I}} = \left.\frac{\mathrm{d}w_{\mathrm{A}}}{\mathrm{d}z}\right|^{\mathrm{BV}} \tag{2}$$

The total rate of transport is the sum of the rate of transport in each of the three regions,

$$A_z^{\mathrm{T}} j_{\mathrm{A}}^{\mathrm{T}} = A_z^{\mathrm{BM}} j_{\mathrm{A}}^{\mathrm{BM}} + A_z^{\mathrm{I}} j_{\mathrm{A}}^{\mathrm{I}} + A_z^{\mathrm{BV}} j_{\mathrm{A}}^{\mathrm{BV}} \tag{3}$$

where $A_z^J$ is the cross-sectional area of region $J$. Combining Eqs. (1)–(3) leads to an expression for the total diffusivity parallel to the interface,

$$D_{\parallel}^{\mathrm{T}} = \frac{A_z^{\mathrm{BM}} \rho^{\mathrm{BM}} D_{\parallel}^{\mathrm{BM}} + A_z^{\mathrm{I}} \rho^{\mathrm{I}} D_{\parallel}^{\mathrm{I}} + A_z^{\mathrm{BV}} \rho^{\mathrm{BV}} D_{\parallel}^{\mathrm{BV}}}{A_z^{\mathrm{T}} \rho^{\mathrm{T}}} \tag{4}$$

For the case of mass transport in series (perpendicular to the interface), at steady state, the flux in Eq. (1) is the same for each region and for the system total. Also, the cross-sectional area of each region is a constant. Therefore, we have

$$j_{\mathrm{A}}^{\mathrm{T}} = j_{\mathrm{A}}^{\mathrm{BM}} = j_{\mathrm{A}}^{\mathrm{I}} = j_{\mathrm{A}}^{\mathrm{BV}} \tag{5}$$

Furthermore, the total driving force is the sum of the driving forces across each region,

$$\left.\frac{\mathrm{d}w_{\mathrm{A}}}{\mathrm{d}z}\right|^{\mathrm{T}} = \left.\frac{\mathrm{d}w_{\mathrm{A}}}{\mathrm{d}z}\right|^{\mathrm{BM}} + \left.\frac{\mathrm{d}w_{\mathrm{A}}}{\mathrm{d}z}\right|^{\mathrm{I}} + \left.\frac{\mathrm{d}w_{\mathrm{A}}}{\mathrm{d}z}\right|^{\mathrm{BV}} \tag{6}$$

Combining Eqs. (1), (5), and (6) leads to an expression for the total diffusivity perpendicular to the interface,

$$\frac{1}{\rho^{\mathrm{T}} D_{\perp}^{\mathrm{T}}} = \frac{1}{\rho^{\mathrm{BM}} D_{\perp}^{\mathrm{BM}}} + \frac{1}{\rho^{\mathrm{I}} D_{\perp}^{\mathrm{I}}} + \frac{1}{\rho^{\mathrm{BV}} D_{\perp}^{\mathrm{BV}}} \tag{7}$$

The goal of this work is to determine the components of the interfacial diffusivity, $D_{\parallel}^{\mathrm{I}}$ and $D_{\perp}^{\mathrm{I}}$. To do this, we must know all four of the densities, the four cross-sectional areas, and the other six diffusivities that appear in Eqs. (4) and (7). Because the BM and BV phases are isotropic, we know that $D^{\mathrm{BM}} = D_{\perp}^{\mathrm{BM}} = D_{||}^{\mathrm{BM}}$ and $D^{\mathrm{BV}} = D_{\perp}^{\mathrm{BV}} = D_{\parallel}^{\mathrm{BV}}$. This leaves four densities, four areas, and four diffusivities to be determined for each state point.

We determine these properties in the following manner. In our earlier MD simulations of the BM phase we have reported the $\rho^{\mathrm{BM}}$ and $D^{\mathrm{BM}}$ of water at four degrees of hydration corresponding to nominal water weight percents of 5%, 10%, 15% and 20% [14]. In this work, we performed extensive MD simulations of the BM/I/BV system, from which we collected $\rho^{\mathrm{T}}$, $\rho^{\mathrm{I}}$, $\rho^{\mathrm{BV}}$, $D_{\perp}^{\mathrm{T}}$ and $D_{\parallel}^{\mathrm{T}}$.

There remains some ambiguity in the determination of the density of a region and the appropriate cross-sectional area. First we consider strictly a BM simulation, as reported previously [14]. In this case, there is an aqueous nanonetwork through which diffusion of water occurs. There is no water transport in the hydrophobic region. The question becomes whether one should report the bulk density, that is, the mass of water per simulation volume, $N_{\mathrm{H_2O}} m_{\mathrm{H_2O}} / V_{\mathrm{sim}}$, or the density of water in the nanochannels, $N_{\mathrm{H_2O}} m_{\mathrm{H_2O}} / V_{\mathrm{chan}}$, because they exclusively transport the water. Likewise, what is the appropriate area to use, $A_{\mathrm{sim}} = V_{\mathrm{sim}} / L$ or

$A_{\text{chan}} = V_{\text{chan}}/L$, where $L$ is the length of the simulation box in the direction of transport? All other things being equal, one would much rather use the simulation volume and area because they can be determined unambiguously. Also, one should acknowledge that the estimation of the volume of the aqueous nanonetwork is not trivial.

To resolve this issue, we can consider the BM region itself to be an isotropic phase composed of two subregions, one composed of polymer (P) with water density, $\rho_{\text{P}}^{\text{BM}} = 0$, volume, $V_{\text{P}}$, and water diffusivity, $D_{\text{P}}^{\text{BM}} = 0$. The second subregion is the network of aqueous channels (chan) with $\rho_{\text{chan}}^{\text{BM}} = N_{\text{H}_2\text{O}} m_{\text{H}_2\text{O}}/V_{\text{chan}}$; volume, $V_{\text{chan}}$, and water diffusivity, $D_{\text{chan}}^{\text{BM}}$. Because the two subregions are parallel (as opposed to being in series), we use the same logic employed previously to arrive at Eq. (4) for the total diffusivity in the BM region,

$$D^{\text{BM}} = \frac{A_{z,\text{P}}^{\text{BM}} \rho_{\text{P}}^{\text{BM}} D_{\text{P}}^{\text{BM}} + A_{z,\text{chan}}^{\text{BM}} \rho_{\text{chan}}^{\text{BM}} D_{\text{chan}}^{\text{BM}}}{A_{z,\text{T}}^{\text{BM}} \rho_{\text{T}}^{\text{BM}}} = \frac{A_{z,\text{chan}}^{\text{BM}} \rho_{\text{chan}}^{\text{BM}} D_{\text{chan}}^{\text{BM}}}{A_{z,\text{T}}^{\text{BM}} \rho_{\text{T}}^{\text{BM}}} = D_{\text{chan}}^{\text{BM}} \tag{8}$$

Therefore, we see that the total diffusivity of the BM region is exactly the diffusivity of the aqueous subregion. There is no need to be concerned with defining channel volumes because those factors cancel each other.

For the multiphase system with the BM, I, and BV regions, the solution is not so simple because the density is zero in each of the phases. Our simulation box is a right parallelepiped with geometry defined by side magnitudes $L_x$, $L_y$, and $L_z$ and angles $\theta_{xy} = \theta_{xz} = \theta_{yz} = 90^\circ$. The interface lies in the *xy* plane. Along the *z* axis, we define distances corresponding to each region, such that the sum of these regions is $L_z$, $L_z = L_z^{\text{BM}} + L_z^{\text{I}} + L_z^{\text{BV}}$. Therefore, the volume of region *J* is $V^J = L_z^J L_x L_y$. The density of region *J* is then determined knowing the number of water molecules in region *J*, $N_{\text{H}_2\text{O}}^J$, and the region volume. If we insert these definitions into Eq. (4) for diffusion parallel to the interface, we obtain

$$D_{\parallel}^{\text{T}} = \frac{N_{\text{H}_2\text{O}}^{\text{BM}} D_{\parallel}^{\text{BM}} + N_{\text{H}_2\text{O}}^{\text{I}} D_{\parallel}^{\text{I}} + N_{\text{H}_2\text{O}}^{\text{BV}} D_{\parallel}^{\text{BV}}}{N_{\text{H}_2\text{O}}^{\text{T}}} = \chi_{\text{H}_2\text{O}}^{\text{BM}} D_{\parallel}^{\text{BM}} + \chi_{\text{H}_2\text{O}}^{\text{I}} D_{\parallel}^{\text{I}} + \chi_{\text{H}_2\text{O}}^{\text{BV}} D_{\parallel}^{\text{BV}} \tag{9}$$

where $\chi_{\text{H}_2\text{O}}^J \equiv N_{\text{H}_2\text{O}}^J / N_{\text{H}_2\text{O}}^T$ is the fraction of water molecules residing in region *J*. Again, we see that there is no need to know the volume of the individual regions, only the distribution of water

among them. The distribution of the water among the regions is an unambiguous output from the MD multiphase simulation.

Similarly, if we put these definitions into Eq. (7) for diffusion perpendicular to the interface, then we have

$$\frac{1}{D_{\perp}^{\mathrm{T}}} = \frac{1}{\frac{\chi_{\mathrm{H_2O}}^{\mathrm{BM}}}{\psi_z^{\mathrm{BM}}} D_{\perp}^{\mathrm{BM}}} + \frac{1}{\frac{\chi_{\mathrm{H_2O}}^{\mathrm{I}}}{\psi_z^{\mathrm{I}}} D_{\perp}^{\mathrm{I}}} + \frac{1}{\frac{\chi_{\mathrm{H_2O}}^{\mathrm{BV}}}{\psi_z^{\mathrm{BV}}} D_{\perp}^{\mathrm{BV}}} \tag{10}$$

where $\psi_z^J \equiv L_z^J / L_z$ is the distribution of volume between the three phases. The specification of $L_z^J$ is arbitrary but must be chosen consistently in the definitions of $\chi_{\mathrm{H_2O}}^J$ and $\psi_z^J$.

In the case of hydronium, following the same procedure and arguments, Eqs. (9) and (10) can be rewritten as

$$D_{\parallel}^{\mathrm{T}} = \chi_{\mathrm{H_3O}}^{\mathrm{BM}} D_{\parallel}^{\mathrm{BM}} + \chi_{\mathrm{H_3O}}^{\mathrm{I}} D_{\parallel}^{\mathrm{I}} \tag{11}$$

$$\frac{1}{D_{\perp}^{\mathrm{T}}} = \frac{1}{\frac{\chi_{\mathrm{H_3O}}^{\mathrm{BM}}}{\psi_z^{\mathrm{BM}}} D_{\perp}^{\mathrm{BM}}} + \frac{1}{\frac{\chi_{\mathrm{H_3O}}^{\mathrm{I}}}{\psi_z^{\mathrm{I}}} D_{\perp}^{\mathrm{I}}} \tag{12}$$

because there are no hydronium ions in the vapor phase; that is, $N_{\mathrm{H_3O}}^{\mathrm{BV}} = \chi_{\mathrm{H_3O}}^{\mathrm{BV}} = 0$. Using Eqs. (11) and (12), we calculated the parallel and the perpendicular components of the self-diffusivity of hydronium in the interfacial region.

Equations (9)–(12) are macroscopic equations derived from continuum theory and require Fickian diffusivities for binary systems. Our MD simulations are molecular-level descriptions that deliver self-diffusivities for a ternary (Nafion, hydronium ions, and water) system. At this time, we accept these limitations.

### 2.3 SIMULATION METHODS

In the simulations, we have used the same interaction potentials for the polymer electrolyte, water and hydronium molecules as used earlier in the simulations of the bulk hydrated membrane [14]. In summary, each polymer unit consists of three monomers. Each ionomer has three side chains, 46 $CF_2$ groups along the backbone and $CF_3$ group at each end. The justification of this model and the successful comparison with similar simulations performed

with longer chains has been discussed previously [14]. The water is modeled using the TIP3P model with a flexible OH bond, while the model for hydronium ions is similar to that used by Urata *et al.* [27].

As was the case in the bulk hydrated membrane simulations, we have examined the properties of the system for water contents of 5%, 10%, 15%, and 20% by weight of the hydrated Nafion polymer electrolyte. These correspond to the $\lambda$ ratio (defined as the number of water molecules to the number of $SO_3^-$ groups) of 3.44, 5.42, 8.63, and 11.83, respectively.

The equilibrated configurations from the previous simulations [14] were used as a portion of the initial configuration in the present simulation. Specifically, we chose to increase the simulation volume by a factor of 2 in all directions. Therefore, we quadrupled the number of Nafion, water, and hydronium ions in these interfacial simulations, which leads to doubling in system size in the *x* and *y* dimensions. In the *z* dimension, we initially left the extra volume empty and allowed it to be filled with vaporized water molecules through equilibration during the simulation. This results in a simulation with 256 Nafion ionomers containing 768 $SO_3^-$ groups as well as 768 $H_3O^+$ ions and 2640 to 9088 water molecules, depending upon the humidity level. Each configuration was equilibrated for 2 ns, and the data production runs were carried on for an additional 2 ns. The total system densities (including vapor volume), simulation length of the box, and the number of molecules of each type used are listed in the Table 2.1.

Simulations were carried out at constant NVT for the system. The 2-time-scale r-RESPA integration scheme [44] was used to solve the equations of motion with 2.0 fs for the large time step and 0.4 fs for the intramolecular motions. The Nosé–Hoover thermostat was used to maintain a constant temperature of 300 K [45,46].

We note that these simulations do not contain a structural diffusion mechanism. However, from the analysis of the hydration structure of the hydronium ions obtained from these simulations we can study the characteristics of Zundel and Eigen ions, which are necessary for structural diffusion [47,48].

## 2.4 RESULTS AND DISCUSSION

In this work, we have divided the simulation box into four regions, as shown in the Figure 2.4. Because the system is periodic in all dimensions (with a period of nominally 12 nm), we have two interfaces in the system. As noted above, the specification of the width of each of these faces, $L_z^J$, is arbitrary. We have chosen to make the widths of the membrane-side of the interface (MI) and vapor-side of the interface (VI) each 10 Å. This makes the width of the bulk membrane (BM) and bulk vapor (BV) nominally 40 Å. The interfacial width is intentionally an overestimate and is chosen to make sure that all of the interfacial behavior is captured in the interfacial regions. Admittedly, some bulk behavior will also be included in the interfacial region. A quantitative interfacial width is calculated by fitting hyperbolic tangents in the density profiles, as discussed later.

We begin the discussion by studying the snapshots of the interfacial region and analyzing the orientation of the hydronium ions at the interface. The various structural measures, including pair correlation functions, hydronium ion hydration histograms, and density distributions are studied in the above-mentioned four regions. Finally, the diffusivities of the water molecules and hydronium ions at the interface are reported.

### 2.4.1 Pair Correlation Functions

As in the previous work [14], the pair correlation functions (PCFs) were generated for virtually every combination of pairs of atoms in the simulation. In this work, we limit ourselves to reporting the PCF between the O of $H_3O^+$ and the O of $H_2O$. What is new in this work is that we report separate PCFs for the four regions of the simulation cell, BM, MI, VI and BV. The PCF is an unnormalized conditional probability distribution. In homogeneous systems, it is scaled by the bulk density so that the PCF is unity at infinite separation.

In this work, we have an inhomogeneous system with four regions and we report PCFs for each region. In inhomogeneous systems, the bulk density now is a weighted average of the individual phase densities and if used as a scaling factor will not generate PCFs from the different phases that are unity at infinite separation. Therefore, we have scaled each PCF independently so that they individually approach unity at our maximum distance of 10 Å.

In Figure 2.5(a)–(d), we show the $O_{H_3O^+} - O_{H_2O}$ PCF as a function of the region in the simulation cell and degree of humidity. From these figures, we observe that the first peaks are the same at 2.55 Å in the three regions where hydronium ions are present at 5, 10, 15, and 20 wt% water. The fourth region, the bulk vapor, does not contain any hydronium ions and hence is not shown in the plot. Practically, the third region, which is the vapor side interface, should also not contain any hydronium ions, but because of the roughness of the interface, there is some distribution of molecules around a geometric center of the interface that separates the MI and VI regions. At all water contents, we observe the sharpest first peak in the VI, a first peak of intermediate sharpness in the MI, and the least sharp first peak in the BM region. The second peak is also more pronounced for the interfacial phases. This trend can be tied to the water density, which is decreasing as one moves away from the bulk membrane, as discussed shortly. The preferential distribution of water molecules near to the hydronium ion is accentuated by lowering the average water density. From an energetic point of view, the relative energetic advantage of being at a nearest neighbor position is greater as the bulk density decreases. We see a similar effect in the fact that the height of the first peak decreases as the water content is increased.

### 2.4.2 Hydronium Hydration Histograms

The PCFs shown in Figure 2.5 can be integrated to give the number of water molecules within a specific radial distance. We have chosen to examine the degree of hydration of hydronium ions based on the number of water molecules in which the O of $H_2O$ lies within 3.2 Å of the O of $H_3O^+$. This distance was chosen as a nominal value of the minimum between the first and second peak of the PCFs in Figure 2.5. Integrating the same PCF from quantum mechanical simulations of bulk water [48], we find that the average number of water molecules within 3.2 Å of an $H_3O^+$ is 3.78 [49]. This corresponds generally to an O of $H_2O$ hydrogen-bonding with each of the three H atoms of the $H_3O^+$, and the O of the $H_3O^+$ hydrogen-bonding to an H atom of a fourth $H_2O$.

The probability of finding a fixed number of water molecules around a hydronium ion with a radial distance less than 3.2 Å is shown in Figure 2.6 as a function of the region within the simulation cell and degree of humidity. From a comparison of Figures 2.6(a)–(d), we can clearly

see that as the water content is increased the hydration distribution is also shifted to higher values in all regions. The probability of finding a hydronium ion with 3 or more water molecules within 3.2 Å increases with increasing water content. This histogram has relevance to structural diffusion, which requires the existence of Eigen ions, involving the presence of at least three water molecules within 3.2 Å. From the figures, we see that there is a slight decrease in the probability of finding a fully hydrated hydronium ion as one approaches the interface, which is present at all levels of humidity. This decrease in probability would correspond to a lower value of the structural diffusivity near the interface.

### 2.4.3 Hydronium Orientation at the Interface

In Figure 2.7, we present the probability distribution of the orientation of the hydronium ions with respect to the *z* axis (perpendicular to the interface surface). The hydronium axis is defined to originate at the midpoint of the three hydrogen atoms and terminate at the oxygen position. An angle of 0° corresponds to the oxygen atom protruding into the vapor phase. An angle of 180° corresponds to the oxygen atoms buried in the membrane. From the distributions shown in Figure 2.7, it is clear that the distribution is isotropic in the bulk membrane. However, at the interface, there is a strong preference for the hydronium to be oriented with the oxygen atom protruding into the vapor phase. A snapshot taken normal to the interfacial surface, depicting this configuration, is shown in Figure 2.8. In this figure, the green spheres represent the oxygen of hydronium. Where one can see green spheres unobscured by the white hydrogen attached to them, those oxygens are sticking out into the vapor phase. There is previous experimental [50,51] and simulation data [52] showing this preferential orientation. The reason for its existence lies in the fact that it is energetically favorable for the hydronium ion to maintain three hydrogen bonds between its hydrogen atoms and the oxygen atom of $H_2O$ in the hydrated membrane.

### 2.4.4 Interfacial Width

In Figure 2.9, we show the average density profile of water for the four levels of humidity with the zero coordinate on the *x* axis corresponding to the central location of the membrane/vapor interface. There is some noise in the water density in the membrane because the

system is spatially inhomogeneous on the nanoscale, and because simulations are not long enough to average out this effect completely. It is typical when performing the simulations of two phase systems to fit the density distribution to a hyperbolic tangent, which has four parameters [53]. Three of the parameters, the location of the interface, the BM density, and the BV density, are taken directly from simulation. The fourth parameter, the interfacial width, is fit to the simulation data. The interfacial width calculated is shown in the Table 2.2. We see that as the humidity increases, the interfacial width decreases. One can understand the decrease in interfacial width with increasing humidity by examining the snapshots of the system taken parallel to the interfacial surface, as shown in Figures 2.10(a) at 5 wt % and 2.10(b) at 20 wt %. The surface has a roughness due to the relatively large and inflexible Nafion molecules. This roughness can be smoothed by small water molecules filling in the valleys of the interfacial roughness created by Nafion, resulting in a thinner interface. So the dehydrated region of the membrane near the interface decreases with the increase in water content leading to decrease in interfacial width.

### 2.4.5 Interfacial Diffusivities

As derived in Sec. 2.2, Eqs. (9)–(12) provide a means to obtain the parallel and perpendicular components of the self-diffusivity of water and the vehicular portion of the self-diffusivity of the hydronium ion. In Tables 2.3 and 2.4, we report the vehicular component of the interfacial diffusivities of the hydronium ion parallel and perpendicular to the surface respectively. The values of the bulk membrane diffusivities are taken from earlier work [14]. The values of the total two-phase parallel and perpendicular diffusivities were generated in the current work, as were the molecular distributions of molecules among the phases. Eqs. (11) and (12) were used to generate the interfacial diffusivities. From the tables, we observe that the vehicular component of the hydronium ion parallel to the interface is statistically the same as it is in the bulk membrane.

We do, however, observe that the component perpendicular to the interface is substantially larger than the parallel component. Because the hydronium ions do not enter the vapor phase, there can be no net diffusion of hydronium ions perpendicular to the interface on a macroscopic time scale. The same is not true of the parallel component, in which the membrane

is still infinite although periodic. Thus if we could simulate an infinitely long time, we would find a zero diffusivity in the perpendicular direction. Here, we are reporting relatively short time diffusivities. (The simulations are nonetheless sufficiently long to establish the linear behavior required in the infinite-time limit of the Einstein relation.) To gauge the length scale associated with this diffusive motion, one can consider that the width of the membrane in these simulations is nominally 60 Å. An estimate of the length scale traveled by hydronium ions on average can be obtained by taking the square root of the final mean square displacements used in the determination of the diffusivity. These final MSDs correspond to a length between 9 and 20 Å. This is thus a measure of dynamics on the nanosecond time scale, as opposed to a macroscopic time scale. On a nanoscopic time scale, we observe enhanced diffusivity perpendicular to the interface. This may be a result of the density gradient that exists in the direction perpendicular to the interface, as shown in Figure 9. In short, we see no observable additional resistance to mass transport of the vehicular component of the hydronium ion due to the interface.

We have used Eqs. (9) and (10) to evaluate the diffusivity of water parallel and perpendicular to the interface. Water differs from the hydronium ion in that it is present in the vapor phase. In this work, the diffusivity of water in the bulk vapor phase, $D^{BV}$, is assumed to be 0.1 $cm^2/s$, a reasonable estimate of the diffusivity of a gas at room temperature and pressure.

From Table 2.5 we can see that perpendicular component of the interfacial diffusivity of the water displays the same behavior as that observed for the hydronium ions, namely, that it increases with humidity and is greater than the diffusivity in the bulk membrane. Thus, we do not see an inherent additional mass transfer resistance to water through the membrane/vapor interface.

The simulations were unable to generate a statistically reliable diffusivity for water parallel to the interface. There are statistically very few water molecules in the vapor phase. In defining the simulation volume, there are two choices. If there is a large vapor-phase that allows many water molecules in the vapor phase, then we obtain good statistics on the vapor properties (which are not interesting), but this will alter the bulk water content of the hydrated membrane. Alternatively, our choice was to simulate a small vapor phase, while maintaining the same nominal water density in the hydrated membrane. This manifested in an inability to extract a statistically (or physically) meaningful value of the diffusion coefficient of water parallel to the

interface. Hence we do not report values for the diffusion coefficient of water parallel to the interface. However, based on the past relationship between the water and hydronium diffusivities in the bulk membrane region, it is not unreasonable to infer that the parallel component of the diffusivity of water is similar to that in the bulk phase, as was the case with the hydronium ion.

## 2.5 CONCLUSIONS

We have performed molecular dynamics simulations and examined the structural and transport properties of water and hydronium ions at the interface of a Nafion polymer electrolyte membrane and a vapor phase. We studied systems at 5%, 10%, 15%, and 20% water content by weight at 300K. The diffusivities of the hydronium ions and water molecules increase with water content. We have reported interfacial water and hydronium ion vehicular diffusion components parallel and perpendicular to the interface. For hydronium ions, the perpendicular components are much higher than the parallel component. The parallel component is almost equal to that of the bulk hydrated membrane. At the nanosecond scale, the perpendicular component of the vehicular diffusivity is large, likely due to the density gradient at the interface. At the macro time scale, the absence of hydronium ions in the vapor phase implies that there is no net diffusion of the ions perpendicular to the interface. For water, we found qualitatively similar diffusive behavior except that water can certainly exist in vapor phase. From these diffusivities we can conclude that there is no inherent resistance to the vehicular diffusion of the hydronium ions and water due to the interface. However, we found that there was a decrease in the fraction of fully hydrated hydronium ions at the interface. This translates into a lower probability of forming Eigen ions, which are necessary for structural diffusion. This finding is consistent with a water depletion region at the membrane/vapor interface that is less than a nanometer wide. The structural measures like pair correlation function showed that the association of water molecules with the hydronium ion increases as the average water density decreases. This can be observed by the monotonic decrease in the peak height as the water content increases and also as one move from the vapor interfacial region to the bulk membrane. From the average density profile of water we concluded that the thickness of the interface decreases with increasing humidity. Finally, we observed that the hydronium ions displayed a preferential orientation at the interface, with their oxygen atoms exposed to the vapor phase.

## 2.6 ACKNOWLEDGEMENT

The work is supported by a grant from the U. S. Department of Energy BES under the contract number DE-FG02-05ER15723. This research used resources of the Center for Computational Sciences at Oak Ridge National Laboratory, which is supported by the Office of Science of the DOE under Contract DE-AC05-00OR22725.

# References

[1] Kreuer, K. D.; Paddison, S. J.; Spohr, E. and Schuster, M., *Chem. Rev.* **104**, 4637 (2004).

[2] O'Hayre, R. and Prinz, F. B., *J. Electrochem. Soc.* **151**, A756 (2004).

[3] Xie, J.; More, K. L.; Zawodzinski, T. A. and Smith, W. H., *J. Electrochem. Soc.* **151**, A1841 (2004).

[4] Hsu, W. Y. and Gierke, T. D., *J. Membr. Sci.* **13**, 307 (1983).

[5] Verbrugge, M. W. and Hill, R. F., *J. Electrochem. Soc.* **137**, 886 (1990).

[6] Falk, M., *Can. J. Chem.* **58**, 1495 (1980).

[7] Vishnyakov, A. and Neimark, A. V., *J. Phys. Chem. B* **105**, 9586 (2001).

[8] Rivin, D.; Meermeier, G.; Schneider, N. S.; Vishnyakov, A. and Neimark, A. V., *J. Phys. Chem. B* **108**, 8900 (2004).

[9] Petersen, M. K.; Wang, F.; Blake, N. P.; Metiu, H. and Voth, G. A., *J. Phys. Chem. B* **109**, 3727 (2005).

[10] Petersen, M. K. and Voth, G. A., *J. Phys. Chem. B* **110**, 18594 (2006).

[11] Spohr, E.; Commer, P. and Kornyshev, A. A., *J. Phys. Chem. B* **106**, 10560 (2002).

[12] Commer, P.; Cherstvy, A. G.; Spohr, E. and Kornyshev, A. A., *Fuel Cells* **2**, 127 (2002).

[13] Jang, S. S.; Molinero, V.; Cagin, T. and Goddard, W. A., *J. Phys. Chem. B* **108**, 3149 (2004).

[14] Cui, S. T.; Liu, J.; Esai Selvan, M.; Keffer, D. J.; Edwards, B. J. and Steele, W. V., *J. Phys. Chem. B* **111**, 2208 (2007).

[15] Paddison, S. J. and Zawodzinski, T. A., *Solid State Ionics* **113**, 333 (1998).

[16] Paddison, S. J.; Pratt, L. R. and Zawodzinski, T. A., *J. New Mater. Electrochem. Sys.* **2**, 183 (1999).

[17] Paddison, S. J.; Paul, R. and Zawodzinski, T. A., *J. Electrochem. Soc.* **147**, 617 (2000).

[18] Paddison, S. J.; Paul, R. and Zawodzinski, T. A., *J. Chem. Phys.* **115**, 7753 (2001).

[19] Paul, R. and Paddison, S. J., *J. Chem. Phys.* **115**, 7762 (2001).

[20] Eikerling, M.; Paddison, S. J. and Zawodzinski, T. A., *J. New Mater. Electrochem. Sys.* **5**, 15 (2002).

[21] Paddison, S. J.; Paul, R. and Kreuer, K. D., *Phys. Chem. Chem. Phys.* **4**, 1151 (2002).

[22] Paddison, S. J. and Paul, R., *Phys. Chem. Chem. Phys.* **4**, 1158 (2002).

[23] Paddison, S. J., *Annu. Rev. Mater. Res.* **33**, 289 (2003).

[24] Paddison, S. J. and Elliott, J. A., *J. Phys. Chem. A* **109**, 7583 (2005).

[25] Paul, R. and Paddison, S. J., *J. Chem. Phys.* **123**, 224704 (2005).

[26] Paddison, S. J. and Elliott, J. A., *Phys. Chem. Chem. Phys.* **8**, 2193 (2006).

[27] Urata, S.; Irisawa, J.; Takada, A.; Shinoda, W.; Tsuzuki, S. and Mikami, M., *J. Phys. Chem. B* **109**, 4269 (2005).

[28] Venkatnathan, A.; Devanathan, R. and Dupuis, M., *J. Phys. Chem. B* **111**, 7234 (2007).

[29] Choi, P.; Jalani, N. H. and Datta, R., *J. Electrochem. Soc.* **152**, A1548 (2005).

[30] Janssen, G. J. M., *J. Electrochem. Soc.* **148**, A1313 (2001).

[31] Zawodzinski, T. A.; Derouin, C.; Radzinski, S.; Sherman, R. J.; Smith, V. T.; Springer, T. E. and Gottesfeld, S., *J. Electrochem. Soc.* **140**, 1041 (1993).

[32] Hirunsit, P. and Balbuena, P. B., *J. Phys. Chem. C* **111**, 1709 (2007).

[33] Yan, W. M.; Chu, H. S.; Chen, J. Y.; Soong, C. Y. and Chen, F. L., *J. Power Sources* **162**, 1147 (2006).

[34] Bernardi, D. M. and Verbrugge, M. W., *AIChE J.* **37**, 1151 (1991).

[35] Liu, J.; Esai Selvan, M.; Cui, S. T.; Edwards, B. J.; Keffer, D. J. and Steele, W. V., *J. Phys. Chem. C* submitted for publication (2007).

[36] Allen, M. P. and Tildesley, D. J., *Computer Simulation of Liquids*, Oxford Science Publications, Oxford (1987).

[37] Haile, J. M., *Molecular Dynamics Simulation*, John Wiley & Sons, Inc., New York (1992).

[38] Gubbins, K. E., Thermal Transport Coefficients for Dense Fluids in: *A Specialist Periodical Report. Statistical Mechanics*, Singer, K. (Ed.), Burlington House, London, 1973, p. 194.

[39] Steele, W. A., Time Correlation Functions in: *Transport Phenomena in Fluids*, Hanley, H. J. M. (Ed.), Dekker, New York, 1969, p. 209.

[40] Keffer, D. J. and Adhangale, P., *Chem. Eng. J.* **100**, 51 (2004).

[41] Darken, L. S., *Trans. Am. Inst. Min. Metall. Eng.* **175**, 184 (1948).

[42] Keffer, D. J.; Adhangale, P. and Edwards, B. J., *J. Non-Newtonian Fluid Mech.* **120**, 41 (2004).

[43] Keffer, D. J.; Gao, C. Y. and Edwards, B. J., *J. Phys. Chem. B* **109**, 5279 (2005).

[44] Tuckerman, M.; Berne, B. J. and Martyna, G. J., *J. Chem. Phys.* **97**, 1990 (1992).

[45] Nosé, S., *Mol. Phys.* **52**, 255 (1984).

[46] Hoover, W. G., *Phys. Rev. A* **31**, 1695 (1985).

[47] Agmon, N., *Chem. Phys. Lett.* **244**, 456 (1995).

[48] Tuckerman, M.; Laasonen, K.; Sprik, M. and Parrinello, M., *J. Chem. Phys.* **103**, 150 (1995).

[49] Brancato, G. and Tuckerman, M. E., *J. Chem. Phys.* **122**, 224507 (2005).

[50] Miranda, P. B. and Shen, Y. R., *J. Phys. Chem. B* **103**, 3292 (1999).

[51] Raduge, C.; Pflumio, V. and Shen, Y. R., *Chem. Phys. Lett.* **274**, 140 (1997).

[52] Petersen, M. K.; Iyengar, S. S.; Day, T. J. F. and Voth, G. A., *J. Phys. Chem. B* **108**, 14804 (2004).

[53] Chen, Y.; Aranovich, G. L. and Donohue, M. D., *J. Colloid and Interface Sci.* **307**, 34 (2007).

# Appendix A

## Tables and Figures

**Table 2.1.** Simulation details for the different water contents

| water content (wt %) | number of nafion molecules | number of water molecules | number of hydronium ions | length of the simulation box (Å) | density ($g/cm^3$) |
|---|---|---|---|---|---|
| 5 | 256 | 2640 | 768 | 117.29356 | 0.975 |
| 10 | 256 | 4160 | 768 | 120.13265 | 0.935 |
| 15 | 256 | 6624 | 768 | 123.48771 | 0.9 |
| 20 | 256 | 9088 | 768 | 126.67535 | 0.87 |

**Table 2.2.** Interfacial width at various water contents

| water content (wt %) | interfacial width $\delta$ (Å) |
|---|---|
| 5 | 9.0 |
| 10 | 8.6 |
| 15 | 8.0 |
| 20 | 7.7 |

**Table 2.3.** Diffusion coefficient of hydronium ions in the interfacial region, parallel to the interface[a]

| water content (wt %) | $D_{\perp}^{BM}$ ($10^{-11}$ $m^2$/sec) | $D_{\perp}^{T}$ ($10^{-11}$ $m^2$/sec) | $\chi_{H_3O^+}^{BM}$ (no units) | $\chi_{H_3O^+}^{I}$ (no units) | $D_{\parallel}^{I}$ ($10^{-11}$ $m^2$/sec) |
|---|---|---|---|---|---|
| 5 | 2.97 | 3.63 | 0.635 | 0.365 | 4.79 |
| 10 | 6.36 | 6.19 | 0.683 | 0.317 | 6.33 |
| 15 | 14.73 | 16.04 | 0.699 | 0.301 | 19.07 |
| 20 | 25.23 | 27.04 | 0.717 | 0.282 | 31.64 |

[a] $D_{\parallel}^{BM}$, $D_{\parallel}^{T}$, $D_{\parallel}^{I}$: bulk membrane and total and interfacial diffusivity of the hydronium ions parallel to the interface. $\chi_{H_3O^+}^{BM}$, $\chi_{H_3O^+}^{I}$: fraction of hydronium ions in the bulk membrane and interfacial region.

**Table 2.4.** Diffusion coefficient of hydronium ions in the interfacial region, perpendicular to the interface[a]

| water content (wt %) | $D_{\perp}^{BM}$ ($10^{-11}$ $m^2$/sec) | $D_{\perp}^{T}$ ($10^{-11}$ $m^2$/sec) | $\chi_{H_3O^+}^{BM}$ (no unit) | $\chi_{H_3O^+}^{I}$ (no unit) | $\psi_z^{BM}$ (no unit) | $\psi_z^{I}$ (no unit) | $D_{\perp}^{I}$ ($10^{-11}$ $m^2$/sec) |
|---|---|---|---|---|---|---|---|
| 5 | 2.97 | 3.37 | 0.635 | 0.365 | 0.491 | 0.509 | 39.17 |
| 10 | 6.36 | 5.30 | 0.683 | 0.317 | 0.500 | 0.500 | 21.45 |
| 15 | 14.73 | 13.51 | 0.699 | 0.301 | 0.511 | 0.489 | 66.58 |
| 20 | 25.23 | 21.08 | 0.717 | 0.282 | 0.520 | 0.480 | 90.81 |

[a] $D_{\perp}^{BM}$, $D_{\perp}^{T}$, $D_{\perp}^{I}$: bulk membrane and total and interfacial diffusivity of the hydronium ions perpendicular to the interface. $\chi_{H_3O^+}^{BM}$, $\chi_{H_3O^+}^{I}$: fraction of hydronium ions in the bulk membrane and interfacial region. $\psi_z^{BM}$, $\psi_z^{I}$: length fraction of the bulk membrane and interfacial region.

**Table 2.5.** Diffusion coefficient of water in the interfacial region, perpendicular to the interface[a]

| water (wt %) | $D_{\perp}^{BM}$ ($10^{-10}$ $m^2$/sec) | $D_{\perp}^{T}$ ($10^{-10}$ $m^2$/sec) | $D_{\perp}^{BV}$ ($10^{-5}$ $m^2$/sec) | $\chi_{H_2O}^{BM}$ | $\chi_{H_2O}^{I}$ | $\chi_{H_2O}^{BV}$ | $\psi_z^{BM}$ | $\psi_z^{I}$ | $\psi_z^{BV}$ | $D_{\perp}^{I}$ ($10^{-10}$ $m^2$/sec) |
|---|---|---|---|---|---|---|---|---|---|---|
| 5 | 1.39 | 2.05 | 1.00 | 0.666 | 0.333 | 0.001 | 0.329 | 0.341 | 0.329 | 8.43 |
| 10 | 3.75 | 3.04 | 1.00 | 0.714 | 0.284 | 0.002 | 0.334 | 0.333 | 0.334 | 6.49 |
| 15 | 7.37 | 4.86 | 1.00 | 0.764 | 0.235 | 0.001 | 0.338 | 0.324 | 0.338 | 12.26 |
| 20 | 9.40 | 6.24 | 1.00 | 0.792 | 0.207 | 0.001 | 0.342 | 0.316 | 0.342 | 21.01 |

[a] $D_{\perp}^{BM}$, $D_{\perp}^{T}$, $D_{\perp}^{BV}$, $D_{\perp}^{I}$: bulk membrane, total, bulk vapor and interfacial diffusivity of the water perpendicular to the interface. $\chi_{H_2O}^{BM}$, $\chi_{H_2O}^{I}$, $\chi_{H_2O}^{BV}$: Fraction of water in the bulk membrane, interfacial and bulk vapor region . $\psi_z^{BM}$, $\psi_z^{I}$, $\psi_z^{BV}$: length fraction of the bulk membrane, interfacial and bulk vapor region.

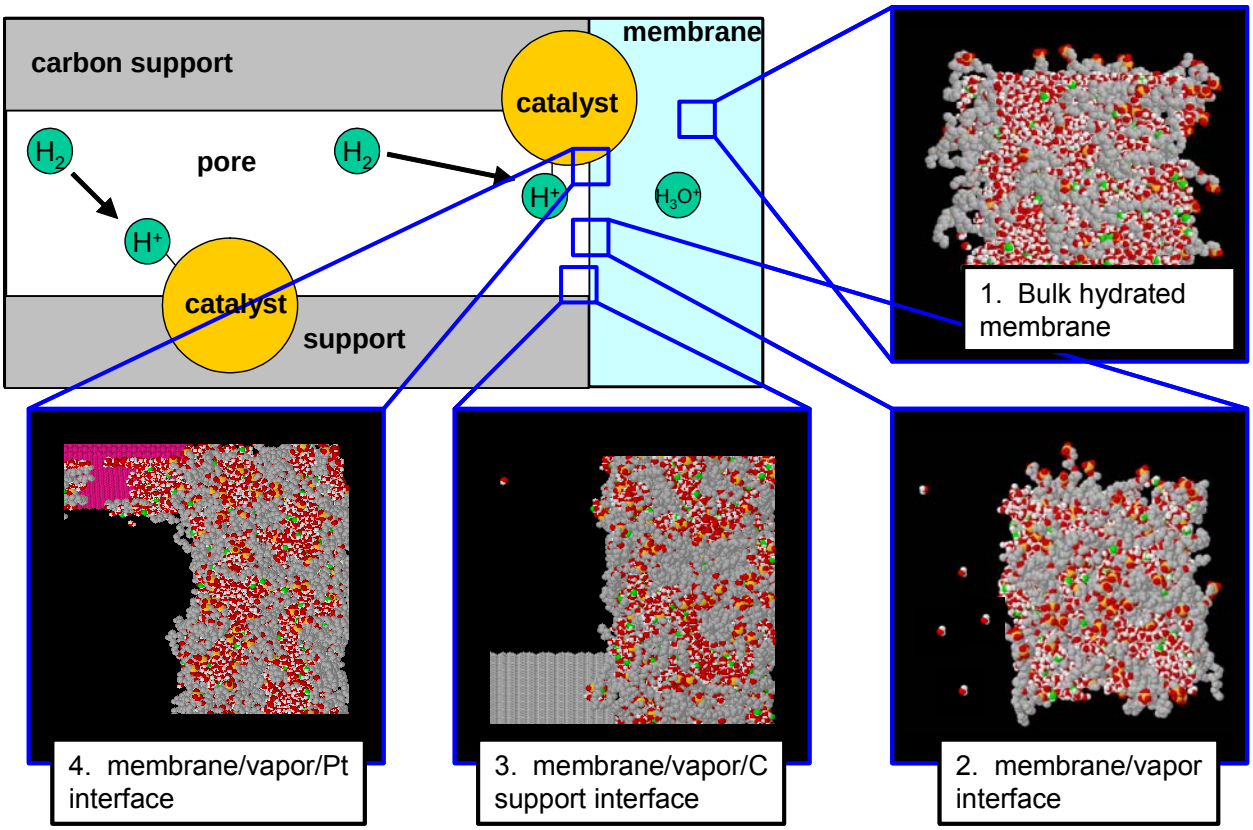


**Figure 2.1.** Idealized schematic illustrating the molecular-level interfaces present at the electrode/electrolyte interface of the membrane electrode assembly.

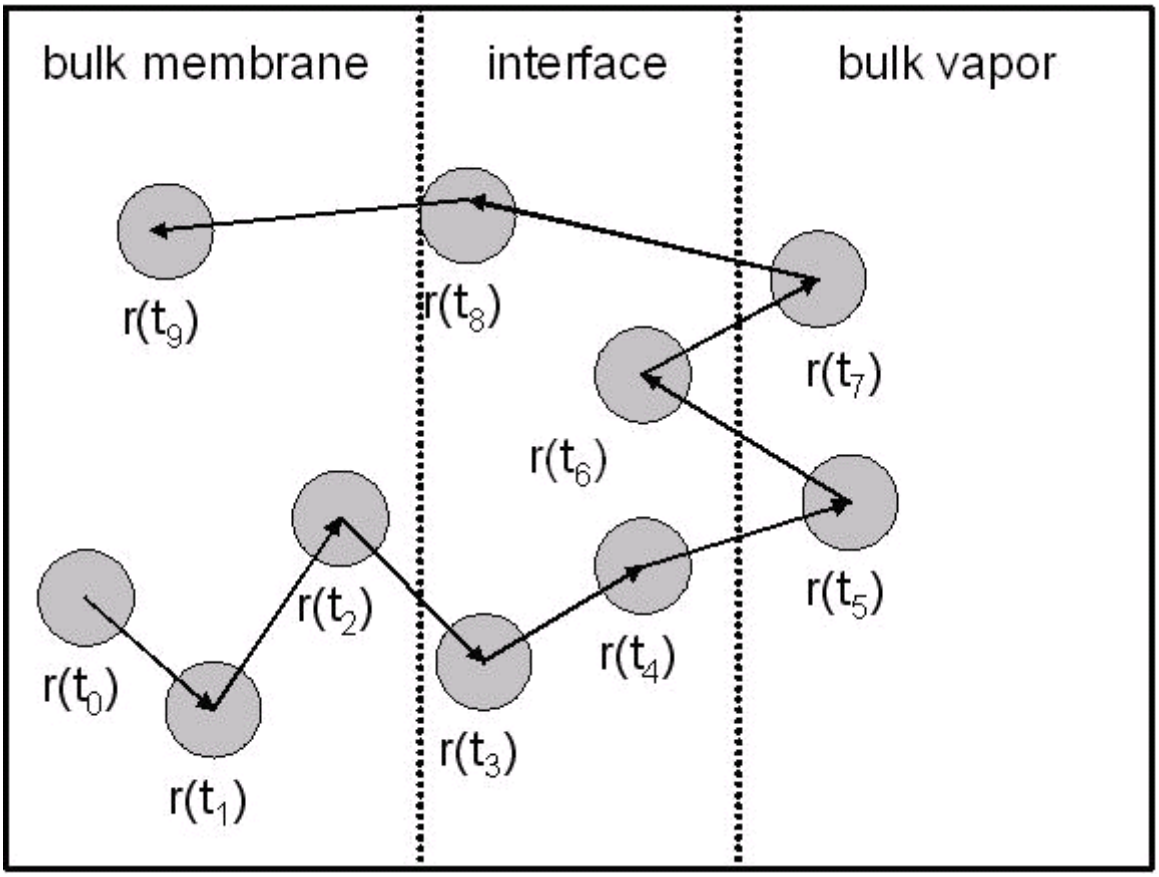


**Figure 2.2.** Schematic illustrating the difficulty of directly calculating an interfacial self-diffusivity from a multiphase simulation using either the VACF or MSD.

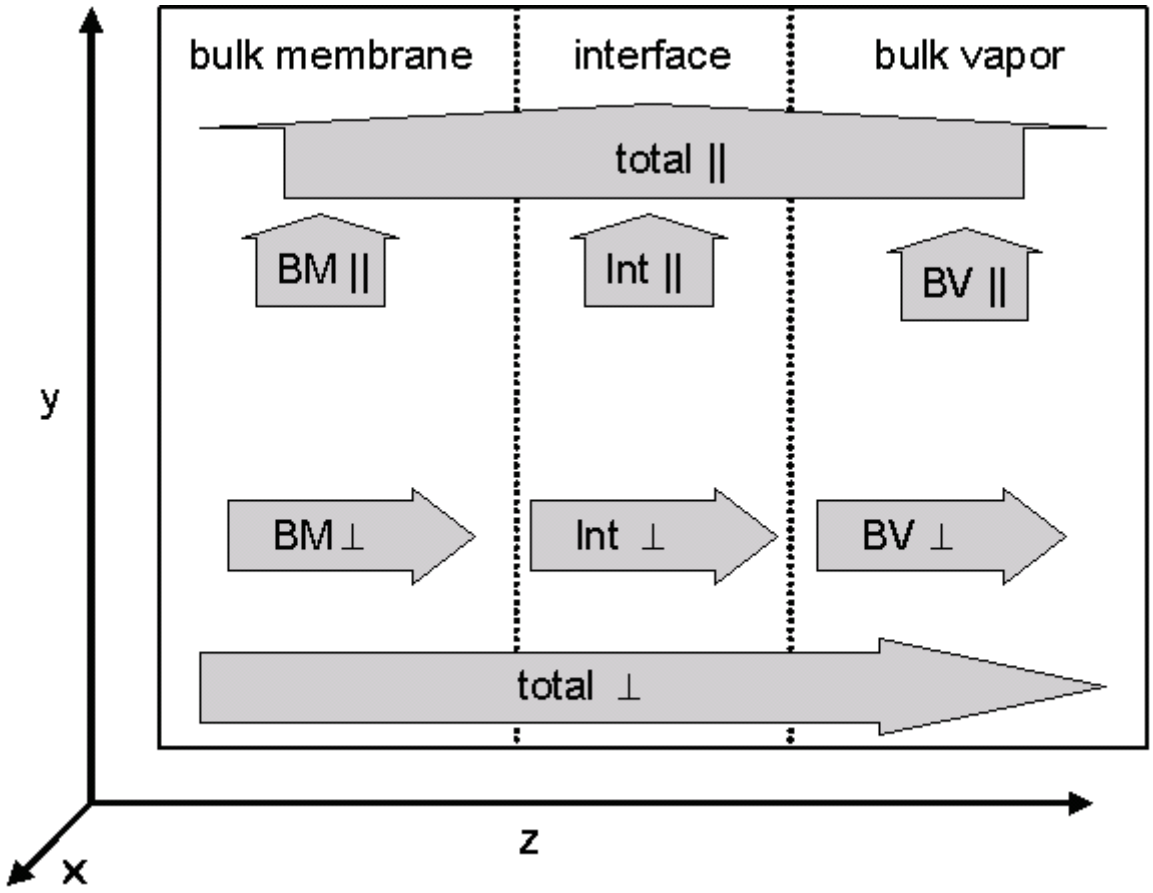


**Figure 2.3.** Schematic illustrating the modes of transport in the three-phase system.

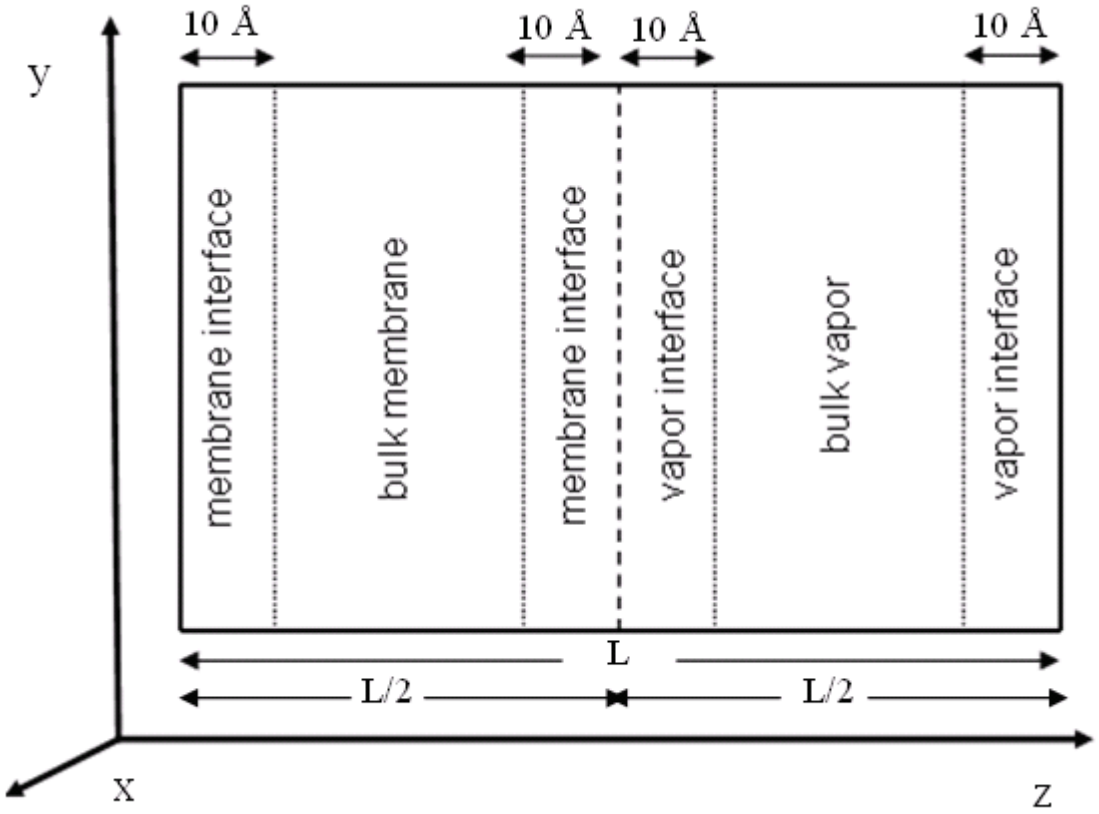


**Figure 2.4.** Schematic illustrating the division of the simulation box into four regions.

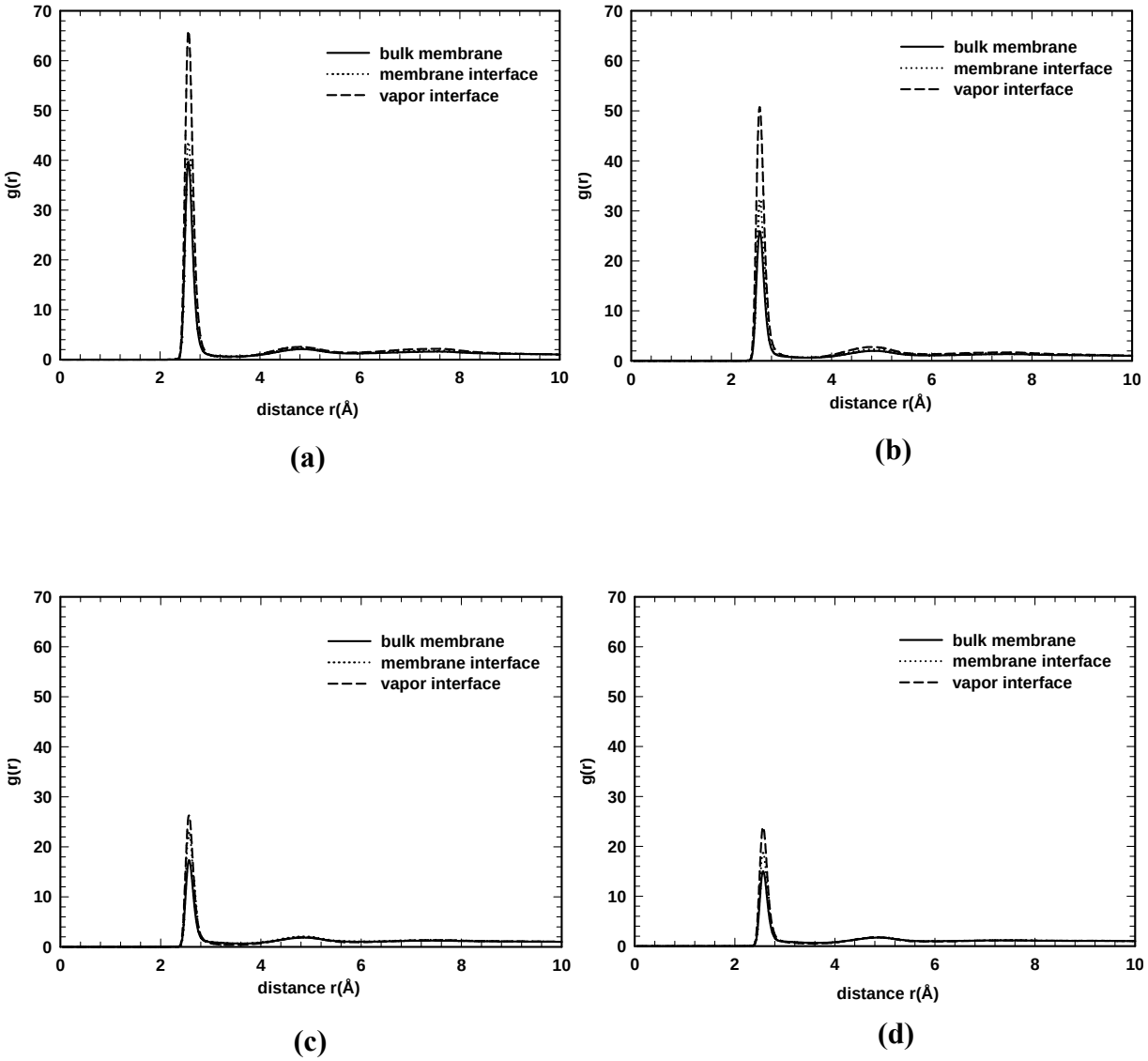


**Figure 2.5.** Pair correlation function between the oxygen of the hydronium ion and the oxygen of water molecules at water contents of **(a)** 5 wt %, **(b)** 10 wt %, **(c)** 15 wt %, and **(d)** 20 wt %. Solid line, bulk membrane; dotted line, membrane interface; and dashed line, vapor interface.

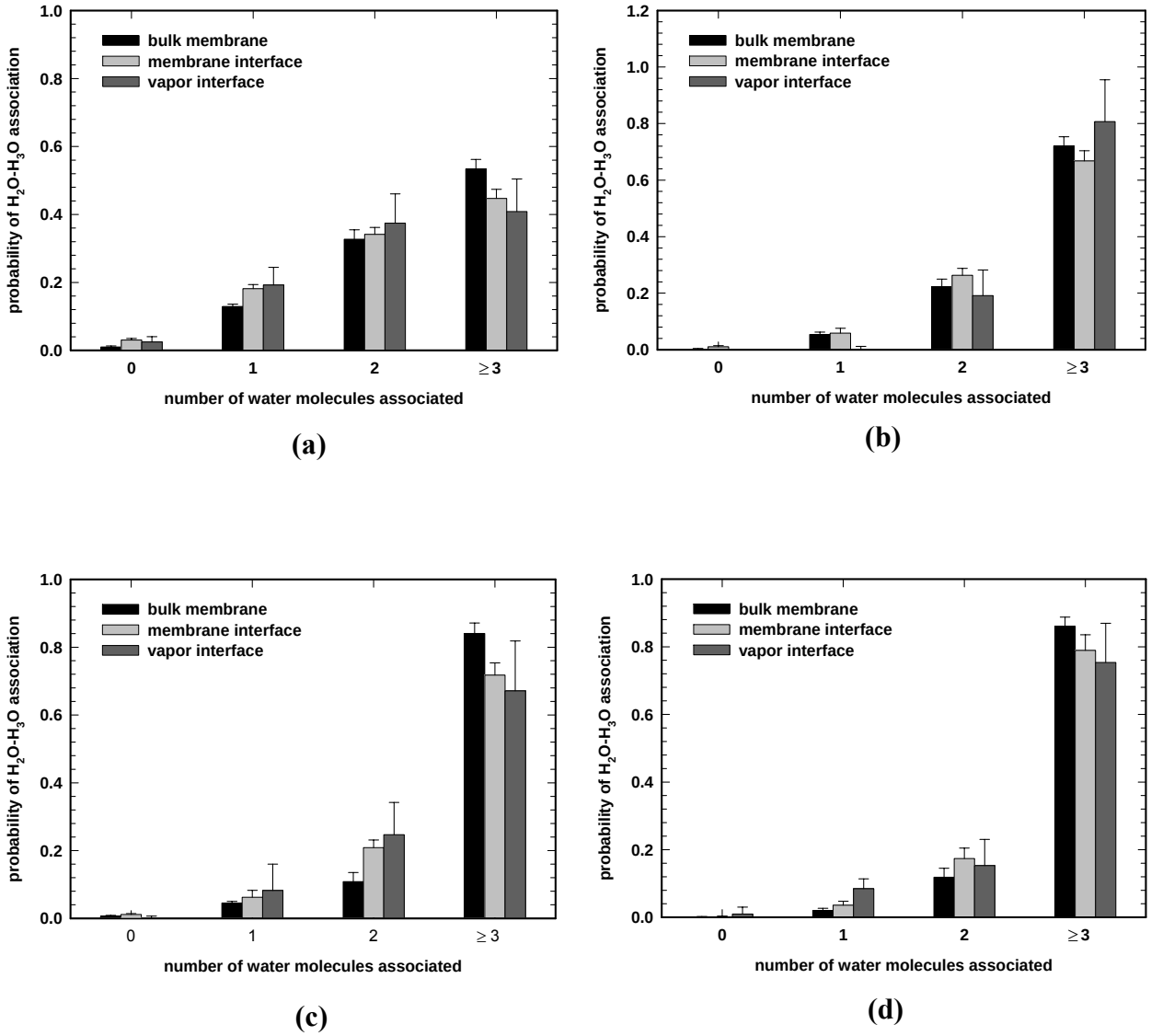


**Figure 2.6.** Distribution of hydrated hydronium complexes as a function of hydration number for water contents of **(a)** 5 wt %, **(b)** 10 wt %, **(c)** 15 wt %, and **(d)** 20 wt %

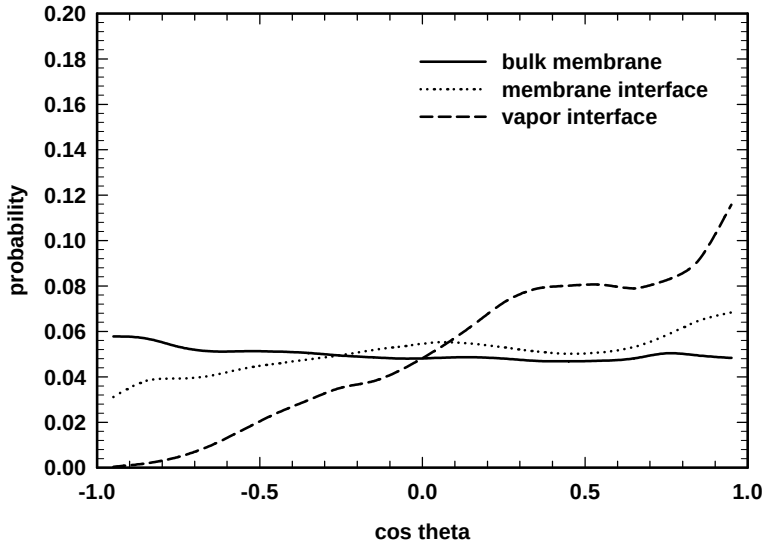


**(a)**

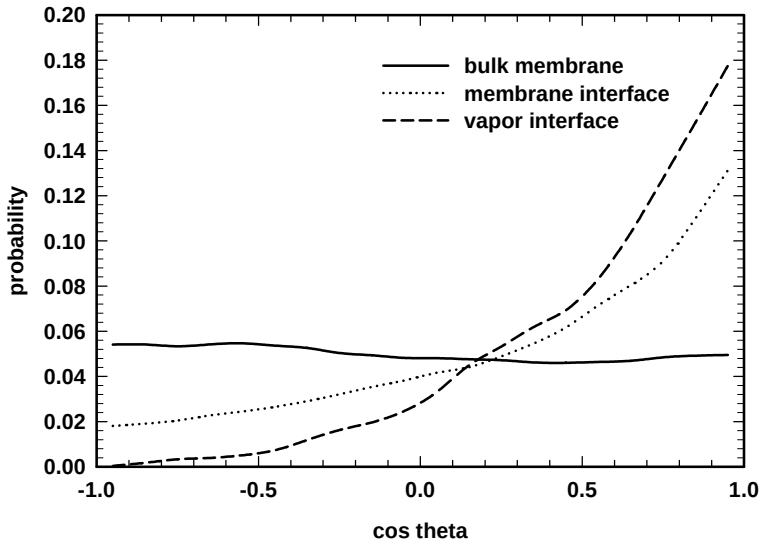


**(b)**

**Figure 2.7.** Probability distribution of the orientation of hydronium ion with respect to the *z* axis (perpendicular to interface) at water contents of **(a)** 5 wt %, and **(b)** 20 wt %. Solid line, bulk membrane; dotted line, membrane interface; and dashed line, vapor interface.

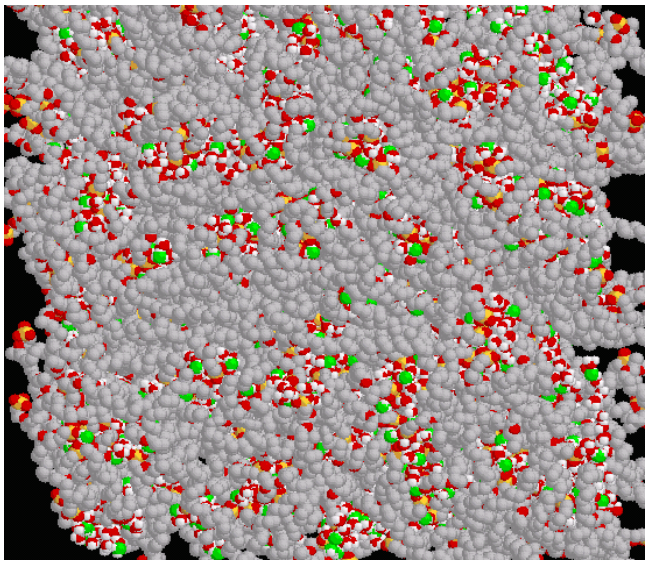

**(a)**

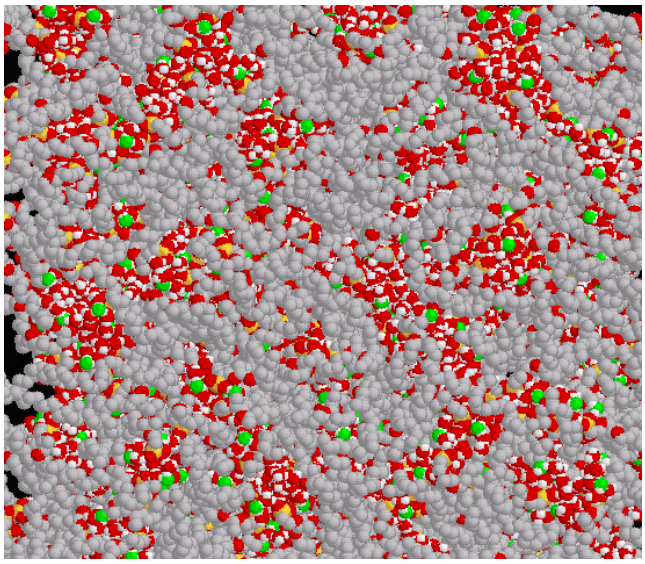

**(b)**

**Figure 2.8.** Snapshot taken normal to the interface from a MD simulation of hydrated Nafion at $T$ = 300 K and nominal water contents of **(a)** 5 wt %, and **(b)** 20 wt %. $CF_2$ and $CF_3$ pseudo-atoms are gray, H are white, S are orange, and O are red, except the O of $H_3O^+$, which are green for emphasis.

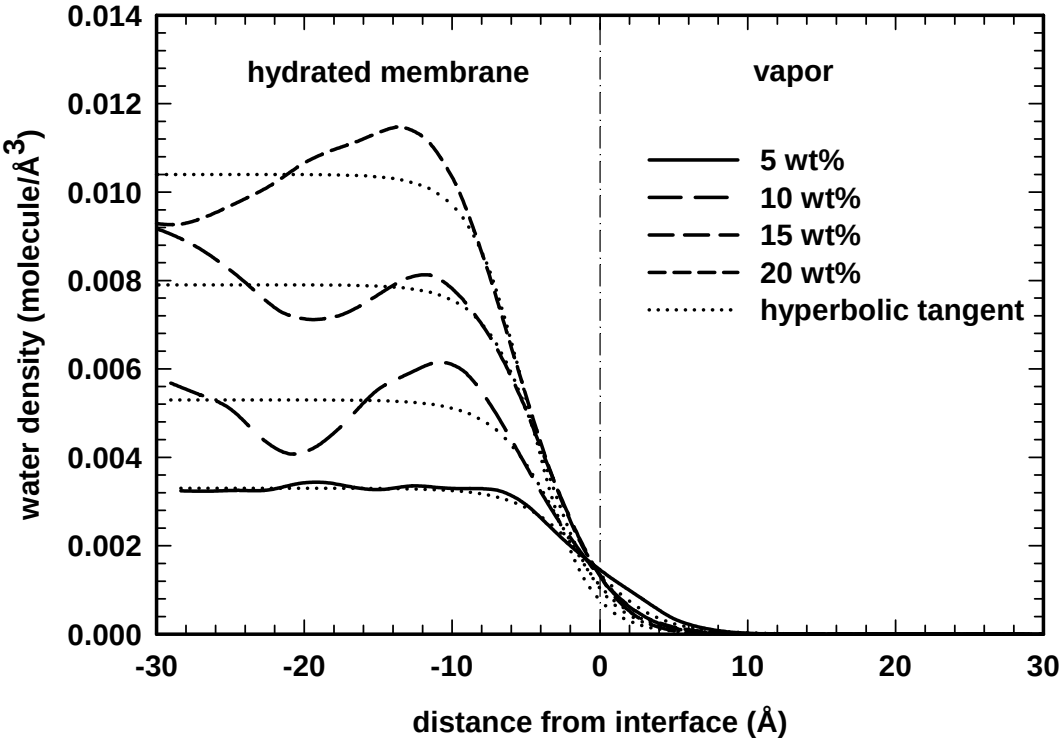


**Figure 2.9.** Density profile for water along the z direction with the hyperbolic tangent fitted for the water contents of 5 wt %, 10 wt %, 15 wt %, and 20 wt %.

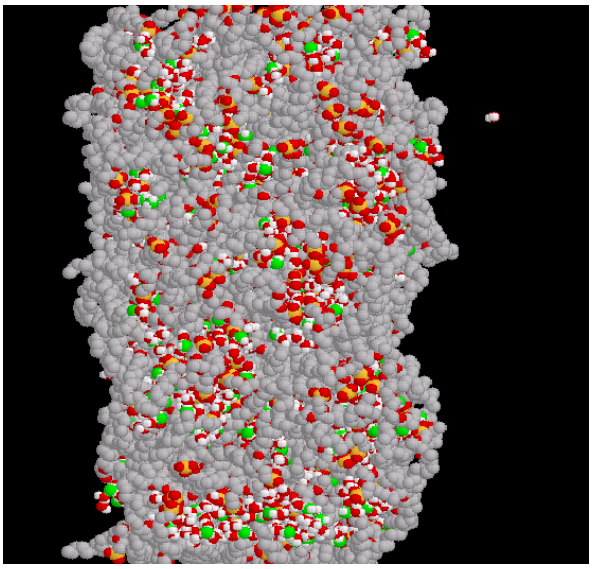

**(a)**

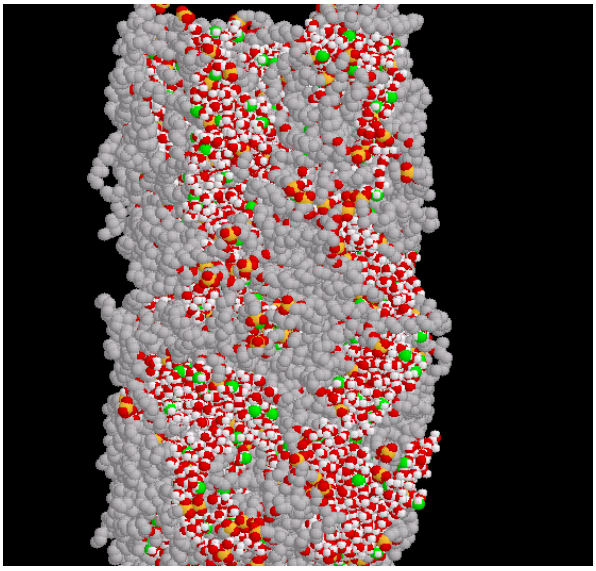

**(b)**

**Figure 2.10.** Snapshot taken parallel to the interface from a MD simulation of hydrated Nafion at $T$ = 300 K and nominal water contents of (a) 5 wt % and (b) 20 wt %. $CF_2$ and $CF_3$ pseudo-atoms are gray, H are white, S are orange, O are red, except the O of $H_3O^+$, which are green for emphasis.

# CHAPTER 3

# A Reactive Molecular Dynamics Algorithm for Proton Transport in Aqueous Systems

This chapter is a slightly revised version of a paper by the same title published in the *Journal of Physical Chemistry C* in 2010 by Myvizhi Esai Selvan, David J. Keffer, Shengting Cui, and Stephen J. Paddison:

Esai Selvan, M.; Keffer, D. J.; Cui, S. T. and Paddison, S. J., "A Reactive molecular dynamics algorithm for proton transport in aqueous systems", *J. Phys. Chem. C* **114**, 11965 (2010).

The use of "we" in this part refers to the co-authors and the author of this dissertation. My primary contributions to this paper include (1) all of the simulation work (2) analysis of data, and (3) most of the writing



**Abstract**

We present a model that incorporates the structural diffusion of a proton into a classical molecular dynamics simulation using a reactive molecular dynamics (RMD) algorithm. The transition state for proton transfer obtained from ab initio calculations is mapped onto a set of geometric and energetic triggers to describe the structural diffusion of the proton in the simulation. Numerical values of these triggers are parametrized to satisfy the experimental values of rate constant and activation energy in order to capture the molecular and macroscopic features of structural diffusion. The algorithm partitions the structural diffusion of a proton into three steps: (i) satisfaction of the triggers, (ii) instantaneous reaction, and (iii) local equilibration. The final step ensures that the ending point of the reaction provides the correct structure and heat of reaction. Hence, the reactivity is incorporated by the algorithm rather than through the development of a reactive potential. We have applied this scheme to study proton transport in bulk water and solutions of HCl. Total charge diffusion along with the structural and vehicular decomposition is studied as a function of temperature (280-320 K). The two components are found to be uncorrelated and the structural diffusion contributes 60-70% of the total charge diffusion in bulk water. The method is applied to HCl solutions (0.22-0.83 M) to study the effect of concentration on proton transport. The reduction in the total diffusivity of the charge with an increase in concentration is due to the reduction in structural diffusion.

## 3.1 INTRODUCTION

The relationship between the hydrated morphology of proton exchange membranes (PEMs), commonly employed as the electrolyte in fuel cells, and proton conductivity continues to be of great interest [1]. A fundamental understanding of this structure–property correlation should enable the effort to develop PEMs with superior performance across a wide range of operating conditions [2,3]. The connection between structure and transport, however, remains unclear [4] due to the uncertainty in the mechanism of proton transport within the aqueous domains of the hydrated membrane. Proton transport in bulk water occurs through a combination of both vehicular diffusion (movement of the center of mass of hydronium ions) and structural diffusion [5,6] (transfer of protons among water molecules). However, it is unclear to what extent these two mechanisms continue to function in a highly acidic and extremely confined aqueous regions of a hydrated PEM [7,8]. There is evidence from theory and simulation suggesting that both proton transport mechanisms are active in PEMs [9-13] with an increase in structural diffusion occurring at high hydration levels [4].

Structural diffusion of a proton involves breaking and forming of covalent and hydrogen bonds, and hence a quantum mechanical (QM) description is warranted to accurately describe this process. Zundel and Eigen cations are two of the predominant solvation complexes of the hydrated proton involved in structural diffusion [5,14]. The proton transport occurs via structural defects due to continual interconversion between covalent and hydrogen bonds with these as the limiting structures [15].

Extensive experimental work has been conducted to study proton transport in water to understand its high mobility. The finding of Eigen [16] and Zundel cations [17] motivated the study of protonated clusters $H^+(H_2O)_n$ (n = 4 to 27), using vibrational predissociation spectroscopy [18-21]. A detailed structural analysis and thermodynamics of these clusters, including their charge delocalization, were obtained from O–H stretching spectral signatures in the region of 0–4000 $cm^{-1}$ and through *ab initio* calculations [22].

Insight into the average residence time of a proton on a water molecule was obtained from NMR spectroscopy. These studies [23-31] determined the activation energy and rate constants for the proton exchange reaction rates using water enriched with $^{17}O$. They were

obtained by measuring the proton spin–lattice relaxation in the rotating frame/low frequency or spin–spin relaxation or $^{17}O$ line widths as a function of temperature and pH using techniques including field-cycling, pulse and spin–echo. Both structure and structural fluctuations were investigated in real time using ultrafast vibrational spectroscopy [32]. Proton rattling along a hydrogen bond was found to take place at a time scale of <100 fs and the interconversion between Eigen and Zundel structures was experimentally observed.

A combination of the results from both simulation and experiments is needed for a clear interpretation of proton transport mechanism. Car–Parrinello *ab initio* molecular dynamics (CPAIMD) simulations [33] were utilized by Tuckerman *et al.* [6,34] to study the structural diffusion of the protons in bulk water. The CPAIMD scheme determines atomic forces "on the fly" from Kohn–Sham density functional theory (DFT) based electronic structure calculations. A detailed description of the transfer of the proton from a $H_3O^+$ ion to an adjacent $H_2O$ molecule, involving the predominant solvation complexes and the dynamics including the time scale and rate limiting step for the structural diffusion, is provided in this approach. An alternate method is to use a mixed quantum and classical dynamics technique to describe the reactivity of the ion in water [35,36]. Part of the system obeys the quantum mechanical description including the $H_3O^+$ ion and the solvation molecules while the rest of the molecules are treated classically in this model. These methods attempt to replicate an accurate description of the proton transport without being as computationally demanding as AIMD simulations.

The empirical valence bond (EVB) approach [37] is a technique where forming and breaking of covalent bonds are described through "states" whose partial charges and interaction potentials are obtained from the lowest energy state of a classical Hamiltonian matrix coupled by the empirical off-diagonal elements. EVB has been used to model proton transport in bulk water [38-42], aqueous and biomolecular systems. A family of EVB models has been introduced in a continual effort to refine and increase the accuracy of the method. By increasing the states represented in the EVB model, *i.e.,* the multi-state empirical valence bond (MS-EVB) [38,42,43], one can enhance the fidelity of the model. The MS-EVB method allows for the delocalization of a proton among several water molecules and the self-consistent iterative (SCI) MS-EVB [44] formulation recognizes multiple protons within the system. The latest improved model with the most accurate description of proton transport is the MS-EVB3 [42,45].

Importantly, all of the EVB methods attempt to include the states from all possible proton transfer reactions into the MS-EVB Hamiltonian. The MS-EVB approach has also been recently applied to study proton transport in Nafion [12,13].

The explicit transfer of the proton from the donor to the acceptor is described by a mixed MD/MC algorithm devised by Schmidt and Brickmann [46] to simulate an excess proton in water. This two-parameter scheme treats the molecules classically through MD and the proton hopping is modeled by introducing a MC step after a distance criterion is satisfied. The hopping probability is based on the energy barrier in the double minimum potential (DMP) and during migration the proton instantaneously jumps from one well of the DMP to the other. The probability parameterization is exclusively done for pure water and hence limits it applicability. Q-HOP MD [47] is a more sophisticated version of this method where the hopping probability instead of being parameterized for each individual system is tied to an analytical formulation of the energy barrier, which includes environmental effect of the surrounding groups. It has been used to study the effects of proton in bulk water and other biomolecular systems [48].

These models have reported structural and dynamical properties of the proton such as lifetime and charge diffusion coefficient that are in good agreement with experimental data. Some of them observed the phenomenon of barrier-less proton rattling [47,49-51] and emphasized the breaking of the hydrogen bond in the second solvation shell as the rate limiting step [34,49,52]. Protonated cluster energetics and geometries were studied and the probable mechanisms of proton transport were discussed.

The various approaches that have been used to model proton transport in bulk water [34-36,38,39,41-43,46,47,49-54] vary by their level of sophistication and accuracy in description of the process. In general, a model would benefit from these features: (1) low computational demand to allow simulation of larger systems over longer times that yields greater statistical reliability of the results and allows coupling of chemical reaction to diffusion and other relaxational processes that occur on longer time scales, (2) easy extension of the model to different systems, and (3) quick development of the algorithm. We believe that a new approach is needed that will allow large scale simulations of proton transport in a hydrated perfluoro sulfonic acid (PFSA) membrane in which all the excess protons are allowed to participate in proton hopping. To our knowledge, such a simulation with currently existing approaches does

not exist. Toward this end, we have developed a classical reactive molecular dynamics (RMD) algorithm that captures the essential molecular and macroscopic features of structural diffusion of a proton. In general, RMD methods can be categorized into those that use reactive force fields [55-58], capable of breaking and forming bonds, and those that use a heuristic approach to move from the potential energy surface of the reactant to the product potential energy surface [59-61]. While our algorithm has unique and original features, it can be categorized with the latter group of RMD methods.

We have parameterized the algorithm to the bulk water system which has the most reliable data (from both *ab initio* and experiments). The sensitivity of the method to its environment has been studied by applying it to aqueous HCl solutions at various concentrations. The paper is organized as follows: Sec. 3.2 gives a detailed description of the model including simulation details and implementation of the algorithm; results are discussed in Sec. 3.3; and finally, conclusions are given in Sec. 3.4.

## 3.2. REACTIVE MOLECULAR DYNAMICS (RMD) ALGORITHM

At the macroscopic level, structural diffusion of a proton is described by the reaction

$$H_3O^+ + H_2O \xleftrightarrow{nH_2O} H_2O + H_3O^+ \tag{1}$$

in which a proton is transferred from a hydronium ion to a water molecule in the presence of $n$ additional water molecules. The reaction rate for the elementary reaction represented in Eq. (1), describing the number of reaction events per volume per time, $r$, is given by

$$r = k\,[H_3O^+][H_2O] \tag{2}$$

where the square brackets indicate concentration and $k$ is the rate constant. This expression has also been used to fit the experimental measurements [23-25] of the relaxation times to the rate of proton exchange in water given by Eq. (1). Typically, $k$ in Eq. (2) is decomposed as

$$k = k_o \exp\left(-\frac{E_{a,f}}{k_B T}\right) \tag{3}$$

where $E_{a,f}$ is the activation energy and $k_o$ is the prefactor in the rate constant that contains both the frequency of attempted reactions as well as the entropic contribution to $\Delta G_{a,f}$, namely

$$k_o = \frac{k_B T}{h} \exp\left(\frac{\Delta S_{a,f}}{k_B}\right) \quad (4)$$

The only remaining macroscopic property of a reaction is the heat of reaction, $\Delta H_r$ .We note that the macroscopic expression for proton hopping rate is capable of reproducing the experimentally observed results, although it does not contain any information regarding the delocalization of the excess proton charge defect over multiple water molecules or other molecular-level details of the process. In other words, the conventional macroscopic model of a chemical reaction contains minimum information regarding the transition state. The RMD algorithm attempts to include a description of the process that is far more detailed than the macroscopic model, but less detailed than a quantum mechanical description. This feature allows the RMD description to capture the effects of the local environment, at least to a first order.

### 3.2.1 Input from Quantum Mechanical Calculations

The description of a chemical reaction in quantum mechanics is a matter of evaluating the structure and free energies of the participating atoms in the reactant, transition state, and product configurations. The identification of the $E_{a,f}$ and $\Delta H_r$ at 0 K is a straightforward matter of determining the energy of the reactant, transition state, and product configurations. The reactant and product are minima in the energy landscape and the transition state is a saddle point. These three configurations are important information that must be mapped onto the RMD algorithm. The mapping of reactant and product configurations is available through nonreactive intramolecular potentials that generate reasonable equilibrium configurations. There are numerous non-reactive potentials for a $H_3O^+$ ion [62-65] and a $H_2O$ molecule [66-69]. Schemes such as EVB describe the reactive process by an empirical potential energy function [38,40]. Our RMD algorithm uses the structures of the ground states and transition state as input to define a set of geometric triggers that must be satisfied in order for the reaction to take place.

### 3.2.2 Input from Macroscopic Model

The macroscopic description of a chemical reaction includes the stoichiometry, rate law, $E_{a,f}$ , $\Delta H_r$ and *k*. Structural diffusion of a proton can be described by the stoichiometry and rate

law given in Eqs. (1) and (2). The $\Delta H_r$ is zero, since the reactants and products are identical. There are numerous sources for the two properties, $E_{a,f}$ and $k$ from simulation [49,53] and experiment [24,25,30,31,70,71]. In this work, we used the rates obtained from the proton magnetic relaxation measurements in $^{17}$O-enriched water using a line broadening technique [25] as reference. Luz and Meiboom represented the proton transfer reaction by Eq. (1) and provided numerical values of the constants in Eq. (3) as $k_o = 6.0\times10^{11}$ L/(mol·s) and $E_{a,f} = 2.4$ kcal/mol. The $E_{a,f}$ is in agreement with other experimental values of 2.4–2.6 kcal/mol [24,70,72] and the $k_o$ is also close to other experimental values [23,30,70,71].

### 3.2.3 Conceptual Implementation

We are motivated to create a generalized RMD algorithm that can be used for any arbitrary chemical reaction. We wish to avoid the extensive and time-consuming reparameterization of the potentials of the reactant and product states, since those mappings already exist in the form of published intramolecular and intermolecular potentials. The RMD algorithm developed here should satisfy both QM and macroscopic descriptions of the reaction. It should recognize that the configuration of the reactants is moving towards the transition state. However, at the same time, guided by the macroscopic model, we wish to include as little information as necessary about the transition state, in order to capture the essential defining features of the reaction. This method has been proven to be successful in other reactions like the thermal decomposition of perfluorodimethyl ether [73].

Our RMD algorithm uses published, non-reactive interaction potentials for the reactants and products. We perform conventional nonreactive molecular dynamics with an added RMD feature, where at the end of each MD time step, we check to see if the reactants satisfy a set of geometric and energetic triggers. These triggers indicate that the reactant is following a trajectory leading to the transition state. In other words, satisfying a set of triggers ensures that one has the correct starting configuration for the reaction to take place. The first step in the RMD algorithm is therefore the satisfaction of a set of triggers. The triggers are tuned to provide the correct $E_{a,f}$ and $k_o$ of the reaction. The second step of the RMD algorithm is the instantaneous reaction. The molecule would never reach the transition state in a classical MD simulation; the nonreactive

potential would not allow it. However, once the complete set of triggers has been satisfied by a given reactant, the RMD algorithm allows the reaction to take place instantaneously while no time is elapsed in the MD simulation. The third and final step of the RMD algorithm is the local equilibration. The change in identity of molecules during the reaction creates a change in structure and energy of the system. Therefore, we perform an equilibration of the local molecules. The objective of the local equilibration is to re-establish a reasonable structure and energy in the system. In other words, local equilibration ensures that one has the correct ending configuration of the products and satisfies the $\Delta H_r$. Once the local equilibration is complete, the MD simulation continues on to the next time step. The details involved in these three steps of the RMD algorithm to describe the reaction in Eq. (1) are discussed later in the paper.

The RMD algorithm describes a procedure that endeavors to have a valid starting point and a valid ending point for the chemical reaction. Information regarding the transition state is embedded in the triggers, but the RMD algorithm makes no attempt to dynamically describe the structure of the transition state. This allows an RMD algorithm parameterized for a reaction in one environment (*i.e.*, bulk water) to potentially function in a second environment (*i.e.*, an aqueous HCl solution or a hydrated PEM or a water filled carbon nanotube [74]) because the starting and ending points of the structural diffusion reaction are likely similar, whereas the details of the transition state may not be. At least, this is a key motivation in developing this RMD algorithm.

Similar methods of allowing instantaneous reaction between titratable sites has been followed by mixed MD/MC [46] and Q-HOP algorithm [47] as discussed in the beginning of the paper. Like RMD, both of these methods are implemented in classical MD simulation. The reaction in our algorithm takes place based on the satisfaction of the six geometric and one energetic trigger, whereas in the Q-HOP MD the occurrence of the reaction is based on the proton transfer probability calculated from the donor-acceptor pair distance and environmental effect of the surrounding group. To reduce the computational cost in Q-HOP the probabilities were calculated only when the separation was less than 3.5 Å and the angle of the hydrogen bond and the angle between the donating atom, transferring proton, and acceptor were greater than 120° were satisfied, which are similar to our geometric triggers. We directly parameterize our triggers to match the experimental rate constant, while in the Q-HOP MD algorithm the

parameterization is performed to obtain faster estimate of the proton transfer rate by fitting an analytical expression for the proton transfer energy barrier. The reaction takes place instantaneously in all the methods where the proton is transferred to the acceptor. We perform an additional step known as local equilibration. So QM information is used in both RMD and Q-HOP algorithms. While the Q-HOP model checks the rate probability using the energy barrier our RMD checks for the favorable configuration and energy.

### 3.2.4 Determination and Parameterization of Triggers

Reaction takes place in the RMD algorithm only if a set of geometric and energetic triggers are satisfied. The determination of the functional form of the triggers comes from a comparison of the QM structures of the ground and transition states. The numerical values of these triggers are fit to the macroscopic measurements of rate.

We identified a set of six geometric triggers and one energetic trigger for the structural diffusion of a proton. A schematic representation of the six geometric triggers is shown in Figure 3.1. The first trigger requires that the distance between the oxygen of the reacting $H_3O^+$, O*, and the oxygen of the reacting $H_2O$ be less than or equal to a cut-off, $r_{O^*O,Zundel,max}$. This first trigger is an obvious and necessary condition for the molecules to move towards the transition state. The second trigger requires that the distance between the proton to be transferred, H* and O* ($r_{O^*H^*,Zundel}$) to be beyond the equilibrium O–H bond distance. The bond distance is determined by the nonreactive potential used in the MD simulation. This trigger acknowledges that our nonreactive potential will not allow the Zundel ion [75] to attain its symmetry, because the H* interacts with the O* through a classical representation of a chemical bond, typically a Hookean spring, and interacts with the O of the $H_2O$, through a combination of Lennard–Jones (LJ) and Coulombic interactions. Nevertheless, the second trigger requires that the H* be moving toward the transition state.

The third trigger requires that the angle formed by the O*, H*, and O of the $H_2O$ ($\theta_{O^*H^*O}$) be nearly linear. This trigger is motivated by the examination of the Zundel [75] and Eigen cations [76] structure. The fourth trigger requires that the angles formed by the H*, the O of the $H_2O$, and each of the two H of the $H_2O$ ($\theta_{H^*OH}$) be near the equilibrium H–O–H bond angles of a

$H_3O^+$ ion. This trigger acknowledges that the water has $sp^3$ bond hybridization. One of the two lone electron pairs in the water must be directed at the incoming H*.

The fifth trigger requires that the $H_3O^+$ ion be properly hydrated. The minimum level of hydration for this reaction can be found in the Eigen ion. This trigger requires that each of the nonreactive H atoms on the $H_3O^+$ ion be within a certain distance of the O of an adjacent nonreactive $H_2O$ ($r_{O*O,Eigen,max}$).This trigger is based on the Eigen ion structure, which is required for the reaction to take place. The sixth and final geometric trigger requires that the $H_2O$ involved in the reaction be properly hydrated ($r_{OO,hydration,max}$). In other words, once the $H_2O$ receives the proton, it becomes a $H_3O^+$ ion at the center of an Eigen ion. This trigger is motivated by the fact that the proton is known to vibrate back and forth in this reaction [15,32,38,46,50,51]. The only way to allow the reverse reaction to occur with any non-negligible probability at all is to force the receiving $H_2O$ to be, by default, in a configuration that can potentially satisfy the reverse reaction. Automatically, the reverse reaction will not occur if during the subsequent MD step any one or more of the geometric and energetic triggers is no longer satisfied. By the implementation of the last two triggers we have assumed Eigen–Zundel–Eigen transition, which is in agreement with the current interpretation of the proton transfer mechanism [14].

Taken together, these six geometric triggers define a configuration in which a $H_3O^+$ ion and a $H_2O$ molecule can be considered to be very close to the transition state. Given the fact that this is a classical description of the QM process, we are satisfied with this mapping. We also note that some of our triggers may be "symptoms" rather than "causes" of proton hopping. Regardless, as long as the triggers represent necessary and sufficient conditions for the reaction to take place it is immaterial whether the triggers are "symptoms" or "causes" and the approach is valid.

There is one energetic trigger in addition to these six geometric triggers. The energetic trigger requires that the H* has sufficient energy to overcome the activation barrier associated with the reaction. This trigger will provide the temperature dependence to the reaction rate that is characteristic to a reaction with an activation barrier. We provide a schematic of the energetic trigger in Figure 3.2. According to the QM description of structural diffusion there is a continuous and finite energy surface along which the proton travels. We also show a parabolic energy surface representing the harmonic bond between the H* and O*. The nonreactive

potential will not allow the H* to reach the transition state. However, we can evaluate if the total energy possessed by the H* is sufficient to overcome that barrier. The total energy in this simple 1-D picture is composed of the potential energy due to the stretching of the bond and the kinetic energy. However, in the real simulation the total energy, $E_{H^*}$ experienced by the H* is composed of all components of the potential energy and kinetic energy. $E_{H^*}$ can be represented as follows:

$$E_{H^*} = V_{H^*}^{intra} + \sum_{j \neq H_3O^+}^{N} V_{H^*,j}^{inter} + E_{k,H^*} \tag{5}$$

where the $V_{H^*}^{intra}$ term is the intramolecular potential of the H* defined by bond bending and bond stretching interactions. The $V_{H^*,j}^{inter}$ term is the intermolecular potential (both LJ and electrostatic interactions) between H* and all other molecules ($j$) in the system. $E_{k,H^*}$ is the kinetic energy of H* projected along the linear axis (O*–H*–O) shown in Figure 3.1(c). This total energy is considered in the energetic trigger.

As mentioned earlier the RMD algorithm naturally incorporates the local environment into the molecular simulation, in such a way that at least the first-order effects of the change in environment are automatically accounted for. For example, in a minimally hydrated PFSA membrane and other model systems, the hydrated protons may exist as Zundel and/or Eigen cations like configurations [77-79] with the O of the sulfonic acid groups that can be immediately accounted for by our geometric and energetic triggers. Geometric triggers 5 and 6, which check for adequate hydration, can just as easily accommodate the hydration via a sulfonic acid group as they can via a water molecule. Furthermore, the energetic trigger is inherently sensitive to the difference in interactions due to the sulfonic acid and water entities.

Once the functional form of the set of six geometric triggers and one energetic trigger has been established, the numerical values of the triggers must be adjusted to generate the correct rate of reaction. The procedure for performing this parameterization of the triggers is iterative. Each iteration involve a fixed set of trigger values and a set of RMD simulations at 5 temperatures, 280, 290, 300, 310, and 320 K. By recording the number of reactions that took place, one can determine the reaction rate. Since this is done at multiple temperatures, one can obtain the $E_{a,f}$ and $k_o$ in Eq. (3) from the regression of an Arrhenius plot. If the values of $E_{a,f}$ and

$k_o$ are within a tolerance of the target values, parameterization is complete, and if the values are outside the tolerance, a new iteration is begun with an updated set of trigger values.

Unlike the parameterization of a reactive potential, in this RMD algorithm we minimize the number of parameters that must be fit because we parameterize only a few triggers. Avoiding the reactive potential parameterization in favor of using existing nonreactive potentials of the reactants and products is a concept that has been successfully used before [59]. Our parameterization is essentially an exercise in multivariate nonlinear optimization but the optimum that is found could be a function of the initial guess. A basic understanding of the nature of the parameters allows us to select a good set of initial guess values which makes the iterative process easier. Though the choice of the geometric parameters is based on the transition and ground state from QM, the numerical values are from the classical MD studies. Triggers 2 and 4 can be determined by the TIP3P water model. Other triggers, such as the hydration distances used in triggers 5 and 6, are based on the RDFs from the simulation of a nonreactive system. The energetic trigger greatly influences the activation energy. The experimental target value of $E_{a,f}$ of 2.4 kcal/mol requires the ratio of the experimental $k$ at 320 K over 280 K to be 1.71 [25]. The energy distribution of the proton in a $H_3O^+$ ion satisfying all six geometric triggers at these temperatures is illustrated in Figure 3.3. The distribution shifts to higher energies as the temperature increases. The energetic trigger is chosen initially such that the ratio of areas under the curve to the right of the trigger value satisfies the experimental ratio of reaction rates. As the trigger energy value is increased the ratio of the area under the curves at 320 K over 280 K increases. Based on the fact that

$$\frac{k_{320}}{k_{280}} \approx \frac{Area_{320}}{Area_{280}} = 1.71 \tag{6}$$

we can have an estimate of the energetic trigger. Using this information we started the parameterization with very good initial set of trigger values. Therefore, only a few iteration steps were needed to match the rate constants to that of the experimental values. At the end of the trigger parameterization, we had a set of triggers that provided rate constants within an acceptable tolerance (6%) of our target values. To conclude this discussion the numerical value of triggers and their initial guesses are listed in Table 3.1. We also see that the trigger values are

reasonably close to the initial guesses, as should be the case, since we are mapping the QM results onto a reasonable classical potential.

### 3.2.5 Local Equilibration

If a $H_3O^+$ ion satisfies all the geometric and energetic triggers, the reaction takes place instantly. The reaction for structural diffusion involves replacing the bond-stretching (harmonic) interaction of the O* and H* with a nonbonded interaction. The reverse switch is made for the reactant $H_2O$ and H*. The proton to be transferred is moved along the O*O axis such that the ratio of O*–H* and O–H* distances are the same in the product molecules as they were in the reactant molecules. Each reaction causes a change in the potential energy of the system due to the rigid potential models used.

The purpose of the local equilibration is to adjust the position of the atoms in such a way that the system is not affected energetically and structurally after the reaction. Therefore, our method of local equilibration has an objective function that has a weighted combination of both energetic (satisfaction of the heat of reaction) and structural (restoration of a structure with a reasonable hydrogen bonding network) components. There is a need to adjust molecule positions because the O–O radial distribution function (RDF) for $H_2O$–$H_2O$ is different than that for $H_3O^+$–$H_2O$. For example, the first peak in the O($H_2O$)–O($H_2O$) RDF is at 2.8 Å, whereas the first peak in the O($H_3O^+$)–O($H_2O$) is at 2.55 Å. If we do not perform any local relaxation at all, then our reaction in Eq. (1) is more specifically

$$H_3O^+_{(2.55)} + H_2O_{(2.8)} \xleftrightarrow{n H_2O} H_2O_{(2.55)} + H_3O^+_{(2.8)} \tag{7.a}$$

where the subscripts indicate first peaks in the RDF. The reactants are in a nonequilibrium configuration. The objective of the local relaxation is to satisfy the heat of reaction and the equation

$$H_3O^+_{(2.55)} + H_2O_{(2.8)} \xleftrightarrow{n H_2O} H_2O_{(2.8)} + H_3O^+_{(2.55)} \tag{7.b}$$

where the reactants are properly hydrated and are part of an equilibrium hydrogen-bonding network. There is evidence that the rate limiting step in proton transport involves the restructuring of the hydrogen bonding network in the solvation shells around the excess charge [14]. Therefore, we equilibrated the proton transferred and the four hydrating molecules, as

shown in triggers 5 and 6 of Figure 3.1 (panels e and f). The objective function, $F_{\text{obj}}$, can be defined by the root-mean-square (RMS) error of the energy difference, $\Delta U^{\text{RMS}}$, and structural difference, $\Delta g(r)^{\text{RMS}}$, with weighing factors, $w_1$ and $w_2$, to each term as follows

$$F_{\text{obj}} = w_1 \Delta U^{\text{RMS}} + w_2 \Delta g(r)^{\text{RMS}} \tag{8}$$

The energetic component of the objective function, $\Delta U^{\text{RMS}}$, is calculated as the difference between the instantaneously calculated energy of the entire system before reaction, $U_{\text{before}}$, and after equilibration, $U_{\text{after}}$:

$$\Delta U^{\text{RMS}} = \sqrt{\left( \frac{U_{\text{after}} - U_{\text{before}}}{U_{\text{before}}} \right)^2} \tag{9}$$

The structural component of the objective function, $\Delta g(r)^{\text{RMS}}$, is given by the following equation:

$$\Delta g(r)^{\text{RMS}} = \sqrt{\frac{1}{N_{\text{pairs}}} \sum_{j=1}^{j=N_{\text{pairs}}} \left( \frac{r_{ij} - r_{ij}^{\text{target}}}{r_{ij}^{\text{target}}} \right)^2} \tag{10}$$

where $r_{ij}$ refers to the distance between the atoms *i* and *j* and $N_{\text{pairs}}$ refers to each such pair of atoms. From initial study, we chose $N_{\text{pairs}} = 12$ and $r_{ij}^{\text{target}}$ is based on the location of peaks in the RDF between the atoms *i* and *j* in an analogous nonreactive simulation. The diagrammatic representation of $N_{\text{pairs}}$ and the values of $r_{ij}^{\text{target}}$ are shown in Figure 3.4 and listed in Table 3.2. It is true that there are more potential definitions for the objective function and varying approaches for the execution of the local equilibration. For example, one could relax the positions of the atoms in just the two reacting molecules. Alternatively, one could relax all the molecules within a given proximity of the reaction. One way to confirm our choice of procedure for this particular system is to compare the water diffusivities from both reactive and nonreactive systems. Experimentally, the protons do not affect the self-diffusion coefficient of water at dilute concentrations [80]. Therefore, we expect the water diffusivity to remain unaffected by the introduction of the RMD algorithm and more specifically by the local equilibration, which can affect the hydrogen bond dynamics in the vicinity of the proton complex. In the first

investigation, since the described method of local equilibration satisfied the above criterion, we studied and parameterized the system with no further refinement of the local equilibration.

### 3.2.6 Systems Simulated

As mentioned earlier both $H_2O$ molecule and $H_3O^+$ ion were modeled with non-reactive potentials. The $H_2O$ molecules used the TIP3P model [67] with flexible OH bonds [81] while the $H_3O^+$ ion was represented using the same TIP3P model with modified charges on the O and H atoms [65]. In spite of the availability of various non-reactive potentials for a $H_2O$ molecule [66-69] and a $H_3O^+$ ion [62-64], we chose the above to be consistent with our previously studied systems [82,83] and to facilitate extension of the algorithm to those systems. The system contained 650 molecules of water along with one $H_3O^+$ ion for an infinite dilute concentration. NVT simulations were performed at temperatures 280, 290, 300, 310, and 320 K with experimental water densities of 0.9999, 0.9988, 0.9965, 0.9932, and 0.9891 g/cm$^3$, respectively [84]. The intermolecular interactions included the LJ and Coulombic interactions within a cutoff radii of 10 Å. Electrostatic interactions were calculated using the reaction field method [85] and long-range correction for LJ interactions was taken into account. Nosé–Hoover thermostat [86-88] was incorporated to maintain a constant temperature but with a slightly higher frequency of 0.01 fs$^{-1}$ to remove the excess heat that was not removed by the local equilibration after the reaction. The equations of motion were integrated using the two time scale r-RESPA [89] with a large time step of 2 fs and a small time step of 0.2 fs. The Polak–Ribiere conjugate gradient method [90] was used to perform the nonlinear multivariate optimization of the objective function. The weighing factors, $w_1$ and $w_2$, were chosen as 1 and 10, respectively. For better statistics 160 simulations were run at each temperature with different initial configurations. All the simulations had their initial configurations equilibrated for 0.6 ns and were run for 1 ns for data collection.

Pure water simulations were conducted to benchmark the water diffusivities of the TIP3P water model. We performed simulations of nonreactive systems in which the RMD algorithm was not implemented (absence of structural diffusion) to compare the diffusion of water in both reactive and nonreactive systems and also to compare the diffusion of the $H_3O^+$ ion with the vehicular component of the charge in the reactive system. Finally, to prove the environmental

adaptability of the algorithm, the RMD algorithm was incorporated to a completely dissociated hydrochloric acid system ($H_2O$, $H_3O^+$ and $Cl^-$) at 300 K at various concentrations of 0.22, 0.44, and 0.83 M with 15 $H_3O^+$, 15 $Cl^-$ and 3750, 1875, and 975 molecules of $H_2O$, respectively. The LJ parameters of $Cl^-$ were $\sigma$ = 4.4 Å and $\varepsilon/k$ = 50.325 K.

### 3.3 RESULTS AND DISCUSSION

The rate constants of the reaction, water diffusion coefficients, and a detailed study of the components of charge diffusion are discussed below. These results also help to validate the algorithm and understand the structural diffusion of the proton as a function of temperature and concentration.

#### 3.3.1 Rate Constant

The trigger values were tuned to match the rate constant, *k*, obtained from simulation to that of the experimental value [25]. The *k* is calculated using the expression,

$$k = \frac{\mathrm{N_{react}}}{\mathrm{time} \cdot \mathrm{V_{box}}} \times \frac{1}{[\mathrm{H_2O}][\mathrm{H_3O^+}]} \tag{11}$$

where $V_{\mathrm{box}}$ is the simulation box volume, $N_{\mathrm{react}}$ is the number of reacted molecules, "time" is the length of the simulation, and the squared brackets represent the concentration. There is one important note to consider in the process of counting $N_{\mathrm{react}}$, namely "proton rattling". As mentioned earlier, it has been noted that the proton vibrates between water molecules. The time scale associated with this vibration is on the order of 100 fs [32]. The macroscopic equation to which we are fitting has no such temporal resolution. Each forward and reverse motion of a vibrating proton does not constitute an independent reaction event, at least not at the macroscopic scale. Therefore, if a proton started on molecule *i* and was vibrating between molecule *i* and molecule *j*, we considered it to be a single reaction, irrespective of the molecule (*i* or *j*) the proton rests at the end of vibration. A sequence of vibrations was said to have ended if either molecule *i* or molecule *j* subsequently participated in a reaction with another molecule. This interpretation is consistent with the experimental data, which are providing the target $E_{\mathrm{a,f}}$ and $k_{\mathrm{o}}$ (during parameterization), since these experiments did not have femtosecond resolution

while measuring the relaxation time [23,30,70,71]. The rate constant calculated from simulation along with experimental values [25] are represented in Figure 3.5. These values were used to generate an Arrhenius plot from which the activation energy, $E_{a,f}$ and the rate constant prefactor, $k_o$, listed in Table 3.3, were obtained. The values of $E_{a,f}$ and $k_o$ are within 20% and 135% of the experimental value, respectively, which corresponds to fitting $k$ within 6% of the experimental value.

An activation energy of 2.7 kcal/mol [49] obtained from an Arrhenius plot using the total diffusion coefficient of the proton was reported by another group that employed MS-EVB2 to study the temperature dependence of the proton mobility. A similar study was carried out by Walbran and Kornyshev [53]. They obtained an activation energy of 2.5 kcal/mol and their absolute value of the diffusivity was lower than the experimental value. The rate constant can also be expressed in terms of proton lifetime. The average lifetime of a proton at 300 K from other simulations corresponds to 1–2 ps [38,47,50] and our value is fit to 1.7 ps.

The probability that each trigger was satisfied is provided and discussed in detail in the Appendix B. The most stringent trigger, in terms of eliminating the largest fraction of $H_3O^+$ ions from reaction is the energetic trigger.

### 3.3.2 Charge Diffusivity

Once we have parameterized the triggers to fit the reaction rate, the diffusion of the charge can be studied. We should point out that, while the reaction rate is a fit, the diffusivity and its decomposition are predictions of the model and are explicitly determined. Thus by tuning the reactive nature of the proton, the transport property of the charge is predicted by the model.

The total diffusivity of the charge can be determined without any ambiguity. The excess proton sits on a $H_3O^+$ ion, which has a center-of-mass position. By following each charge individually, we can create a trajectory as a function of time composed of the center-of-mass position of whichever molecule the specific charge is currently covalently bound. The Einstein relation relates the total diffusivity to the mean square displacement, $\left\langle \left[ r(t+\tau) - r(t) \right]^2 \right\rangle$,

$$D_{tot} = \lim_{\tau \to \infty} \frac{\left\langle \left[ r(t+\tau) - r(t) \right]^2 \right\rangle}{2d\tau} \tag{12}$$

where $d$ is the dimensionality of the system and $\tau$ is the observation time.

The decomposition of the total charge diffusivity into vehicular and structural components is not without some arbitrary choice. We enforce the constraint that at each step, the total change in position of the charge must be equal to the sum of the displacement vectors attributed to vehicular and structural components.

$$\Delta\vec{r}_{\text{tot}} = \Delta\vec{r}_{\text{veh}} + \Delta\vec{r}_{\text{struct}} \tag{13}$$

During steps in which a charge does not undergo reaction, the entire displacement is categorized as vehicular and when the charge is transferred from one molecule to another, the decomposition is defined as follows. The displacement of the molecule by the classical MD step before reaction is considered as the vehicular contribution and the displacement of the reactant $H_3O^+$ ion from the pre-reaction location to the final position of the product $H_3O^+$ ion after the local equilibration is taken as the structural displacement. Therefore, the vehicular displacement is continuous while the structural trajectory of a proton remains unchanged in the absence of a reaction. Similar decomposition of the total displacement into continuous and discrete displacements and the analysis of the components of charge diffusion have been done earlier [91].

### *3.3.2.a Structural Diffusion*

An estimate [5,23] of the structural component of the charge diffusivity can be obtained using the Einstein relation:

$$D_{\text{struct}}^{\text{est}} = \frac{\left\langle \left[ r\left(t+\tau_{\text{struct}}\right) - r\left(t\right) \right]^2 \right\rangle_{\text{struct}}}{6\tau_{\text{struct}}} \tag{14}$$

where $\tau_{\text{struct}}$ is the proton lifetime and $\left\langle \left[ r\left(t+\tau\right) - r\left(t\right) \right] \right\rangle_{\text{struct}}$ is the hopping length. $\tau_{\text{struct}}$ is calculated from the experimental $k$ [25], as 1.3, 1.5, 1.7, 2.0, and 2.3 ps at the temperatures 320, 310, 300, 290, and 280 K respectively using the following relationship.

$$\tau_{\text{struct}} = \frac{1}{k[\text{H}_2\text{O}]} \tag{15}$$

We have chosen the mean displacement as 2.65 Å, which is the average distance between O*–O of the two reacting molecules for the $r_{\text{O*O,Zundel,max}}$ trigger of 2.8 Å. The above estimate assumes each reaction causes a net displacement of the proton but our definition of reaction does not

support this assumption. There is a net movement of the proton only when there is odd number of rattles (when a proton from molecule *i* ends in molecule *j* after vibrating) and if the proton rattles even number of times the net displacement for that reaction is zero since the proton ends up in the same parent water molecule. Therefore, $D_{\text{struct}}^{\text{est}}$ can be considered as the upper limit for the estimated structural component, while a lower limit, $D_{\text{struct}}^{\text{est,low}}$, can be determined with only the fraction of reactions that contribute to the structural diffusion in the simulation. For this purpose, $\tau_{\text{struct}}$ was calculated from *k* determined using only the reactions with odd number of rattles in the simulation (which is different from the *k* used for parameterization). Figure 3.6 shows the estimated upper and lower limits, along with the structural component of the charge diffusivity from the simulation. The calculated structural component of the total charge diffusion is within the estimated limits.

We note that, as in any MD simulation, the self diffusion of the proton in water is calculated based on the Einstein relation. In our simulations the total, structural, and vehicular displacements were saved every 200 fs. As a result whether the reaction takes place instantaneously or over time only the cumulative displacement in a specified time interval of 200 fs is being saved. Therefore the approximation that the reaction is instantaneous should not impact our value of the self-diffusion coefficient.

### *3.3.2.b Vehicular Diffusion*

Earlier studies [5,50,51] defined the intrinsic diffusivity as $D_{\text{int}} = D_{\text{tot}} - D_{\text{W}}$ where $D_{\text{W}}$ is the pure water diffusivity. This equation has two assumptions. First, it equates the vehicular component of the $H_3O^+$ ion diffusivity to the diffusivity of water and, second, it assumes that the vehicular and structural components are completely uncorrelated and thus can be added. While it is true that the displacement is additive (as in Eq. (13)), the diffusivity is not in general additive. We can check the validity of both these assumptions in the simulations.

The first assumption is easy to check. The self-diffusivity of each component is in general different [92] in a mixture. For the example of $H_3O^+$ ions in water, the suggestion [72] that the vehicular component of the $H_3O^+$ ion [93] is equal to the diffusivity of water [94] is still unclear [95]. The strong hydrogen bonds surrounding the $H_3O^+$ ion [96] might contribute to a

much smaller component relative to water diffusivity. We can also perform a simulation of nonreactive $H_3O^+$ ions in water and directly measure the vehicular diffusivity of the ion and the diffusivity of water. These are shown in Table 3.4. From these results we see that the vehicular component of the charge diffusivity is not necessarily equal to the diffusivity of water in a TIP3P model. In the nonreactive simulation, the $H_3O^+$ ion diffusivity is about 54% of the diffusivity of water at 300 K. This can be compared with the "conventional" hydronium diffusion ($2.1 \times 10^{-5}$ $cm^2/s$) obtained using 1 state MS-EVB2 model, which is about 66% of pure water ($3.2 \times 10^{-5}$ $cm^2/s$) [43].

We can also conclude from the table that there is a substantial discrepancy between the self-diffusivity of TIP3P water molecule and the experimental measurements [97,98] as has been known for TIP3P [99]. This disagreement in the water diffusivity is not debilitating to the purpose of this work, but it must be accounted for. Therefore, when we compare our diffusivity of water, the relevant comparison is the pure TIP3P water simulations.

The second assumption, namely that the vehicular and structural components of the charge diffusion are uncorrelated, can also be checked. If one substitutes Eq. (13) into Eq. (12) then

$$D_{\text{tot}} = \lim_{\tau\to\infty} \frac{\left\langle \Delta\vec{r}_{\text{veh}}^{\,2} \right\rangle + \left\langle \Delta\vec{r}_{\text{struct}}^{\,2} \right\rangle + 2\left\langle \Delta\vec{r}_{\text{veh}} \Delta\vec{r}_{\text{struct}} \right\rangle}{2d\tau} \tag{16}$$

If one makes the arbitrary but reasonable definition of decomposition that

$$D_{\text{veh}} \equiv \lim_{\tau\to\infty} \frac{\left\langle \Delta\vec{r}_{\text{veh}}^{\,2} \right\rangle}{2d\tau} \tag{17.a}$$

$$D_{\text{struct}} \equiv \lim_{\tau\to\infty} \frac{\left\langle \Delta\vec{r}_{\text{struct}}^{\,2} \right\rangle}{2d\tau} \tag{17.b}$$

$$D_{\text{corr}} \equiv \lim_{\tau\to\infty} \frac{2\left\langle \Delta\vec{r}_{\text{veh}} \Delta\vec{r}_{\text{struct}} \right\rangle}{2d\tau} \tag{17.c}$$

then the conventional assumption is valid only if $\left\langle \Delta\vec{r}_{\text{veh}} \Delta\vec{r}_{\text{struct}} \right\rangle$ is zero. We will discuss this below.

We can generate an estimate of the expected vehicular component, $D_{\text{veh}}^{\text{est}}$, based on the experimental total diffusivity [100,101] and the $D_{\text{struct}}^{\text{est}}$ from the previous section using the following relationship to confirm our $D_{\text{veh}}$.

$$D_{\text{total}}^{\text{expt}} = D_{\text{veh}}^{\text{est}} + D_{\text{struct}}^{\text{est}} \tag{18}$$

The vehicular diffusion components from the nonreactive system, reactive system and the estimated $D_{\text{veh}}^{\text{est}}$ are plotted in Figure 3.7. As it can be seen, the estimated vehicular component and our vehicular component of the charge diffusion agree well. We also find the $H_3O^+$ ion diffusion from the nonreactive system and vehicular component of the charge diffusion to be almost same. We note that using EVB, a nonreactive hydronium (1-EVB state) self-diffusion coefficient has been reported as $2.1 \times 10^{-5}$ $cm^2/s$ [43] and a vehicular component of the total charge self-diffusion coefficient from a reactive system (MS-EVB2) can be determined to be $1.2 \times 10^{-5}$ $cm^2/s$ [91] (from Figure 8 [91]). Thus the equality of these two numbers appears to depend upon the simulation method. In the case of RMD, the equality of the vehicular contribution of the charge diffusion in the reactive system and the diffusion of the hydronium ion in the non-reactive system can be attributed to the fact that we are modeling the reaction given in Eq. (7.b) rather than Eq. (7.a). The reaction in (7.b) has an equilibrated solvation shell, whereas the reaction in (7.a) has a perturbed, nonequilibrium solvation shell that persists for short times. A more detailed comparison based on the relative hydronium ion/water correlation function is given in the Appendix C.

### *3.3.2.c Total Charge Diffusion*

Figure 3.8 shows the experimental charge diffusivity [100,101] along with the diffusivity obtained from simulation. As one would expect the system has lower diffusion coefficients than the experimental values because of the low structural component.

Apart from the qualitative and quantitative agreement of the total, structural, and vehicular diffusivities to the reference value, the relationship among the three is also important. The correlation term $\Delta\vec{r}_{\text{veh}} \times \Delta\vec{r}_{\text{struct}}$ calculated for the system at 320 K is plotted in Figure 3.9 as a function of time. The term is found to fluctuate around zero, implying the components of the

charge diffusion are uncorrelated. The structural component contributes 60–70% of the total charge diffusion coefficient.

### 3.3.3 Water Diffusivity

The change in the identity of the molecules during the reaction makes it difficult to calculate the water diffusivity using the Einstein relation based on the normal data collection method. Therefore instead of calculating the diffusivity through the entire simulation involving reactions we calculated the water diffusivities for time segments in which they did not react. The water diffusion coefficients in the pure system ($N$ = 650) are listed in Table 3.4. The values within the parenthesis refer to the diffusivities from classical MD simulations using flexible TIP3P water models in a system of 216 molecules by Markovitch and Agmon [102]. We find our diffusivities consistently higher than their value because of the finite-size effect ($N$ = 216 vs. 650) on diffusion coefficients [103] due to hydrodynamic interactions in a system with periodic boundary conditions. The diffusivity of water is expected to be the same in the nonreactive and reactive systems since the diffusion of the protons do not affect the self-diffusion coefficient of water [80] at a dilute concentration. We have compared the water diffusivities of the nonreactive system, reactive system, and pure water simulations to that of the experimental water diffusivity [97,98] in Figure 3.10. As noted before, we see that the TIP3P model has a higher diffusivity than the experimental value even in pure water. Therefore the pure water diffusivities from the simulation are used as the reference values for the diffusivities in the reactive system. The water diffusivity in the nonreactive and reactive system compares well with the water diffusivity in the pure water system.

### 3.3.4 Concentration Dependence

The RMD algorithm is sensitive to the environment due to the energetic and geometric triggers. To evaluate the sensitivity of the algorithm to the environment we studied aqueous HCl systems at 0.22, 0.44, and 0.83 M at 300 K. The experimental conductivities [100] per unit concentration were found to decrease with an increase in concentration. Diffusivity of an ion can be related to its conductivity through the following relationship [104]:

$$D = \left( \frac{RT}{|z|^2 F^2} \right) \frac{\sigma}{c} \tag{19}$$

where $c$ is the concentration, σ is the conductivity, and the rest of the symbols have their usual meaning. Figure 3.11 shows the diffusivity calculated from experimental conductivity [100] along with the total and structural component of the charge diffusivity obtained from the simulation at various concentrations. The diffusivities are represented as a ratio to their corresponding total charge diffusivity at infinite dilution. Since the vehicular component is not strongly affected by the difference in the concentration, it has not been plotted. The total charge diffusivity from the simulation follows the same trend as in the experiment but at higher concentration they are steeper and lower than the expected value. The structural component of the charge diffusivity decreases as the concentration increases, which is similar to the trend followed by the total charge diffusivity. Thus the concentration dependence of the charge diffusivity can be attributed to changes in the structural contribution. The two important triggers responsible for the decrease in structural diffusion of the protons in the simulation are the energetic trigger and the geometric trigger that checks the hydration of the $H_3O^+$ ion. The presence of the chloride ion affects the surroundings of an Eigen cation both structurally and energetically leading to the reduction in the probability of a reaction occurring and thus lowers the structural contribution to the charge diffusion. Therefore, our algorithm is capable of aiding the reactants in identifying its local environment which makes it very promising for application in other concentrated systems like the PFSA membrane where confinement and charged anions might play important roles in the charge diffusion.

## 3.4 CONCLUSIONS

We have implemented a new RMD algorithm to study proton transport in aqueous systems. The reactive part of the algorithm is composed of three steps: (i) satisfaction of the triggers, (ii) instantaneous reaction, and (iii) local equilibration. The transition state for structural diffusion, as determined by *ab initio* calculations, is embedded into the triggers. The numerical values of these triggers are parameterized to satisfy experimentally determined values of the rate constant and activation energy. The final step ensures that the ending point of the reaction provides the correct structure and heat of reaction.

We have successfully fit the experimental values of the rate constant, activation energy, and heat of reaction for proton transport in bulk water in the temperature range of 280–320 K. By fitting the reaction rate, this model can be used to predict the total diffusivity of the charge. A study of its decomposition into structural and vehicular components was conducted. We confirm that these two components are uncorrelated at all temperatures. The structural component of the charge diffusivity in bulk water is within the limits of the estimated value from Einstein relation and the vehicular component of the charge diffusivity is equal to the hydronium ion diffusion coefficient in the nonreactive system. The overall picture of the roles of vehicular and structural diffusion can be clearly understood in spite of the total charge diffusivity being lower than the experimental value. We find that the structural diffusion contributes between 60 and 70% to the total charge diffusion at various temperatures in bulk water.

The dependence of the total charge diffusion coefficient on the concentration of HCl was also studied. Structural diffusion decreases with increasing HCl concentration, resulting in a decrease in the total charge diffusion. The presence of the chloride ion disrupts the environment of an Eigen ion both structurally and energetically, reducing the probability of the reaction leading to structural diffusion.

Our RMD approach has several advantages. It uses the computationally efficient classical molecular dynamics with the non-reactive potential that already exists and has been optimized. The algorithm is sensitive to its environment and has shown to qualitatively predict the effect of pH on charge diffusion in aqueous HCl. We are able to capture the correct trend of decrease in the diffusivity with an increase in the concentration. The adaptability of the algorithm to its local environment enables the application of the methodology to proton transport in water filled carbon nanotubes [74] and can be further extended to hydrated PFSA membranes.

## 3.5 ACKNOWLEDGMENTS

The work is supported by the U.S. Department of Energy BES under contract DE-FG02-05ER15723. This research used resources of the Center for Computational Sciences at Oak Ridge National Laboratory, which is supported by the Office of Science of the DOE under contract DE-AC05-00OR22725. This research also used resources of the National Institute for Computational Sciences (NICS) supported by NSF with agreement number OCI 07-11134.

# References

[1] Elliott, J. A. and Paddison, S. J., *Phys. Chem. Chem. Phys.* **9**, 2602 (2007).

[2] Kreuer, K. D., *ChemPhysChem* **3**, 771 (2002).

[3] Roziere, J. and Jones, D. J., *Ann. Rev. Mater. Res.* **33**, 503 (2003).

[4] Kreuer, K. D., *J. Membr. Sci.* **185**, 29 (2001).

[5] Agmon, N., *Chem. Phys. Lett.* **244**, 456 (1995).

[6] Tuckerman, M.; Laasonen, K.; Sprik, M. and Parrinello, M., *J. Chem. Phys.* **103**, 150 (1995).

[7] Kreuer, K. D., *Solid State Ionics* **136**, 149 (2000).

[8] Paddison, S. J., *Ann. Rev. Mater. Res.* **33**, 289 (2003).

[9] Zawodzinski, T. A.; Springer, T. E.; Davey, J.; Jestel, R.; Lopez, C.; Valerio, J. and Gottesfeld, S., *J. Electrochem. Soc.* **140**, 1981 (1993).

[10] Kreuer, K. D., *Solid State Ionics* **97**, 1 (1997).

[11] Paddison, S. J. and Paul, R., *Phys. Chem. Chem. Phys.* **4**, 1158 (2002).

[12] Seeliger, D.; Hartnig, C. and Spohr, E., *Electrochim. Acta* **50**, 4234 (2005).

[13] Petersen, M. K.; Wang, F.; Blake, N. P.; Metiu, H. and Voth, G. A., *J. Phys. Chem. B* **109**, 3727 (2005).

[14] Markovitch, O.; Chen, H.; Izvekov, S.; Paesani, F.; Voth, G. A. and Agmon, N., *J. Phys. Chem. B* **112**, 9456 (2008).

[15] Marx, D.; Tuckerman, M. E.; Hutter, J. and Parrinello, M., *Nature* **397**, 601 (1999).

[16] Wicke, E.; Eigen, M. and Ackermann, T., *Z. Phys. Chem.* **1**, 340 (1954).

[17] Zundel, G. and Metzger, H., *Z. Phys. Chem.* **58**, 225 (1968).

[18] Okumura, M.; Yeh, L. I.; Myers, J. D. and Lee, Y. T., *J. Phys. Chem.* **94**, 3416 (1990).

[19] Headrick, J. M.; Diken, E. G.; Walters, R. S.; Hammer, N. I.; Christie, R. A.; Cui, J.; Myshakin, E. M.; Duncan, M. A.; Johnson, M. A. and Jordan, K. D., *Science* **308**, 1765 (2005).

[20] Miyazaki, M.; Fujii, A.; Ebata, T. and Mikami, N., *Science* **304**, 1134 (2004).

[21] Schwarz, H. A., *J. Chem. Phys.* **67**, 5525 (1977).

[22] Newton, M. D., *J. Chem. Phys.* **67**, 5535 (1977).

[23] Meiboom, S., *J. Chem. Phys.* **34**, 375 (1961).

[24] Loewenstein, A. and Szoke, A., *J. Am. Chem. Soc.* **84**, 1151 (1962).

[25] Luz, Z. and Meiboom, S., *J. Am. Chem. Soc.* **86**, 4768 (1964).

[26] Knispel, R. R. and Pintar, M. M., *Chem. Phys. Lett.* **32**, 238 (1975).

[27] Graf, V.; Noack, F. and Bene, G. J., *J. Chem. Phys.* **72**, 861 (1980).

[28] Turner, D. L., *Mol. Phys.* **40**, 949 (1980).

[29] Lamb, W. J.; Brown, D. R. and Jonas, J., *J. Phys. Chem.* **85**, 3883 (1981).

[30] Halle, B. and Karlstrom, G., *J. Chem. Soc., Faraday Trans. II* **79**, 1031 (1983).

[31] Pfeifer, R. and Hertz, H. G., *Ber. Bunsen-Ges. Phys. Chem. Chem. Phys.* **94**, 1349 (1990).

[32] Woutersen, S. and Bakker, H. J., *Phys. Rev. Lett.* **96**, 138305 (2006).

[33] Car, R. and Parrinello, M., *Phys. Rev. Lett.* **55**, 2471 (1985).

[34] Tuckerman, M.; Laasonen, K.; Sprik, M. and Parinello, M., *J. Phys. Chem.* **99**, 5749 (1995).

[35] Billeter, S. R. and van Gunsteren, W. F., *J. Phys. Chem. A* **102**, 4669 (1998).

[36] Intharathep, P.; Tongraar, A. and Sagarik, K., *J. Comput. Chem.* **27**, 1723 (2006).

[37] Warshel, A. and Weiss, R. M., *J. Am. Chem. Soc.* **102**, 6218 (1980).

[38] Schmitt, U. W. and Voth, G. A., *J. Chem. Phys.* **111**, 9361 (1999).

[39] Lobaugh, J. and Voth, G. A., *J. Chem. Phys.* **104**, 2056 (1996).

[40] Sagnella, D. E. and Tuckerman, M. E., *J. Chem. Phys.* **108**, 2073 (1998).

[41] Vuilleumier, R. and Borgis, D., *J. Phys. Chem. B* **102**, 4261 (1998).

[42] Wu, Y. J.; Chen, H. N.; Wang, F.; Paesani, F. and Voth, G. A., *J. Phys. Chem. B* **112**, 467 (2008).

[43] Day, T. J. F.; Soudackov, A. V.; Cuma, M.; Schmitt, U. W. and Voth, G. A., *J. Chem. Phys.* **117**, 5839 (2002).

[44] Wang, F. and Voth, G. A., *J. Chem. Phys.* **122**, 144105 (2005).

[45] Chen, H.; Voth, G. A. and Agmon, N., *J. Phys. Chem. B* **114**, 333 (2010).

[46] Schmidt, R. G. and Brickmann, J., *Ber. Bunsen-Ges. Phys. Chem. Chem. Phys.* **101**, 1816 (1997).

[47] Lill, M. A. and Helms, V., *J. Chem. Phys.* **115**, 7993 (2001).

[48] Lill, M. A. and Helms, V., *Proc. Natl. Acad. Sci. U. S. A.* **99**, 2778 (2002).

[49] Lapid, H.; Agmon, N.; Petersen, M. K. and Voth, G. A., *J. Chem. Phys.* **122**, 014506 (2005).

[50] Vuilleumier, R. and Borgis, D., *J. Chem. Phys.* **111**, 4251 (1999).

[51] Izvekov, S. and Voth, G. A., *J. Chem. Phys.* **123**, 044505 (2005).

[52] Tuckerman, M. E.; Mundy, C. J. and Martyna, G. J., *Europhys. Lett.* **45**, 149 (1999).

[53] Walbran, S. and Kornyshev, A. A., *J. Chem. Phys.* **114**, 10039 (2001).

[54] Brancato, G. and Tuckerman, M. E., *J. Chem. Phys.* **122**, 224507 (2005).

[55] Brenner, D. W., *Phys. Rev. B* **42**, 9458 (1990).

[56] Tersoff, J., *Phys. Rev. Lett.* **56**, 632 (1986).

[57] Stoliarov, S. I.; Westmoreland, P. R.; Nyden, M. R. and Forney, G. P., *Polymer* **44**, 883 (2003).

[58] Stuart, S. J.; Tutein, A. B. and Harrison, J. A., *J. Chem. Phys.* **112**, 6472 (2000).

[59] Danielsson, J. and Meuwly, M., *J. Chem. Theory Comput.* **4**, 1083 (2008).

[60] Meuwly, M.; Becker, O. M.; Stote, R. and Karplus, M., *Biophys. Chem.* **98**, 183 (2002).

[61] Tully, J. C. and Preston, R. K., *J. Chem. Phys.* **55**, 562 (1971).

[62] Fornili, S. L.; Migliore, M. and Palazzo, M. A., *Chem. Phys. Lett.* **125**, 419 (1986).

[63] Sagnella, D. E. and Voth, G. A., *Biophys. J.* **70**, 2043 (1996).

[64] Kusaka, I.; Wang, Z. G. and Seinfeld, J. H., *J. Chem. Phys.* **108**, 6829 (1998).

[65] Urata, S.; Irisawa, J.; Takada, A.; Shinoda, W.; Tsuzuki, S. and Mikami, M., *J. Phys. Chem. B* **109**, 4269 (2005).

[66] Berendsen, H. J. C.; Postma, J. P. M.; Van Gunsteren, W. F. and Hermans, J., *Intermolecular Forces*, D. Reidel, Dordrecht (1981).

[67] Jorgensen, W. L.; J. Chandrasekhar, J.; Madura, J. D.; Impey, R. W. and Klein, M. L., *J. Chem. Phys.* **79**, 926 (1983).

[68] Berendsen, H. J. C.; Grigera, J. R. and Straatsma, T. P., *J. Phys. Chem.* **91**, 6269 (1987).

[69] Mahoney, M. W. and Jorgensen, W. L., *J. Chem. Phys.* **112**, 8910 (2000).

[70] Glick, R. E. and Tewari, K. C., *J. Chem. Phys.* **44**, 546 (1966).

[71] Rabideau, S. W. and Hecht, H. G., *J. Chem. Phys.* **47**, 544 (1967).

[72] Agmon, N., *Isr. J. Chem.* **39**, 493 (1999).

[73] Jiang, B.; Esai Selvan, M.; Keffer, D. J. and Edwards, B. J., *J. Chem. Phys. B* **113**, 13670 (2009).

[74] Esai Selvan, M.; Keffer, D. J.; Cui, S. and Paddison, S. J., *Mol. Simul.* **in press**.

[75] Huang, X. C.; Braams, B. J. and Bowman, J. M., *J. Chem. Phys.* **122**, 044308 (2005).

[76] Ojamäe, L.; Shavitt, I. and Singer, S. J., *J. Chem. Phys.* **109**, 5547 (1998).

[77] Hayes, R. L.; Paddison, S. J. and Tuckerman, M. E., *J. Phys. Chem. B* **113**, 16574 (2009).

[78] Paddison, S. J. and Elliott, J. A., *J. Phys. Chem. A* **109**, 7583 (2005).

[79] Paddison, S. J. and Elliott, J. A., *Phys. Chem. Chem. Phys.* **8**, 2193 (2006).

[80] McCall, D. W. and Douglass, D. C., *J. Phys. Chem.* **69**, 2001 (1965).

[81] Neria, E.; Fischer, S. and Karplus, M., *J. Chem. Phys.* **105**, 1902 (1996).

[82] Cui, S. T.; Liu, J.; Esai Selvan, M.; Keffer, D. J.; Edwards, B. J. and Steele, W. V., *J. Phys. Chem. B* **111**, 2208 (2007).

[83] Liu, J. W.; Esai Selvan, M.; Cui, S.; Edwards, B. J.; Keffer, D. J. and Steele, W. V., *J. Phys. Chem. C* **112**, 1985 (2008).

[84] Kell, G. S., *J. Chem. Eng. Data* **20**, 97 (1975).

[85] Hummer, G.; Soumpasis, D. M. and Neumann, M., *Mol. Phys.* **77**, 769 (1992).

[86] Nosé, S., *Mol. Phys.* **52**, 255 (1984).

[87] Nosé, S., *J. Chem. Phys.* **81**, 511 (1984).

[88] Hoover, W. G., *Phys. Rev. A* **31**, 1695 (1985).

[89] Tuckerman, M.; Berne, B. J. and Martyna, G. J., *J. Chem. Phys.* **97**, 1990 (1992).

[90] Press, W. H.; Vetterling, W. T.; Teukolsky, S. A. and Flannery, B. P., *Numerical Recipes in Fortran 77: The Art of Scientific Computing, 2nd ed.*, Cambridge University Press, Cambridge (1992).

[91] Petersen, M. K. and Voth, G. A., *J. Phys. Chem. B* **110**, 18594 (2006).

[92] Keffer, D.; Adhangale, P. and Edwards, B. J., *J. Non-Newtonian Fluid Mech.* **120**, 41 (2004).

[93] Simpson, J. H. and Carr, H. Y., *Phys. Rev.* **111**, 1201 (1958).

[94] Gillen, K. T.; Douglass, D. C. and Hoch, J. R., *J. Chem. Phys.* **57**, 5117 (1972).

[95] Agmon, N., *J. Chim. Phys.-Chim. Biol.* **93**, 1714 (1996).

[96] Markovitch, O. and Agmon, N., *J. Phys. Chem. A* **111**, 2253 (2007).

[97] Easteal, A. J.; Price, W. E. and Woolf, L. A., *J. Chem. Soc., Faraday Trans. I* **85**, 1091 (1989).

[98] Holz, M.; Heil, S. R. and Sacco, A., *Phys. Chem. Chem. Phys.* **2**, 4740 (2000).

[99] Mahoney, M. W. and Jorgensen, W. L., *J. Chem. Phys.* **114**, 363 (2001).

[100] Cornish, B. D. and Speedy, R. J., *J. Phys. Chem.* **88**, 1888 (1984).

[101] Robison, R. A. and Stokes, R. H., *Electrolyte Solutions*, Butterworths, London (1959).

[102] Markovitch, O. and Agmon, N., *J. Chem. Phys.* **129**, 084505 (2008).

[103] Yeh, I. C. and Hummer, G., *J. Phys. Chem. B* **108**, 15873 (2004).

[104] Bockris, J. O. M. and Reddy, A. K. N., *Modern Electrochemistry*, Plenum Press, New York (1970).

# Appendix B

## Probability of a Reaction by Trigger Satisfaction

In this appendix, probability of a reaction occurrence by trigger satisfaction is discussed. The conditional probability that each trigger was satisfied given that the previous trigger was satisfied is shown in Figure B.1. The first trigger, $r_{O^*O,Zundel,max}$ that checks whether the oxygen of the water is sufficiently close to the oxygen of the $H_3O^+$ ion is not shown, as it provides the conditional basis for the second trigger. The definition of each trigger is given in the manuscript. One can see that any single geometric trigger eliminates less than 40% of the $H_3O^+$ ions under consideration for reaction. However, the energetic trigger eliminates more than 99% of the $H_3O^+$ ions under consideration. One can also see that as the temperature increases, more molecules satisfy the energetic trigger while some of the geometric triggers display only weak temperature dependence. This is consistent with the idea that the temperature dependence of a chemical reaction is largely captured through the activation energy.

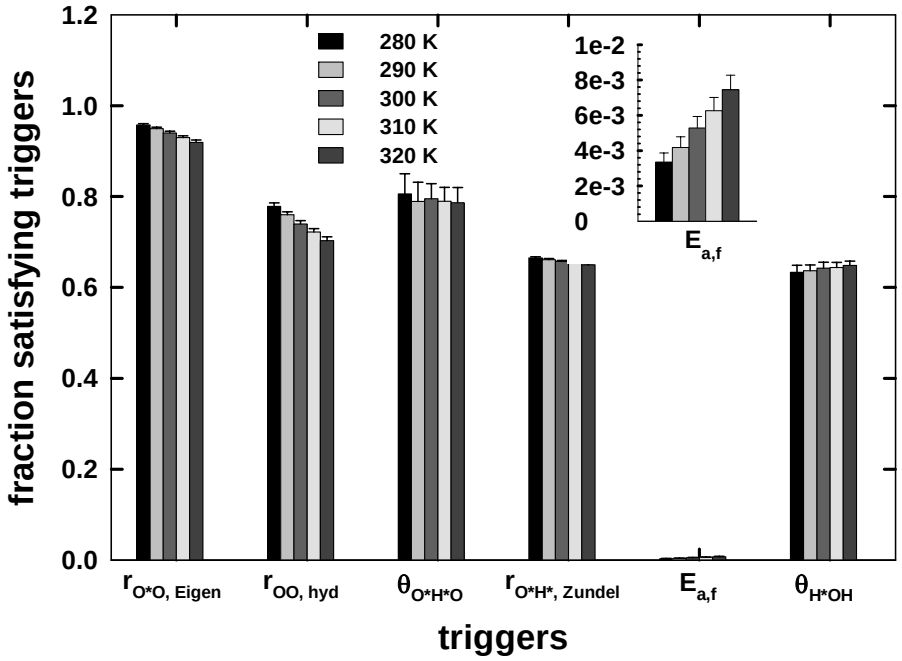


**Figure B.1.** Probability that a proton hopping reaction takes place as a function of triggers. Each probability is a conditional probability based on the satisfaction of all previous triggers, moving from left to right.

# Appendix C

## Relative $H_3O^+$ Ion-Water Mean Square Displacement

In this appendix, relative $H_3O^+$ ion-water mean square displacement is discussed. The relative $H_3O^+$ ion-water mean square displacement as a function of observation time is plotted in Figure C.2. This auto-correlation function is based on the difference between the current position ($\mathbf{r}_O(t)$) of the oxygen of the $H_3O^+$ ion carrying the excess proton at time=$t$ and the current position ($\mathbf{r}_{O^*}(t)$) of the oxygen that was part of the $H_3O^+$ ion carrying the excess proton at time=0.

$$r(t) = \left|\mathbf{r}_O(t) - \mathbf{r}_{O^*}(t)\right| \tag{C.1}$$

In the figure, the solid line represents the relative $H_3O^+$ ion-water correlation. The dashed line represents the total charge diffusivity. The dash-dot line represents the water diffusivity. In addition, the dash-dot-dot line is the sum of the absolute MSDs of water and charge, minus a constant of 38 $Å^2$. The dotted line is a fit to the three parameter equation,

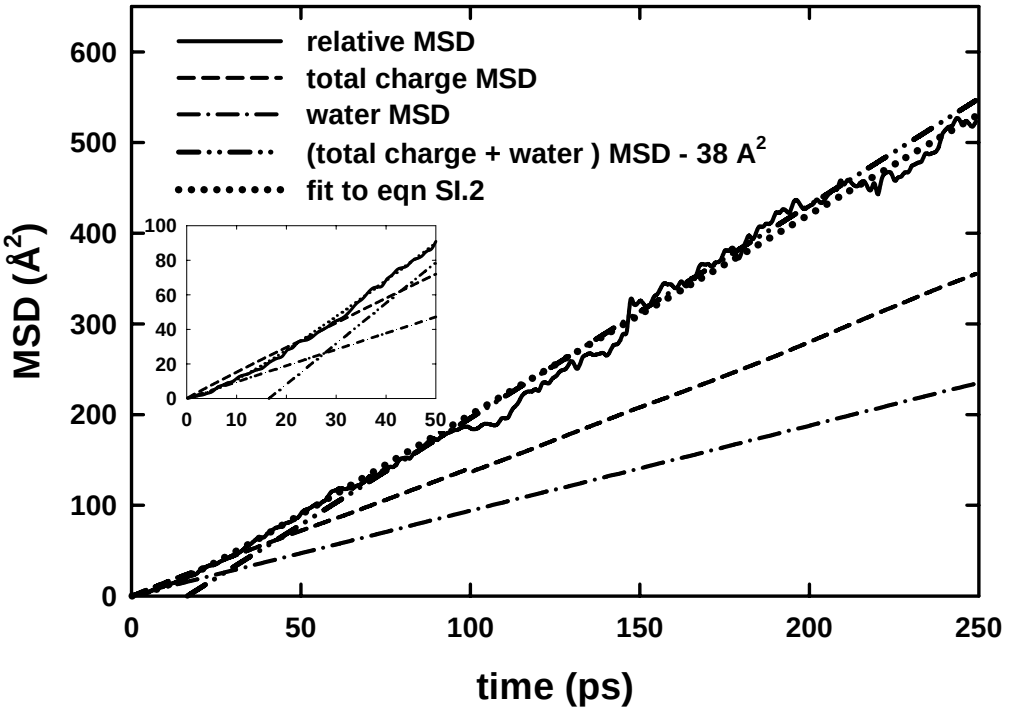


**Figure C.1.** The relative $H_3O^+$ ion-water correlation function. Additional description of each curve is given in the Appendix C discussion.

**Table C.1.** Comparison of transport properties between the RMD algorithm and the MS-EVB3 model

| System | $D_{\text{charge}}$ Å$^2$/ps | $D_{\text{water}}$ Å$^2$/ps | $D_{\text{charge}} + D_{\text{water}}$ Å$^2$/ps | $D_0$ Å$^2$/ps | $D_\infty$ Å$^2$/ps | $\tau$ ps |
|---|---|---|---|---|---|---|
| RMD system | 0.69 | 0.47 | 1.16 | 0.33 | 1.10 | 13.5 |
| MS-EVB3$^{\text{SI-1}}$ | 0.285 | 0.24 | 0.53 | 0.24 | 0.50 | 8 |

$D_{\text{charge}}$ is the total diffusivity of the charge. $D_{\text{water}}$ is the water diffusivity. $D_0$ is the short-time scale diffusivity, $D_\infty$ is the long-time scale diffusivity, and $\tau$ is the time in Eq. (C.2).

$$< [r(t) - r(0)]^2 > / 2 = D_\infty t + \tau(D_\infty - D_0)\left(e^{-t/\tau} - 1\right) \tag{C.2}$$

An analogous plot was presented by Chen *et al.* for the MS-EVB3 model [C-1] and our plot is qualitatively similar to their plot. They reported a shifting constant of 28 Å$^2$. Table C.1. compares the diffusivity values of the charge and water and the three parameters between the RMD system and the MS-EVB3 model

There is curvature in the short-time MSD behavior of the relative hydronium ion-water mean square displacement, Chen *et al.* [C-1] interpreted the time variation in $D(t)$ as arising from a distance-dependent $D(r)$, due to the fact that diffusion is impeded at short separations by stronger hydrogen-bonds in the hydronium ion inner solvation shells. As noted above, we reproduce qualitatively their results.

**Appendix C References**

[C-1] Chen, H.; Voth, G. A.; Agmon, N., *J. Phys. Chem. B* **114**, 333 (2010).

# Appendix D

## Tables and Figures

**Table 3.1.** Numerical values of the geometric and energetic triggers after parameterization[a]

| Triggers | $r_{O^*O,Zundel,max}$ (Å) | $r_{O^*H^*,eqlbm}$ (Å) | $\theta_{O^*H^*O}$ | $\theta_{H^*OH}$ | $r_{O^*O,Eigen,max}$ (Å) | $r_{OO,hydration,max}$ (Å) | $E_{a,f}$ (kcal/mol) |
|---|---|---|---|---|---|---|---|
| Prior Studies | 2.3 – 2.75[b] | 0.80 – 1.30[b] | 173.73[c] | 115.8 – 118.2[c] | 2.35 – 2.7[b] | 2.40 – 3.30[d] | 2.4[e] |
| Classical MD | 2.35 – 2.85[f] | 0.957[g] | - | ≈ 104[h] | 2.35 – 2.85[f] | 2.50 – 3.40[f] | ≥ -26.05[i] |
| RMD parameters | 2.35 – 2.75 | ≥ 0.965 | ≥ 146.0 | 65 – 143 | 2.35 – 2.93 | 2.50 – 3.29 | ≥ -23.39 |

[a] The graphical representation of the triggers is given in Figure 3.1. [b] The distribution of the first peak from the RDF of $O(H_3O^+)$–$O(H_2O)$, $H(H_3O^+)$–$O(H_3O^+)$ in Zundel cation and $O(H_3O^+)$–$O(H_2O)$ in Eigen cation from Ref. 54. [c] Bond angles of $\angle O_1H^+O_2$ and $\angle H_3O_2H^+$ from optimized isolated $H_5O_2^+$ structure from Ref. 75. [d] The distribution of the first peak from the RDF of $O(H_2O)$–$O(H_2O)$ in quantum simulations of water from Stern HA, 2001. [e] Activation energy from Ref. 25. [f] The distribution of the first peak from the RDF of MD simulations where the system of hydronium ions and water molecules are treated classically. [g] Equilibrium bond distance of OH in $H_3O^+$ TIP3P model. [h] Equilibrium bond angle in TIP3P model. [i] Figure 3.3.

**Table 3.2.** Occurrence of the first peak in the RDF between atoms *i* and *j* in a classical MD system[a]

| $N_{\text{pairs}}$ | $i - j$ | $r_{ij}^{\text{target}}$ (Å) |
|---|---|---|
| 1 | $O_3 - O_2$ | 2.80 |
| 2 | $O_4 - O_2$ | 2.80 |
| 3 | $O_5 - O_1$ | 2.55 |
| 4 | $O_6 - O_1$ | 2.55 |
| 5 | $O_1 - O_2$ | 2.55 |
| 6 | $O_3 - H_1$ | 1.85 |
| 7 | $O_4 - H_2$ | 1.85 |
| 8 | $O_5 - H_3$ | 1.60 |
| 9 | $O_6 - H_4$ | 1.60 |
| 10 | $O_3 - O_1$ | 4.90 |
| 11 | $O_4 - O_1$ | 4.90 |
| 12 | $H_5 - O_2$ | 1.60 |

[a] Values correspond to Eq. (10) and labels appear in Figure 3.4.

**Table 3.3.** Activation energy and rate constant prefactor[a]

| System | $k_o$ ($10^{11}$ l/(mol.s)) | $E_{a,f}$ (kcal/mol) |
|---|---|---|
| Experimental [b] | 5.99 | 2.40 |
| Simulation | 14.20 | 2.91 |

[a] Activation energy, $E_{a,f}$ and rate constant prefactor, $k_o$ are obtained from an Arrhenius plot using the rate constants in Figure 3.5. [b] Ref. 25.

**Table 3.4.** Comparison of the diffusion coefficients of $H_2O$ and $H_3O^+$ in the nonreactive system with pure water diffusivities from experiment and simulation

| T | Pure water system | | Nonreactive system | |
|---|---|---|---|---|
| (K) | Experimental[b] | Simulation | $H_2O$ | $H_3O^+$ |
| 280 | 1.24 | 3.40 ± 0.46 | 3.04 ± 0.20 | 1.46 ± 0.22 |
| 290 | 1.70 | 3.69 ± 0.21 (2.99)[c] | 3.59 ± 0.28 | 2.18 ± 0.30 |
| 300 | 2.26 | 4.62 ± 0.26 (3.60)[c] | 4.24 ± 0.31 | 2.30 ± 0.16 |
| 310 | 2.92 | 4.92 ± 0.17 | 4.97 ± 0.34 | 2.69 ± 0.32 |
| 320 | 3.69 | 5.67 ± 0.42 (5.07)[c] | 5.65 ± 0.35 | 3.49 ± 0.23 |

[a] All Diffusivities are in $10^{-5}$ $cm^2/s$. [b] Refs. 97 and 98. [c] Values from Table I in Ref. 102.

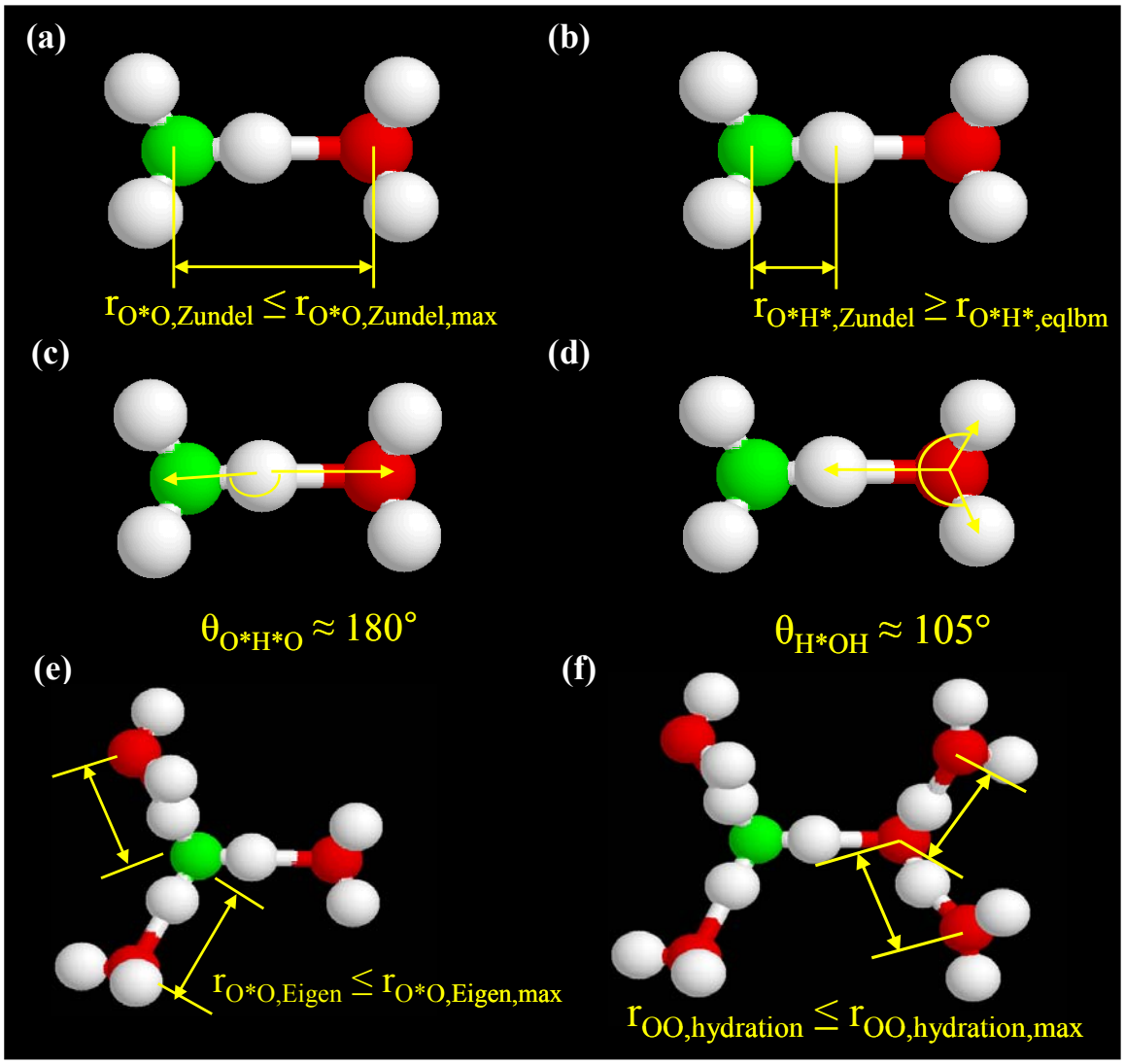


**Figure 3.1.** Description of the six geometric triggers identified for the structural diffusion of a proton: **(a)** O*–O separation must form a Zundel ion; **(b)** O*–H* separation must exceed the equilibrium bond distance; **(c)** $\angle O^*H^*O$ is nearly linear in the Zundel ion; (d) lone pair of electrons in the water should point towards the proton; **(e)** initial $H_3O^+$ forms an Eigen ion; **(f)** an Eigen ion is formed around final $H_3O^+$. These six geometric triggers must be satisfied along with the energetic trigger for the reaction to take place. O of $H_3O^+$, green; O of $H_2O$, red; H, white.

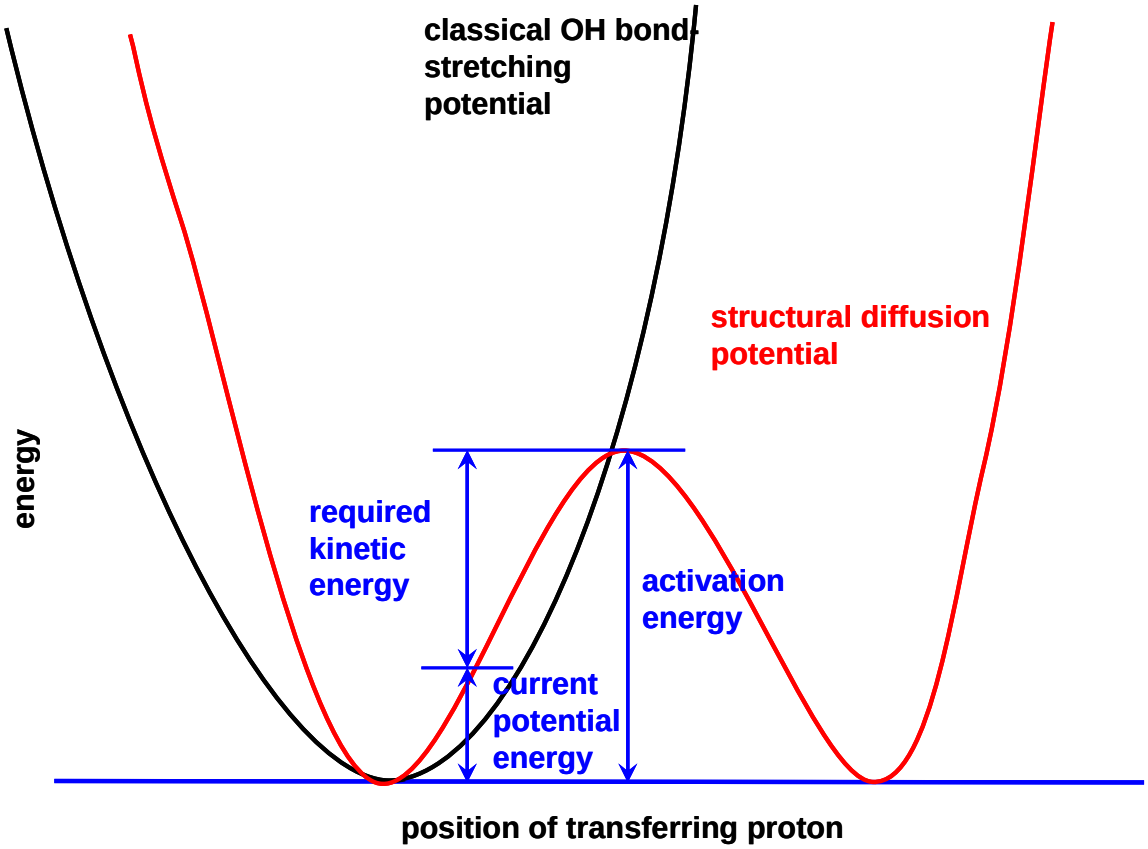


**Figure 3.2.** Description of the energetic trigger for the structural diffusion of a proton. The proton getting transferred will have the potential energy along the red curve while the black curve represents the classical definition. The sum of potential and kinetic energies of the proton should be higher than the activation energy to go from one well to the other side.

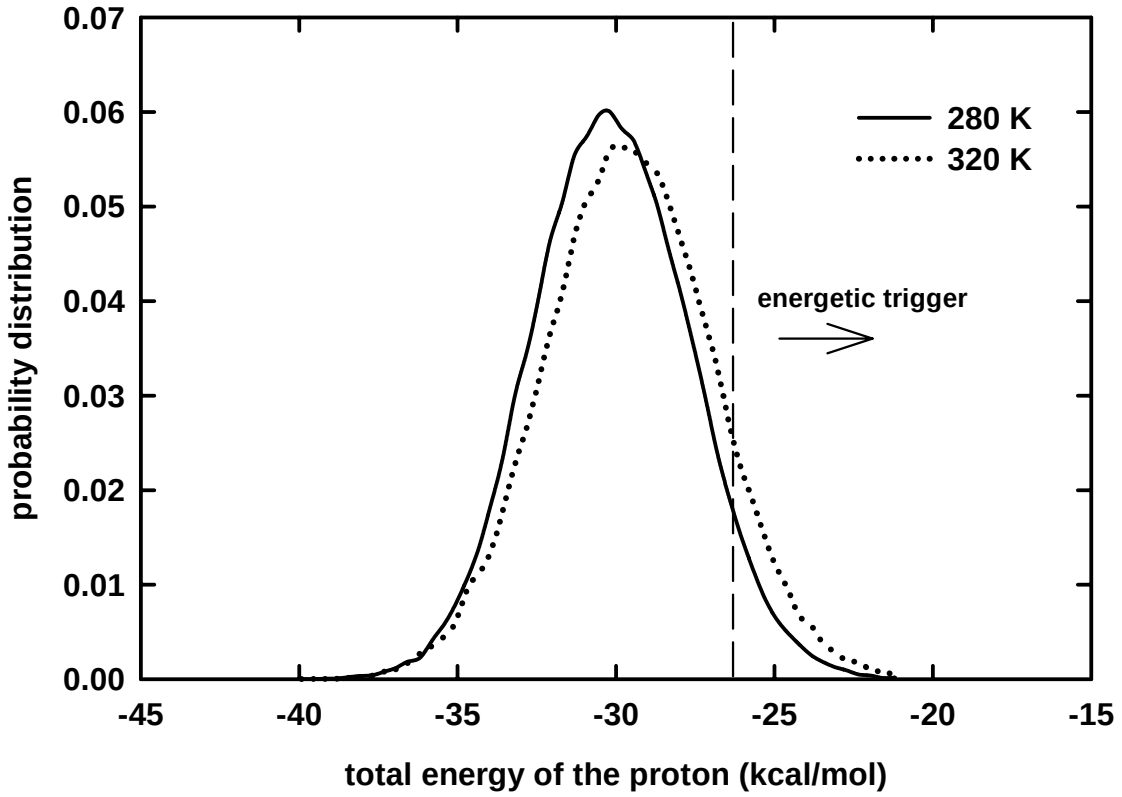


**Figure 3.3.** Energy distribution (inter + intra + kinetic energy) of the proton to be transferred in a $H_3O^+$ ion satisfying six geometric triggers at 280 K (bold line) and 320 K (dotted line).

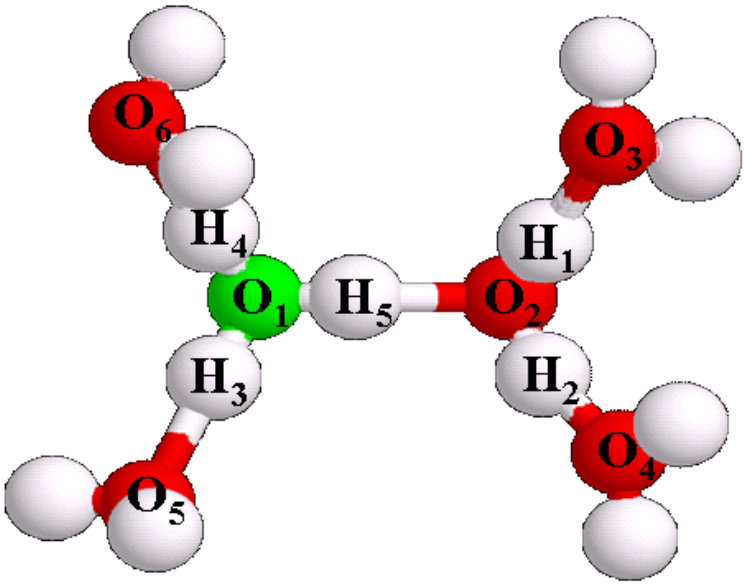


**Figure 3.4.** Schematic representation of $N_{\text{pairs}}$ in Eq. (10) and labels of the atoms designated as *i* and *j* in Table 3.2. O of $H_3O^+$, green; O of $H_2O$, red; H, white.

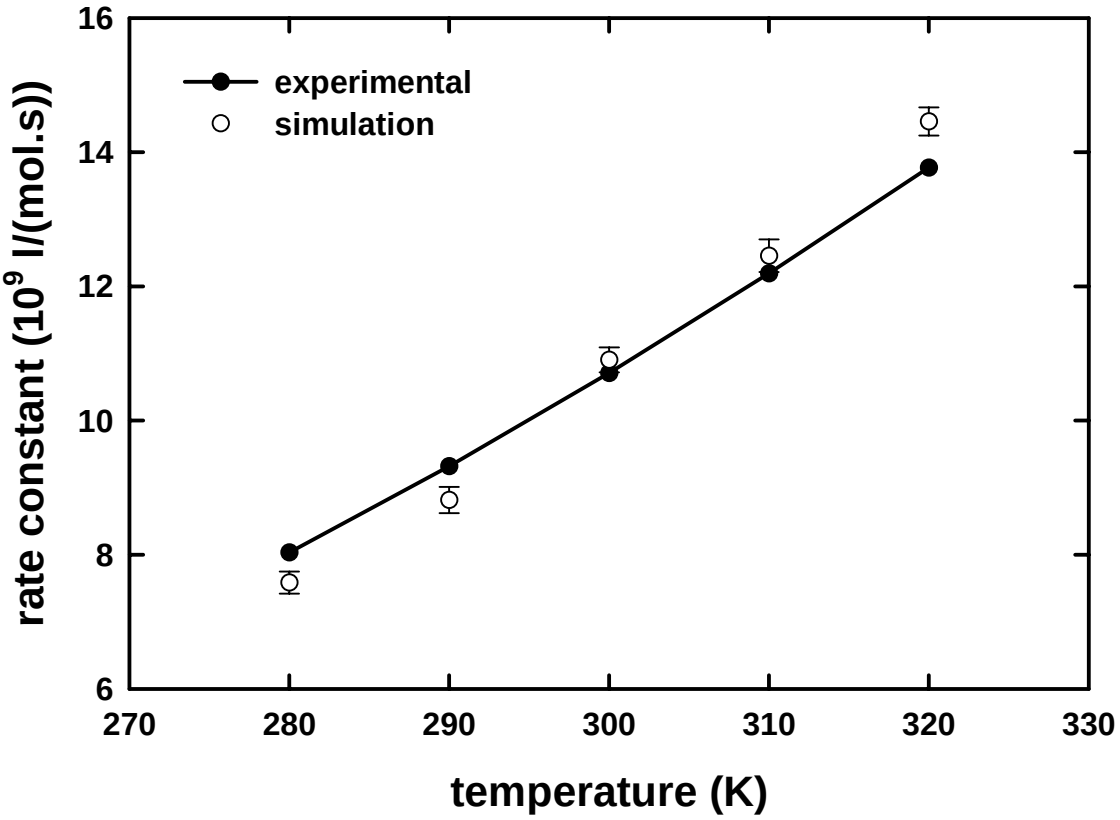


**Figure 3.5.** Rate constants, *k*, of the reaction in simulation (circle) calculated using Eq. (11) compared to the experimental (bold line) values (Ref. 25) as a function of temperature.

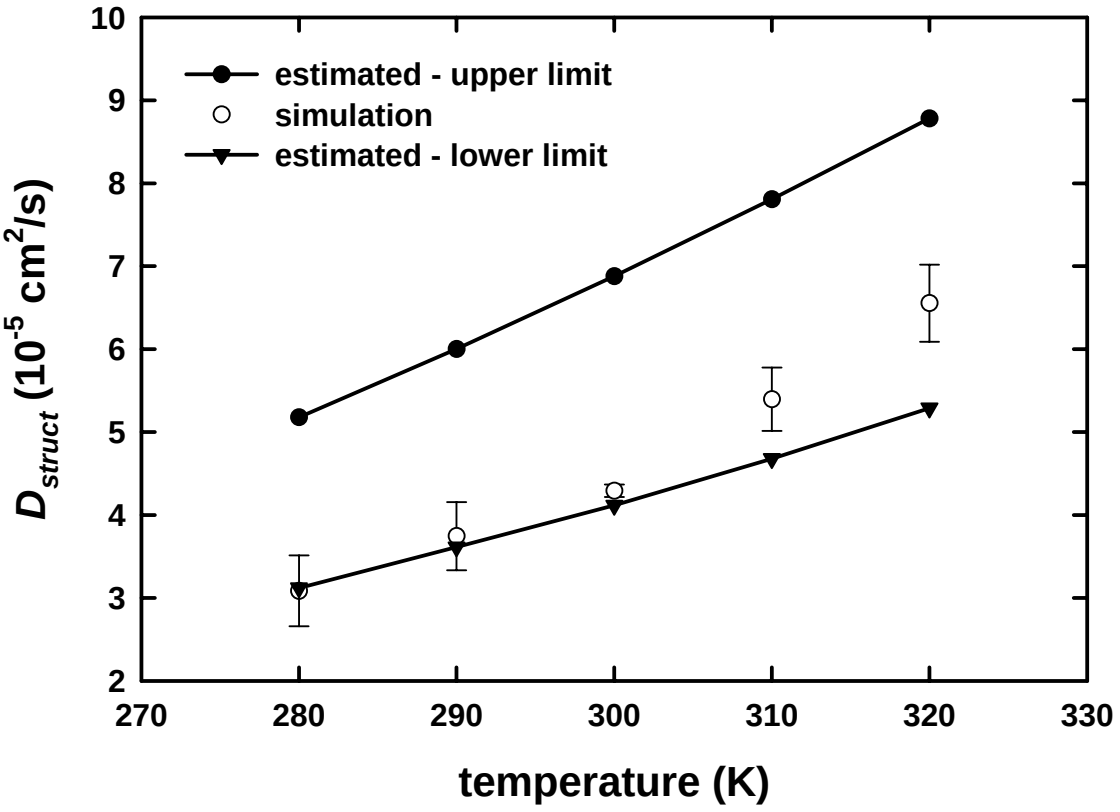


**Figure 3.6.** Structural diffusion coefficients obtained from simulation (circle) with the estimated (bold line) upper and lower limits of the structural component of the charge diffusivity as references (from Eq. (14)).

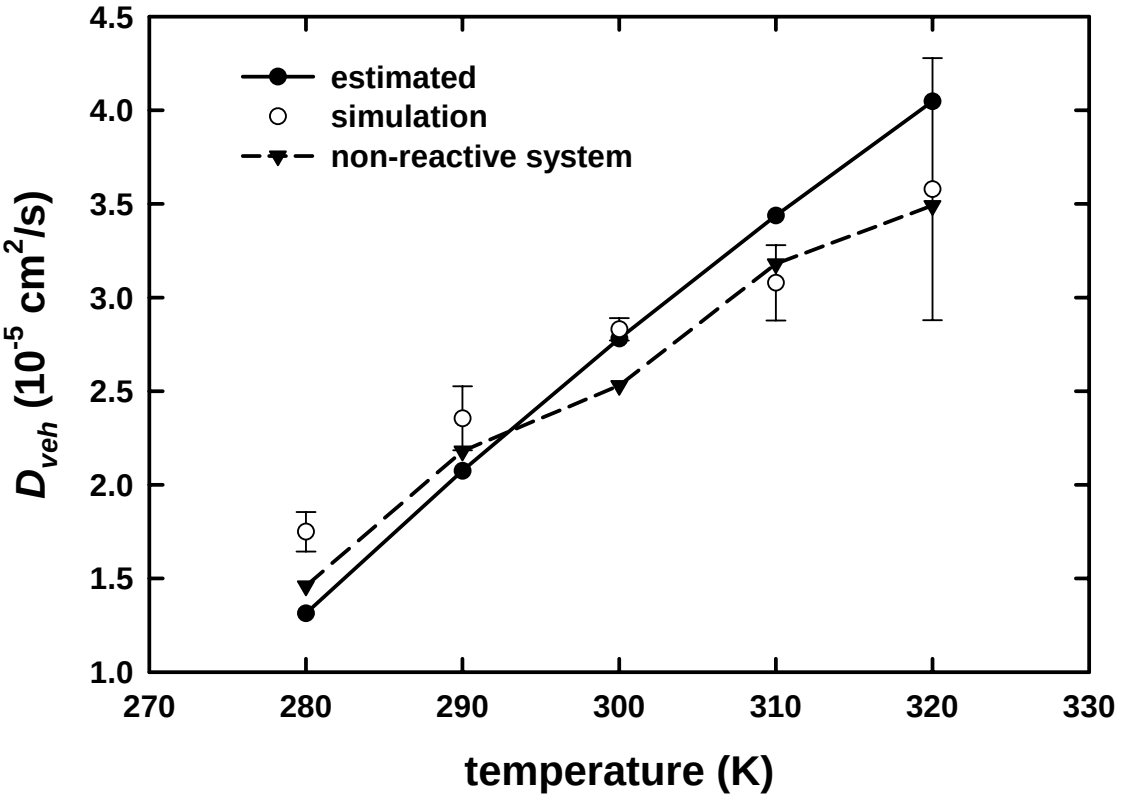


**Figure 3.7.** Vehicular component of the proton diffusivity, $D_{\text{veh}}$, which measures the movement of the centre of mass of the hydronium ion is given as a function of temperature: bold line, estimated; dashed line, non-reactive system; circle, reactive system.

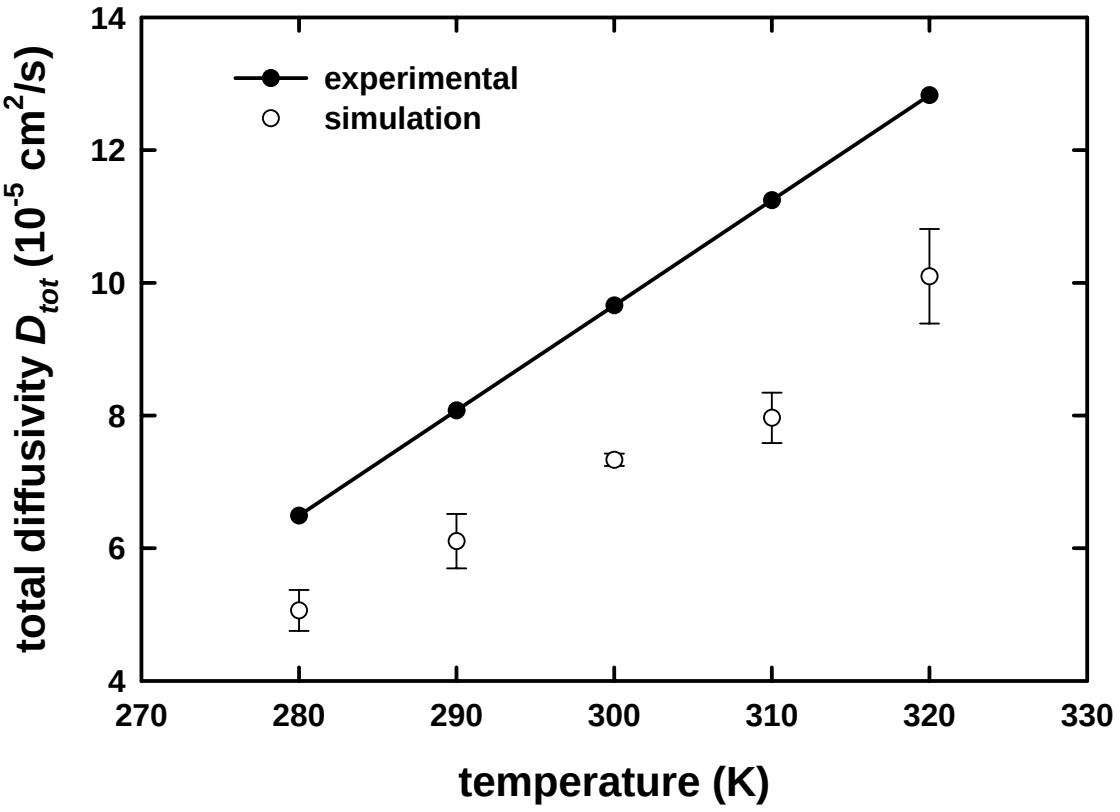


**Figure 3.8.** Total diffusion of the charge from simulation (circle) is compared with the experimental (bold line) value (Refs. 100 and 101) as a function of temperature.

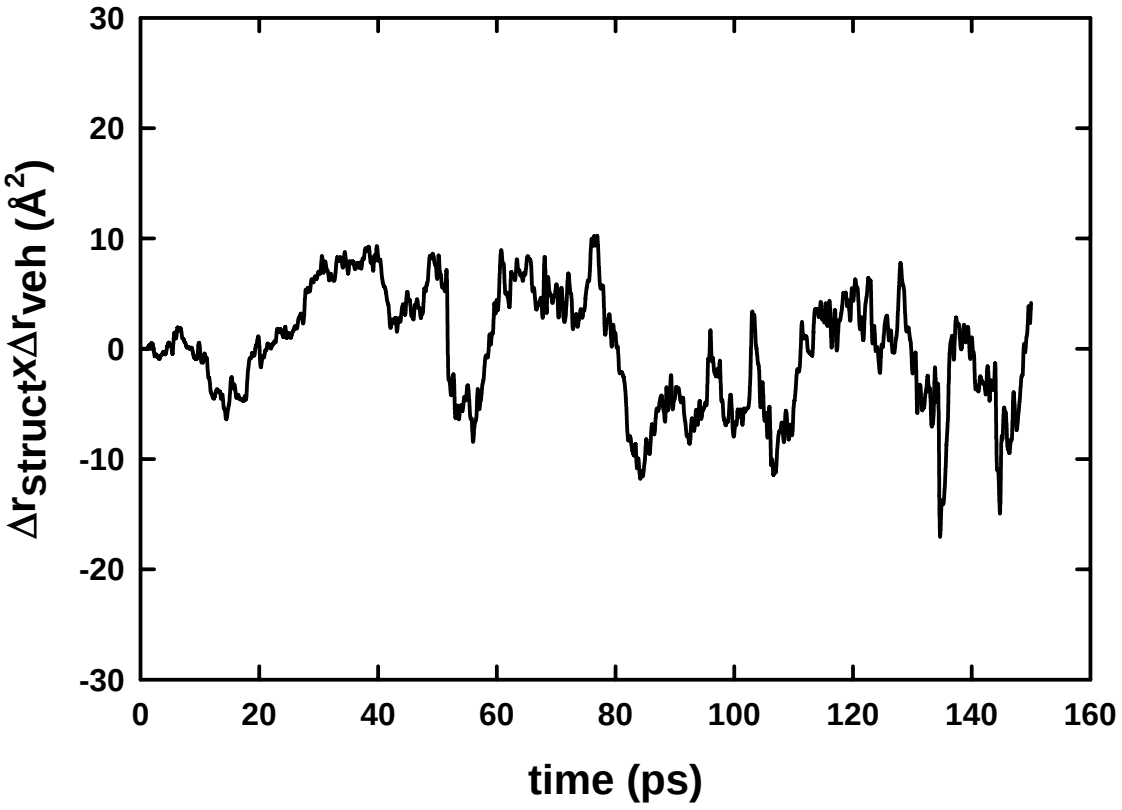


**Figure 3.9.** Correlation term ($\Delta r_{struct} \times \Delta r_{veh}$) calculated from structural and vehicular displacements of the charge as a function of time at 320 K. The term being close to zero implies both components of the total charge diffusion are uncorrelated.

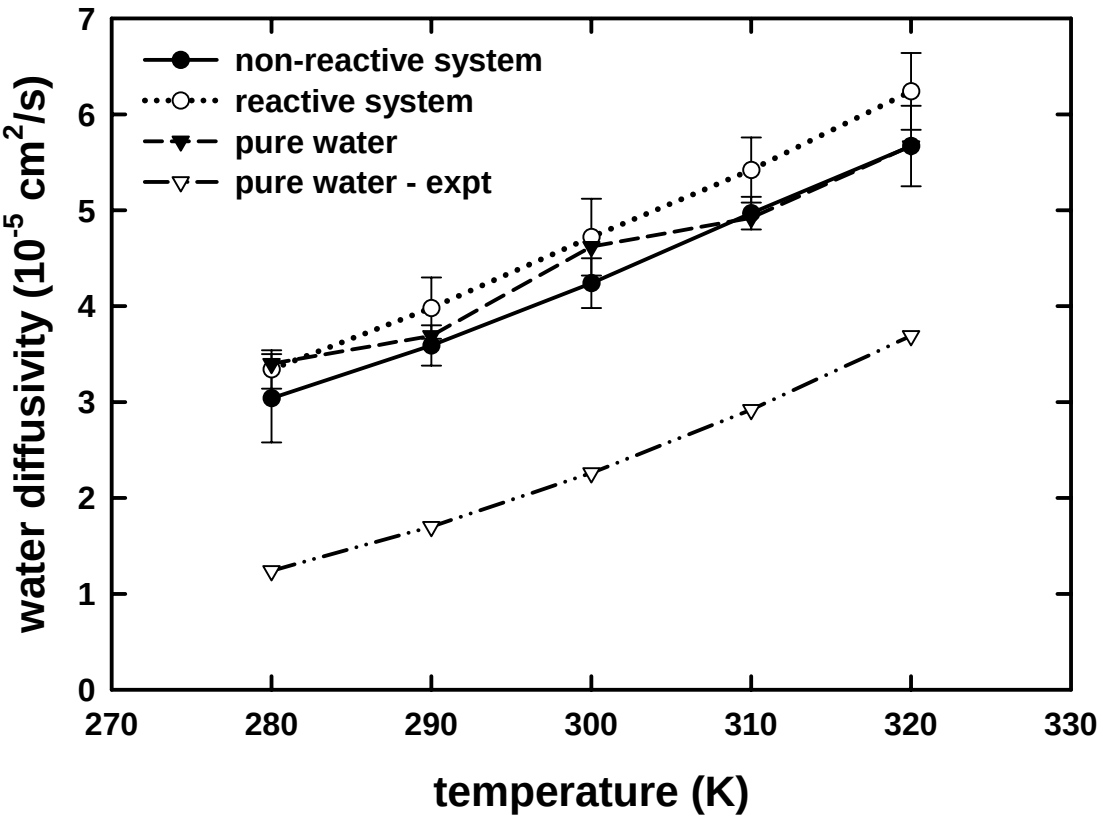


**Figure 3.10.** Water diffusivity in various systems—nonreactive (solid circle) and reactive system (circle) are compared to that of pure water simulation (solid triangle) using TIP3P model. Experimental diffusion coefficients of water (triangle) are from Refs. 97 and 98.

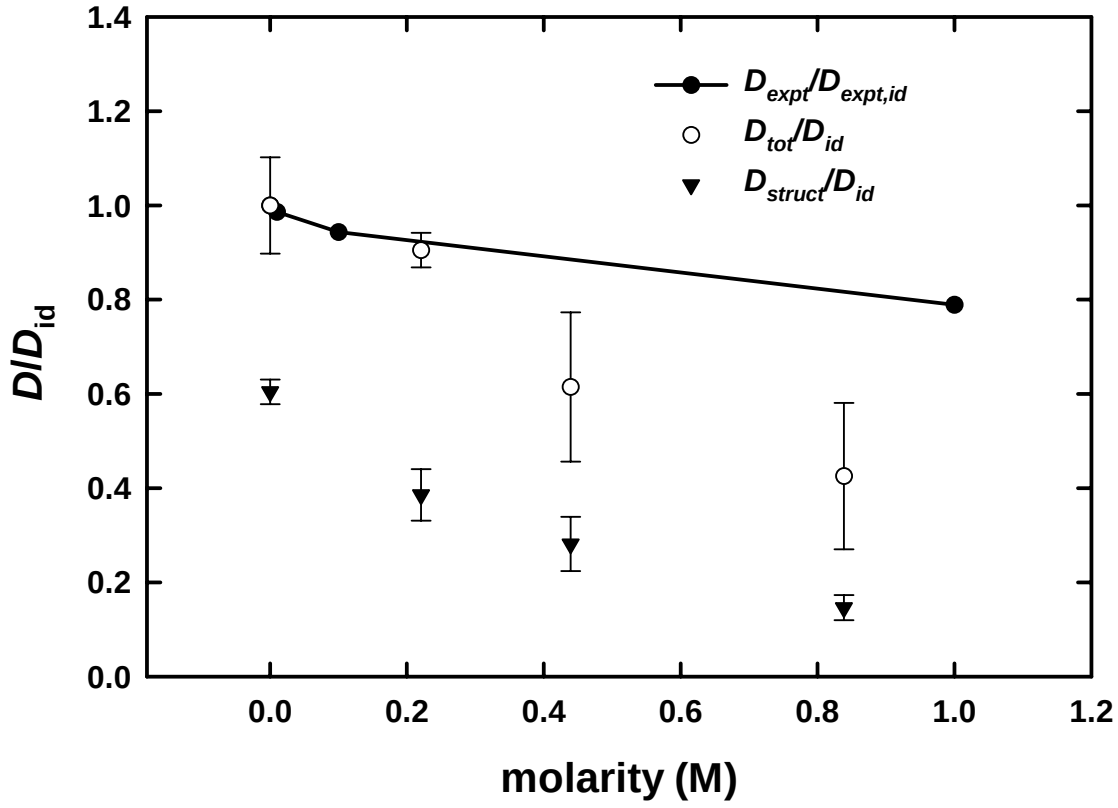


**Figure 3.11.** Total and structural component of the charge diffusivity as a function of concentration at 300 K. The diffusivities are represented as a ratio to the total charge diffusivity at infinite dilution ($D_{id}$)—Diffusivity calculated from experimental conductivity (solid circle), total diffusivity, $D_{tot}/D_{id}$ (circle), and structural component of the charge diffusivity, $D_{struct}/D_{id}$ (solid triangle).

# CHAPTER 4

# Proton Transport in Water Confined in Carbon Nanotubes: A Reactive Molecular Dynamics Study

This chapter is a slightly revised version of a paper by the same title published in the *Molecular Simulation* in 2010 by Myvizhi Esai Selvan, David J. Keffer, Shengting Cui, and Stephen J. Paddison:

Esai Selvan, M.; Keffer, D. J.; Cui, S. T.; and Paddison, S. J., "Proton transport in water confined in carbon nanotubes: A reactive molecular dynamics study", *Mol. Sim.* **36**, 568 (2010).

The use of "we" in this part refers to the co-authors and the author of this dissertation. My primary contributions to this paper include (1) all of the simulation work (2) analysis of data, and (3) most of the writing



**Abstract**

The effects on the structural and transport properties of a proton in water confined in carbon nanotubes of radii ranging from 5.42 to 10.85 Å were studied by employing a recently devised reactive molecular dynamics (RMD) scheme. The formation of distinct layers was observed in the computed radial density profile of water. Affinity of hydronium ions towards the tube–water interface and its preferential orientation with the oxygen atom protruding towards the wall was observed. The axial water diffusivity was observed to decrease with increasing confinement of water. Analysis of the axial charge diffusivity and its two components (structural and vehicular) was also performed. Confinement was found to have a more significant effect on structural diffusion than on vehicular diffusion. The axial vehicular component of the charge diffusivity in the nanotube of radius 10.85 Å was found to be equal to the value computed in bulk water while structural component was 12% of the value observed in bulk water, which resulted in a total charge diffusivity of 42% of the diffusion in bulk water. The confined geometry affects the system energetically and perturbs the solvation structure around the proton from that found in bulk water. The RMD algorithm, which defines the occurrence of a proton transfer reaction based on the satisfaction of a set of triggers, identified the energetic factor to be greatly responsible for the decreased structural diffusion of a proton.

## 4.1 INTRODUCTION

Proton transport is a key process in many chemical (acid–base solutions), biological (proteins and enzymes) and electrochemical [proton exchange membranes (PEM)] systems and hence a fundamental understanding of this process will benefit a wide range of applications. One of the potential applications of proton transport includes the energy conversion in PEM fuel cells. Many PEM fuel cells use perfluorinated sulfonic acid polymers (e.g Nafion, Flemion, Aciplex) as electrolytes, which have a perfluorinated backbone and pendant side chains containing sulfonic acid ($SO_3H$) groups. Hydration of the materials leads to a spontaneous segregation into hydrophobic (perfluorinated backbone) and hydrophilic regions (water and charged side groups) whose characteristic dimensions are of the order of nanometers. It is through the hydrophilic domain networks that the proton is transported. Therefore, understanding the relationship between proton transport and the hydrated morphology, which is governed by the polymer structure [1,2], is important in the development of economically viable PEM fuel cells.

There is significant understanding of the molecular-level mechanisms of proton transport in bulk water. The proton is transported via both structural diffusion [3,4] and mass diffusion as hydronium ions (vehicular diffusion). Structural diffusion involves the hopping of protons from one water molecule to another via structural defects [5]. The hopping mechanism is responsible for the high mobility of protons compared to other cations of similar size and charge in aqueous media [6]. Structural diffusion of the proton in aqueous media occurs by the continual interconversion of two predominant structures of Zundel [7] ($H_5O_2^+$) and Eigen [8] ($H_9O_4^+$) cations with the cleavage and formation of the hydrogen bonds in the second solvation shell [3,9].

The aqueous domains within PEMs differ from bulk water in two important ways. First, the proton is in a highly acidic environment and, second, the proton is in a confined fluid. The effects of confining the proton transport to very small aqueous regions are not completely understood. However, both experimental and modeling studies have revealed that the water in PEMs exhibits a decreased polarity and rate of relaxation and an increase in the degree of the spatial and orientational order when compared to bulk water [10-13]. We have examined systems in which the acidity and confinement can be independently varied to better understand how these

two factors, acidity and confinement, impact proton mobility. Previously, we investigated the effects of acidity on proton transport in aqueous solutions of HCl [14]. In the present study, we examine only the effect of confinement on proton transport in dilute acidic solutions in carbon nanotubes (CNTs). This ability to distinguish between the impact of acidity and confinement on proton transport may help to understand the cumulative behavior of proton transport in PEMs, where both acidity and confinement are present.

Currently, there is evidence from theory and simulation that both proton transport mechanisms are active in PEMs [15-19]. However, the extent to which these two mechanisms function in an environment with high local density of acidic groups is unclear [20,21]. Recent investigations employing *ab initio* molecular dynamics (AIMD) simulations of proton transport in the mono-, di-, and tetra-hydrates of trifluoromethanesulfonic acid substantiate the evidence that structural diffusion occurs in systems with very high densities of $SO_3H$ and encapsulated water [22,23].

Various modeling techniques such as Car–Parinello AIMD [4,24], mixed quantum and classical mechanics techniques [25,26] (QM/MM), various empirical valence bond (EVB) schemes [27-30], a mixed MD/MC algorithm [31], and the Q-HOP MD method [32] have been devised to investigate proton transport. We have chosen to utilize a reactive molecular dynamics (RMD) algorithm, which has been applied previously to study proton transport in bulk water [14] as well as the thermal decomposition of perfluorodimethyl ether [33]. Using the RMD algorithm, the effect of acidic environment on the mechanisms of proton transport has already been investigated by the implementation of the algorithm in aqueous HCl systems of concentrations ranging from 0.22 – 0.83 M [14]. One advantage of the RMD algorithm is that, although it was parameterized in bulk water, it can be applied to bulk HCl solutions or to transport in CNTs without reparameterization, because, at least to the coarse-grained level of description contained within the algorithm, it is able to directly account for the impact of the local environment on the reaction rate.

The transport properties of protons through water confined in carbon nanotubes (CNTs) of various diameters have been investigated earlier by AIMD simulations [34], classical MD simulations using potentials derived from *ab initio* calculations [35], and EVB models [36,37]. When the channels are very narrow (i.e., a (6,6) CNT of radius 4.07 Å), water wires are formed

[34,37]. Proton diffusion through these well aligned (defect-free) quasi-1D hydrogen bonded water chains exceeds that in bulk water by a factor of 40 [37]. The influence of the electrostatic forces due to charge or polarity of the CNT leads to the formation of hydrogen-bonding defects in the water wire such as the L-defects and D-defects which can drastically hinder the proton transfer mechanism [37]. A proton encapsulated within a water wire in a CNT is found to be highly stabilized but in the presence of an electric field, rapid diffusion is observed [34]. Once the CNT radius is large enough to have a 3D hydrogen bonded water network, the proton diffusivity is sensitive to the channel radius and increases with the decrease in confinement [36].

In this work, the RMD algorithm has been applied to simulate proton transport through water confined in CNTs of radii from 5.42 – 10.85 Å to study the effect of confinement on the individual contribution of the component of the charge diffusion and to understand the probable reasons that can affect the structural diffusion of proton under confinement. CNTs play a pivotal role in a wide range of applications from membrane separations to drug delivery and hence understanding the effect of the confined CNT geometries on fluid transport properties has independent merit [38].

The paper is organized as follows: the methodology including a brief description of the RMD algorithm and the details of the simulations are described in Sec. 4.2, the results and discussion are presented in Sec. 4.3, and the conclusions are summarized in Sec. 4.4.

## 4.2 METHOD

The structural diffusion of a proton is modeled with the RMD algorithm, whose details are presented in our earlier work [14,33]. A short description of the method is given here. The proton transfer process can be written as the following chemical reaction:

$$H_3O^+ + H_2O \xleftarrow{nH_2O} H_2O + H_3O^+ \quad (1)$$

Chemical reactions occur when the reactant molecules are suitably oriented and have sufficient energy to overcome the activation barrier for the formation of the products. The RMD algorithm coarse grains the chemical reaction via three steps: (i) satisfaction of a set of geometric and energetic triggers, (ii) instantaneous reaction, and (iii) local equilibration. We perform a classical MD time step in the RMD algorithm. At the end of each MD time step the three steps of the RMD algorithm are implemented. The first step checks whether the reactants ($H_2O$ and $H_3O^+$)

satisfy a set of six geometric triggers and one energetic trigger. The functional form of these triggers indicates that the reactant is following a trajectory leading to the transition state, as determined by quantum mechanical calculations. In other words, satisfying a set of triggers ensures that one has the correct starting configuration for the reaction in Eq. (1) to take place. For this specific reaction, the six geometric triggers dictate (1) a maximum separation between the O of the $H_3O^+$ ion and the O of the $H_2O$ molecule participating in the reaction, $r_{\mathrm{OO,Zundel,max}}$, (2) a minimum separation between the proton to be transferred and the O of the $H_3O^+$ ion, $r_{\mathrm{OH,Equilib}}$, (3) colinearity of the O of the $H_3O^+$ ion, the O of the $H_2O$ molecule and the proton to be transferred, $\theta_{\mathrm{OHO}}$, (4) proper H–O–H bond angles between the proton and H on the water molecules, in accord with $sp^3$ bond hybridization, $\theta_{\mathrm{HOH}}$, (5) hydrogen bonding of the two non-transferring H on the $H_3O^+$ ion with O of solvating water molecules, $r_{\mathrm{OO,Eigen,max}}$, and (6) hydrogen bonding of the two H atoms on the $H_2O$ molecule with O of other water molecules, $r_{\mathrm{OO,Hydration,max}}$. The energetic trigger, $E_{\mathrm{a,f}}$, ensures that the total energy of the proton to transferred composed of the kinetic energy projected along the reaction axis and all components of potential energy (intramolecular interactions and intermolecular—both Lennard-Jones (LJ) and electrostatic interactions) is sufficient to overcome the activation barrier for reaction. The numerical values of these triggers are tuned to the experimental reaction rate as a function of temperature to yield the correct activation energy and rate constant for bulk water. The schematic representation of the six geometric triggers is shown in Figure 4.1 and the trigger values are given in parenthesis. The first step of a reaction in the RMD algorithm is therefore the satisfaction of a set of triggers for a favorable starting configuration for the reaction to take place.

The RMD algorithm includes fewer details than the quantum mechanical studies and many more details than the macroscopic modeling. The RMD triggers represent a necessary and sufficient condition for reaction to take place and predict well the charge diffusivity in bulk water, but they may not be the only set of triggers capable of doing so. It is possible that an alternative set of triggers including, for example, coordination number of water molecules in the first solvation shell might also suffice, but that alternative has not been explored here. There are certainly more detailed characteristics of the proton hopping process that do not appear in the

more coarse-grained RMD description. For example, recent studies indicate that the cleavage of an acceptor-type hydrogen bond of a water molecule in the first solvation shell (forming the Zundel complex) is the rate limiting step associated with partner exchange and the cleavage of a donor type hydrogen bonds of the other two water molecules (in the first solvation shell) not involved in the reaction is likely to be associated with the actual proton transfer event [9]. The purpose of the RMD algorithm, like any coarse-grained procedure, is to capture the basic behavior of the system with as few degrees of freedom as possible. Admittedly, in this procedure, the full quantum mechanical description of proton transport is not retained.

The second step of the RMD algorithm is the instantaneous reaction. Once the complete set of triggers has been satisfied by a given reactant, the RMD algorithm coarse grains the reaction path and the proton gets transferred instantaneously. The reaction involves exchanging the identities of the reactants, where the $H_3O^+$ that previously contained the proton to be transferred is now $H_2O$ and the $H_2O$ that received the proton is now a $H_3O^+$ ion. The reaction takes place with no time elapsed in the MD simulation.

The third and final step of the RMD algorithm is the local equilibration. When a reaction takes place, structure and energy of the system is disturbed. The heat of reaction is zero for structural diffusion of proton. Therefore, the objective of the local equilibration is to ensure that one has the correct ending configuration of the product in Eq. (1) and satisfy the target heat of reaction. The re-establishment of reasonable hydrogen bonding network and energy of the system is achieved by relaxing the hydrating water molecules of the reactants with an objective function that has a weighted combination of both energetic and structural term. Once structural diffusion is implemented by the RMD algorithm, the MD simulation continues on to the next time step.

The algorithm includes several proven beneficial effects as follows: (1) usage of computationally efficient classical MD simulation, (2) reduction in the development time required to parameterize the reactive algorithm, relative to reactive potentials, due to the decrease in the degrees of freedom, and (3) extension of the methodology from one environment (bulk water) to another environment (aqueous HCl system or fluids confined in CNTs).

The accurate determination of the density of fluids under confinement is difficult since the inaccessible volume due to tube – wall interaction and void fraction due to the organized

structure varies based on the choice of radius. There are various methods of determining the density of water [39]. One way is to immerse a nanotube segment into a large water bath where the water molecules are free to enter and exit the nanotube, so that one can obtain the natural density [40]. Another way is to perform simulations with fixed number of water molecules inside the nanotube based on the density of water (typically 1 g/cc) [36,41,42]. Here, we follow the latter and simpler method where the number of molecules needed in the system is fixed and the length of the CNT is determined from the bulk water density and accessible volume. The effective accessible radius is defined as the radius beyond which no water molecules exist due to the wall repulsion. The nanotubes are represented by a smooth external potential instead of modeling the walls atomistically with site-to-site interaction. Fluid – tube interactions have been modeled with a LJ potential integrated over the semi-infinite volume of the wall in cylindrical coordinates, as derived by Peterson *et al*. [43]. The fluid particle at a radial position, r, from the tube axis interacts with the tube wall of radius, *R*, using the potential, $V_{\mathrm{ft}}$,

$$V_{\mathrm{ft}}(r,R) = \pi\varepsilon_{\mathrm{ft}}\rho_{\mathrm{t}}\left[\frac{7\sigma_{ft}^{12}}{32}K_9(r,R) - \sigma_{\mathrm{ft}}^{6}K_3(r,R)\right] \tag{2}$$

where $K_m(r,R)$ is defined as

$$K_m(r,R) = R^{-m}\int_0^{\pi} d\Theta\left[-\eta\cos\Theta + (1-\eta^2\sin^2\Theta)^{1/2}\right]^{-m} \tag{3}$$

and $\eta = r/R$. The Lorentz-Berthelot rule is applied to obtain the values of LJ mixture well-depth and collision diameter, $\varepsilon_{\mathrm{ft}}$ and $\sigma_{\mathrm{ft}}$, from the pure component parameters. The number density of interaction sites in the carbon wall, $\rho_{\mathrm{t}}$, is equal to 0.114 Å$^{-3}$ [44]. The size and energy parameters of carbon (graphite) are 3.4 Å and 28 K [45].

Constant number of molecules, volume, and temperature (NVT) simulations were performed for nanotubes of radii ranging from 5.42 to 10.85 Å at 300 K with an experimental bulk water density [46] of 0.9965 g/cc within the accessible volume. We choose this temperature and this range of radii as they are relevant to the aqueous nanochannels present in PEMs. [47]. The system contains 499 molecules of water along with 1 hydronium ion for an infinite dilution. For better statistics, 144 independent simulations were run at each state point with different initial configurations. Table 4.1 summarizes the system sizes for each of the nanotubes studied.

The radii studied corresponds to armchair (*R*,*R*) CNTs with indices *R* = 8, 10, 12, 14, and 16. The TIP3P model [48] with flexible OH bond [49] is used for water while the hydronium ion is represented using the same model with modified charges on the O and H atoms [50]. Electrostatic interactions were calculated using the reaction field method [51]. The cut-off distance for non-bonded interactions is 10 Å. The equations of motion are integrated using a two time-scale r-RESPA [52] with a large time step of 2 fs and a small time step of 0.2 fs. Periodic boundary conditions are enforced only in the axial direction of the tube (*z* axis) to yield an infinite long channel. Constant temperature was maintained by incorporating a Nosé–Hoover thermostat [53-55] with a frequency of 0.01 $fs^{-1}$. The high frequency aids the removal of excess heat that was not removed by the local equilibration. Runs of 0.8 ns were initially performed to equilibrate the systems. Then the simulations were run for additional 1 ns for data collection. The trigger values and details of local equilibration involved in the RMD algorithm are same as that employed in bulk water.

Three systems were examined with the above simulation parameters. Simulations of pure confined water (500 molecules) were conducted to benchmark the diffusivities of the TIP3P water model under confinement. A reactive and nonreactive system consisting of water and hydronium are the other two systems considered. A reactive system allows for the structural diffusion and was used to analyze the transport properties of the charge. Nonreactive systems in which the RMD algorithm was not implemented (absence of structural diffusion) were studied to compare the diffusion of the hydronium ion with the vehicular component of the charge in the reactive system.

CNTs of lower radius like 4.07 Å (*R* = 6), where water wires may theoretically exist, were not studied. The parameterization of this RMD algorithm is based on the complex 3D hydrogen bonding network. It is an interesting possibility whether relaxations of the solvation triggers will allow the RMD algorithm to be applied to more confined systems, but that avenue is not pursued in this work, where we strictly adhere to the bulk water RMD parameters.

## 4.3 RESULTS AND DISCUSSION

The effect of confinement within CNTs on some of the physical and transport properties of the proton and water is illustrated here in detail as a function of CNT radius. The snapshots of

a portion of the water and hydronium ion confined in the five CNTs are shown in the Figure 4.2. It is immediately apparent from these snapshots that the hydronium ion is preferentially located at the water/CNT interface with the oxygen atom extended toward the CNT. Both of these visual observations from the snapshots will be discussed in a more quantitative nature below.

### 4.3.1 Radial Density Profile

The distribution profiles of water molecules in confined geometries have been widely studied [56-58]. Figure 4.3(a) represents the density profile of water in a nonreactive system along the radial distance for different channel radius. The density near the CNT wall decreases with the channel radius. The number of peaks in the radial density profile increases as the CNT radius increases, implying the increase in water layers within the tube. At larger CNT radii, the density near the center of tube approaches the bulk water density, which indicates that as the channel radius increases we find bulk water behavior towards the center of the tube where the fluid-tube interaction is weak. In other works, where the CNTs are modeled atomistically both ordered structures (helical [59] or *n*-gonal rings [60], where *n* is based on the radius) and organized layers were observed depending on the geometry of the CNT, pressure, temperature, water model, and many other simulation parameters.

Figure 4.3(b) shows the radial density profile of the hydronium ion in a nonreactive system for different CNT radii. Unlike water, the density near the wall increases as the channel radius increases. From both figures, we can observe that the position of the first peak of the hydronium ion is always closer to the wall than the first peak of water. The very high first peak also shows that the hydronium ion is preferentially located next to the walls. The probability distribution of the orientation of the hydronium ion in the outer and inner layers of the CNT of radius 10.85 Å in the nonreactive system is presented in Figure 4.4. The outer layer is defined 2 Å from the accessible radius. The orientation of the hydronium axis (originating at the midpoint of the three hydrogen atoms and terminating at the position of oxygen atom) is measured with respect to the radial axis. An angle of 0° corresponds to the oxygen atom pointing towards the tube wall. The distribution of orientation in the outer layer shows a strong preference for the ion to be oriented with the oxygen atom, protruding towards the wall with the hydrogen atoms

forming hydrogen bonds with the water molecules in the CNT. However, at the inner layers, no such strong preference for a particular orientation is observed. Similar affinity for the interface and preferential orientation of the hydronium ion has been observed at the interface between a liquid and hydrophobic media or vapor both from simulation [61-64] and experiments [65-67]. The reason behind this phenomenon has been attributed to the energetically favorable formation of hydrogen bonds by the hydronium ion with three water molecules without strongly perturbing the hydrogen bonding network in the aqueous phase.

### 4.3.2 Reaction Rate Constant

The hopping of the proton can be quantitatively described either in the terms of lifetime of the proton or hopping rate. Here, we denote it by reaction rate constant since the structural diffusion is considered as a reaction. The rate constant, $k$, is calculated using the expression:

$$k = \frac{N_{\text{react}}}{\text{time} \cdot V_{\text{tube}}} \times \frac{1}{[\text{H}_2\text{O}][\text{H}_3\text{O}^+]} \tag{4}$$

where $V_{\text{tube}}$ is the accessible nanotube volume excluding the void space near the wall, $N_{\text{react}}$ is the number reactions taken place, *time* is the length of the simulation and the square brackets represent the concentration. The concentrations and $V_{\text{tube}}$ are same for all the CNTs considered, since they all have same density. The definition of reaction needs to be clearly explained in this aspect. The rattling of proton between the reactants is observed in our simulation but they are not taken into account for the calculation of rate constant. At the end of rattling, the proton might end up either in the parent water molecule (starting molecule of rattle) or different water molecule. In either case, we consider a reaction has occurred at the end of rattling. The above definition of reaction is chosen to be consistent with the definition of reaction for proton transport in bulk water [14] whose trigger values are being used. Analysis of the reaction rates of different CNTs shown in Figure 4.5 indicates that there is an upward trend with the tube radius. The reaction rate has increased by roughly an order of magnitude from the smallest to the largest tube. For comparison, the reaction rate constant for structural diffusion of proton in bulk water from experiment [68] is $1.072\times10^{10}$ l/mol/s. The reaction rate constant for structural diffusion of proton in bulk water from the RMD algorithm is $1.090\times10^{10}$ l/mol/s [14]. Both bulk reaction

rates are about an order of magnitude higher than the rate constants found in even the largest CNT studied here.

The reduction in the rate constant can be directly related to the decrease in the probability of the occurrence of reaction. In the RMD algorithm, the event of the reaction is based on the satisfaction of triggers. The fraction satisfying each trigger is presented in Figure 4.6. The order of the trigger analyzed in the plot is based on the hierarchy on which it was verified during the simulation. The particular hierarchy was chosen for computational efficiency and the satisfaction of a particular trigger was tested only when the previous trigger was satisfied. Figure 4.6 contains only six triggers listed, since each fraction was calculated based on the satisfaction of the earlier trigger. Therefore, the first trigger, $r_{\mathrm{OO,Zundel}}$, provided the basis for the calculation of the fraction satisfying the second trigger. Though the preferential location and orientation of the hydronium ions at the wall affect the satisfaction of the geometric trigger, the energetic trigger is identified as the one most affected by confinement and causes a reduction in the structural diffusivity.

Another interesting way to analyze the effect of confinement on the reaction rate constant is to study the reactivity profile along the radial distance. For this purpose, we have chosen the CNT with radius 10.85 Å where the maximum number of reactions takes place. The CNT is divided into cylindrical shells and the number of reactions in each shell is based on the position of the reacting hydronium. The rattling of protons is included in the rate calculation. The reaction rate is provided in Figure 4.7 as a function of the radial distance along with the hydronium concentration. The hydronium ion concentration near the wall is nearly 10 times higher than the inner layers of the CNT. Typically, one considers a reaction rate constant, as shown in Eq. (4), to be independent of concentration. If this was the case, then we would expect the rate to increase by nearly a factor of 10 near the wall. Since we do not see this, we can conclude that the reaction rate constant is not independent of the local concentration and, in fact, decreases with increasing hydronium concentration. This same decrease in rate constant with increasing hydronium ion concentration is also observed in the aqueous HCl system [14], although to a lesser extent.

### 4.3.3 Water Diffusivity

The diffusion coefficient of bulk water can be calculated using the Einstein expression, which relates the diffusivity to the mean square displacement (MSD) of a molecule as

$$D = \lim_{\tau \to \infty} \frac{\left\langle [r(t+\tau) - r(t)]^2 \right\rangle}{2d\tau} \tag{5}$$

where $d$ is the dimensionality of the system and $\tau$ is the observation time. In the CNT, we apply this expression to evaluate the diffusion coefficient in only the axial dimension. Since the movement of the molecules is restricted by confinement in the other two directions (radial axis), the trajectories would not reach the long-time limit required by the Einstein relation in the radial dimension. In a confined geometry, the diffusion of water can be described by three mechanisms: [69] Fickian $(\text{MSD} \propto \tau)$, single-file $(\text{MSD} \propto \tau^{1/2})$, and ballistic $(\text{MSD} \propto \tau^2)$. Single file motion will be observed only if the pore is so small that water molecules cannot pass each other within the tube [70]. This is not the case in any of these simulations. Striolo [69] observed the molecules in the CNT (8,8) to initially follow a ballistic transport but in the long run evolve into Fickian diffusion. Therefore, in the CNTs considered, we expect Fickian diffusion in the long-time limit.

We have calculated the water diffusivity in the axial direction in all the three systems considered. Axial diffusivity measurement in pure confined water and nonreactive systems can be done without ambiguity, while the reactive system which involves the change in the identity of the molecules needs attention. Therefore, instead of calculating the diffusivity through the entire simulation time involving reactions we calculated the water diffusivities in the reactive system for time segments in which they did not react. Figure 4.8 shows the axial water diffusivity in the various systems against CNT radius along with the bulk water density at 300 K. The reason we compare the diffusivities of three systems is to show that the presence of the hydronium ion and implementation of RMD algorithm do not affect the water diffusivity. The diffusivities of all the three systems are almost the same. They initially increase with the channel radius but later stabilize. At larger radii, we find the water diffusivity to be slightly higher than the bulk water diffusivity. This might be explained due to the fact the choice of accessible volume impacts the fluid density, which can have considerable influence on the diffusion

coefficient. For example, when the CNT of radius 10.85 Å has its density changed from 0.9965 to 1.15 g/cc, it causes a 22% reduction in the water diffusivity.

Liu *et al.* [59] measured the diffusivity of water in an atomistically modeled armchair (*R,R*) CNT with indices $R$ = 8, 10, 12, 14, 16 and found a steady increase in the water axial diffusivity with the increase in radius and found values below that of their bulk water diffusivity. With the increase in confinement of channels (from 5 – 2 Å) Brewer *et al.* [36] observed a similar trend of decrease in the water diffusivity, which was also less than the bulk phase.

### 4.3.4 Charge Diffusivity

The transport properties of the charge and its components were measured using the Einstein relation. In the nonreactive system, the diffusivity of the charge is equal to the vehicular diffusion of the hydronium ion. In the RMD simulation, the excess charge hops from one water molecule to another, temporarily creating hydronium ions from each molecule. The hydronium ion trajectories can be unambiguously followed using the center-of-mass position of the ion. Decoupling the total charge movement into the two components can be easily done by enforcing the following relationship

$$\Delta\vec{r}_{\text{tot}} = \Delta\vec{r}_{\text{veh}} + \Delta\vec{r}_{\text{struct}} \tag{6}$$

By the implementation of the above constraint in each step, the total displacement vector is equal to the sum of the displacement vectors attributed by both the vehicular and structural components. Similar decomposition of the total charge displacement vector has been performed earlier [71]. The vehicular component is continuously measured whether a reaction takes place or not. During the absence of reaction, the displacement due to structural diffusion is zero and the vehicular component is the sole contributor to the total charge diffusion. When a reaction takes place, the displacement due to the Newtonian motion (MD step) is categorized as the vehicular contribution, while the displacement of the reactant hydronium from the location before reaction (position at the end of MD step) to the final position of the product hydronium after local equilibration is considered as the structural displacement. The relationship between the vehicular, $D_{\text{veh}}$, structural, $D_{\text{struct}}$, and total charge diffusion, $D_{\text{tot}}$ can be obtained by substituting Eq. (6) in Einstein's relation (Eq. (5)) as follows:

$$D_{\text{tot}} = \lim_{\tau \to \infty} \frac{\left\langle \Delta \vec{r}_{\text{veh}}^{\,2} \right\rangle + \left\langle \Delta \vec{r}_{\text{struct}}^{\,2} \right\rangle + 2\left\langle \Delta \vec{r}_{\text{veh}} \Delta \vec{r}_{\text{struct}} \right\rangle}{2d\tau} \tag{7}$$

By making an arbitrary but reasonable definition of decomposition, we get:

$$D_{\text{veh}} \equiv \lim_{\tau \to \infty} \frac{\left\langle \Delta \vec{r}_{\text{veh}}^{\,2} \right\rangle}{2d\tau} \tag{7.a}$$

$$D_{\text{struct}} \equiv \lim_{\tau \to \infty} \frac{\left\langle \Delta \vec{r}_{\text{struct}}^{\,2} \right\rangle}{2d\tau} \tag{7.b}$$

$$D_{\text{corr}} \equiv \lim_{\tau \to \infty} \frac{2\left\langle \Delta \vec{r}_{\text{veh}} \Delta \vec{r}_{\text{struct}} \right\rangle}{2d\tau} \tag{7.c}$$

where $D_{\text{corr}}$ is the correlation term that denotes the coupling between the structural and vehicular contributions. If $D_{\text{corr}} = 0$, then both the components of the total charge diffusion are uncorrelated. Analogous to the estimation of water diffusion coefficients, we have reported only the diffusivities of the charge in the axial direction.

The total charge diffusivity and the individual contributions of the two diffusion mechanisms in the axial direction for the various CNTs considered are shown in Figure 4.9 along with the vehicular diffusion of hydronium in the nonreactive system. The uncertainties are represented as the standard error [72]. The total diffusion and vehicular component follow the same trend where an initial increase in the radius of CNT caused a steep increase in the axial diffusivities and further reduction in the confinement (radius > 8.14 Å) did not affect them tremendously. On the other hand, the structural component showed steady increase with the reduction of confinement.

The implementation of RMD algorithm should not affect the fluid vehicular diffusivities. Similar to the case of measurement of water diffusivity, the vehicular diffusion of the hydronium ion in a nonreactive system is compared to the vehicular component of charge diffusion in a reactive system and is found to be in agreement within the standard errors.

A better way to understand the effect of confinement on the charge diffusion would be to compare these diffusivity values to that of bulk water from our previous work. The total, structural, and vehicular diffusivities of proton in bulk water at 300 K are $7.33\times10^{-5}$, $4.29\times10^{-5}$ and $2.83\times10^{-5}$ $\text{cm}^2/\text{s}$ based on our algorithm [14]. When we compare these values to the CNT

with the largest radius, we find the vehicular diffusivities are virtually the same while the structural component is only 12% of the value observed in bulk water. This can be explained by the obvious reduction in the rate constant. So in overall there is 58% reduction in the total charge diffusion at our largest CNT due to confinement.

We found the two components of charge diffusivity in bulk water to be uncorrelated and structural diffusion contributing to about 60% of the charge diffusion. The vehicular component is the major contributor of the charge diffusion in CNTs for the range of radius we investigated, and both the components are uncorrelated. We can also conclude confinement affects the structural diffusion much more than the vehicular diffusion.

Proton transport in confined water has been previously studied. The mobility of proton was much higher [34,37] in 1D water wires in armchair (6,6) CNTs (radius = 4.07 Å) than observed in bulk water. However, in cylindrical channels with 3D water structure, the proton diffusivity was computed to be much lower than observed in bulk water but increased with channel diameter [36]. The center of excess charge diffusion coefficient in a cylindrical channel of carbon with radius and length of 5 and 29.8 Å, respectively, containing 77 water molecules was about $2.5\times10^{-5}$ $cm^2/s$ [36] compared to the computed value of $4.5\pm1.1\times10^{-5}$ $cm^2/s$ in bulk water using MS-EVB model. The charge diffusivity at our smallest CNT of radius 5.42 Å is $1.30\times10^{-5}$ $cm^2/s$ compared to the value of $7.33\times10^{-5}cm^2/s$ in bulk water. Therefore, we observe the same qualitative trend with the RMD algorithm as is observed with the MS-EVB model.

## 4.4 CONCLUSIONS

Proton mobility through water confined in CNTs of radius ranging from 5.42 – 10.85 Å at 300 K and infinite dilution has been investigated by means of classical MD simulations with the structural diffusion modeled with an RMD algorithm. The algorithm, parameterized for a bulk water system, was directly implemented to the CNT systems without any modifications. The algorithm has successfully captured the essential features of the structural diffusion under confinement, confirming its facile adaptability to different environments.

The radial density profiles of both water and hydronium ions were computed. The radial water profile showed layered structures in the confined geometries with higher density near the walls and an increase in the number of layers with increasing radius. Hydronium ions showed a

great affinity towards the wall and were preferentially oriented with the oxygen atom facing the wall. The reaction rate constant for the proton transfer process increased with the decrease in confinement due to requirement imposed by the energetic trigger. The axial water diffusivity was not affected by the presence of protons in dilute concentrations or by the implementation of the RMD algorithm. The diffusion coefficients initially increased with the increase in the radius of the CNT but approached a plateau at the larger tube sizes. The axial vehicular diffusion of hydronium ions showed analogous behavior. The axial structural component of charge diffusion showed a steady increase with increasing diameter of the CNT. The two components were determined to be uncorrelated with the axial total charge diffusivity, essentially being the sum of the two components. We observed that the vehicular component of the charge diffusivity was the same as that in bulk water in the largest diameter CNT. However, the structural component of charge diffusivity was only 12% of the value observed in bulk water. Clearly, confinement impacts structural diffusion at larger tube sizes and in a more significant manner than vehicular diffusion.

This work impacts the design This work impacts the design of novel PEMs because it indicates that a severe reduction in the structural component of the charge diffusivity occurs as a consequence of confinement. The coupled effects of confinement and high acidity, as present in PEMs, remain of interest.

## 4.5 ACKNOWLEDGEMENT

This work is funded by the U.S. Department of Energy (DOE) BES under contract number DE-FG02-05ER15723. This research used resources of the Center for Computational Sciences at Oak Ridge National Laboratory (ORNL) supported by the Office of Science of the DOE (contract number DE-AC05-00OR22725) and National Institute for Computational Sciences (NICS) supported by the National Science Foundation (agreement number OCI 07-11134).

# References

[1] Kreuer, K. D., *J. Membr. Sci.* **185**, 29 (2001).

[2] Kreuer, K. D.; Schuster, M.; Obliers, B.; Diat, O.; Traub, U.; Fuchs, A.; Klock, U.; Paddison, S. J. and Maier, J., *J. Power Sources* **178**, 499 (2008).

[3] Agmon, N., *Chem. Phys. Lett.* **244**, 456 (1995).

[4] Tuckerman, M.; Laasonen, K.; Sprik, M. and Parrinello, M., *J. Chem. Phys.* **103**, 150 (1995).

[5] Marx, D.; Tuckerman, M. E.; Hutter, J. and Parrinello, M., *Nature* **397**, 601 (1999).

[6] Robison, R. A. and Stokes, R. H., *Electrolyte Solutions*, Butterworths, London (1959).

[7] Zundel, G. and Metzger, H., *Z. Phys. Chem.* **58**, 225 (1968).

[8] Wicke, E.; Eigen, M. and Ackermann, T., *Z. Phys. Chem.* **1**, 340 (1954).

[9] Markovitch, O.; Chen, H.; Izvekov, S.; Paesani, F.; Voth, G. A. and Agmon, N., *J. Phys. Chem. B* **112**, 9456 (2008).

[10] Paddison, S. J.; Bender, G.; Kreuer, K. D.; Nicoloso, N. and Zawodzinski, T. A., *J. New Mater. Electrochem. Systems* **3**, 291 (2000).

[11] Lu, Z. J.; Lanagan, M.; Manias, E. and Macdonald, D. D., *J. Phys. Chem. B* **113**, 13551 (2009).

[12] Paul, R. and Paddison, S. J., *J. Chem. Phys.* **115**, 7762 (2001).

[13] Paul, R. and Paddison, S. J., *J. Phys. Chem. B* **108**, 13231 (2004).

[14] Esai Selvan, M.; Keffer, D. J.; Cui, S. and Paddison, S. J., *J. Chem. Phys. B* **Submitted**, (2009).

[15] Zawodzinski, T. A.; Springer, T. E.; Davey, J.; Jestel, R.; Lopez, C.; Valerio, J. and Gottesfeld, S., *J. Electrochem. Soc.* **140**, 1981 (1993).

[16] Kreuer, K. D., *Solid State Ionics* **97**, 1 (1997).

[17] Paddison, S. J. and Paul, R., *Phys. Chem. Chem. Phys.* **4**, 1158 (2002).

[18] Kreuer, K.-D.; Paddison, S. J.; Spohr, E. and Schuster, M., *Chem. Rev.* **104**, 4637 (2004).

[19] Petersen, M. K.; Wang, F.; Blake, N. P.; Metiu, H. and Voth, G. A., *J. Phys. Chem. B* **109**, 3727 (2005).

[20] Kreuer, K. D., *Solid State Ionics* **136**, 149 (2000).

[21] Paddison, S. J., *Ann. Rev. Mater. Res.* **33**, 289 (2003).

[22] Eikerling, M.; Paddison, S. J.; Pratt, L. R. and Zawodzinski, T. A. J., *Chem. Phys. Lett.* **368**, 108 (2003).

[23] Hayes, R. L.; Paddison, S. J. and Tuckerman, M. E., *J. Chem. Phys. B* in press.

[24] Car, R. and Parrinello, M., *Phys. Rev. Lett.* **55**, 2471 (1985).

[25] Billeter, S. R. and van Gunsteren, W. F., *J. Phys. Chem. A* **102**, 4669 (1998).

[26] Intharathep, P.; Tongraar, A. and Sagarik, K., *J. Comput. Chem.* **27**, 1723 (2006).

[27] Warshel, A. and Weiss, R. M., *J. Am. Chem. Soc.* **102**, 6218 (1980).

[28] Schmitt, U. W. and Voth, G. A., *J. Chem. Phys.* **111**, 9361 (1999).

[29] Wang, F. and Voth, G. A., *J. Chem. Phys.* **122**, 144105 (2005).

[30] Wu, Y. J.; Chen, H. N.; Wang, F.; Paesani, F. and Voth, G. A., *J. Phys. Chem. B* **112**, 467 (2008).

[31] Schmidt, R. G. and Brickmann, J., *Ber. Bunsen-Ges. Phys. Chem. Chem. Phys.* **101**, 1816 (1997).

[32] Lill, M. A. and Helms, V., *J. Chem. Phys.* **115**, 7993 (2001).

[33] Jiang, B. W.; Selvan, M. E.; Keffer, D. J. and Edwards, B. J., *J. Phys. Chem. B* **113**, 13670 (2009).

[34] Mann, D. J. and Halls, M. D., *Phys. Rev. Lett.* **90**, 4 (2003).

[35] Lee, S. H., *Bull. Korean Chem. Soc.* **30**, 700 (2009).

[36] Brewer, M. L.; Schmitt, U. W. and Voth, G. A., *Biophys. J.* **80**, 1691 (2001).

[37] Dellago, C.; Naor, M. M. and Hummer, G., *Phys. Rev. Lett.* **90**, (2003).

[38] Holt, J. K., *Adv. Mater.* **21**, 3542 (2009).

[39] Alexiadis, A. and Kassinos, S., *Chem. Eng. Sci.* **63**, 2047 (2008).

[40] Hummer, G.; Rasaiah, J. C. and Noworyta, J. P., *Nature* **414**, 188 (2001).

[41] LyndenBell, R. M. and Rasaiah, J. C., *J. Chem. Phys.* **105**, 9266 (1996).

[42] Gordillo, M. C. and Marti, J., *Chem. Phys. Lett.* **329**, 341 (2000).

[43] Peterson, B. K.; Walton, J. and Gubbins, K. E., *J. Chem. Soc., Faraday Trans. 2* **82**, 1789 (1986).

[44] McCallum, C. L.; Bandosz, T. J.; McGrother, S. C.; Muller, E. A. and Gubbins, K. E., *Langmuir* **15**, 533 (1999).

[45] Steele, W. A., *The Interaction of Gases with Solid Surfaces*, Pergamon Press, Oxford (1974).

[46] Kell, G. S., *J. Chem. Eng. Data* **20**, 97 (1975).

[47] Cui, S. T.; Liu, J. W.; Esai Selvan, M.; Keffer, D. J.; Edwards, B. J. and Steele, W. V., *J. Phys. Chem. B* **111**, 2208 (2007).

[48] Jorgensen, W. L.; J. Chandrasekhar, J.; Madura, J. D.; Impey, R. W. and Klein, M. L., *J. Chem. Phys.* **79**, 926 (1983).

[49] Neria, E.; Fischer, S. and Karplus, M., *J. Chem. Phys.* **105**, 1902 (1996).

[50] Urata, S.; Irisawa, J.; Takada, A.; Shinoda, W.; Tsuzuki, S. and Mikami, M., *J. Phys. Chem. B* **109**, 4269 (2005).

[51] Hummer, G.; Soumpasis, D. M. and Neumann, M., *Mol. Phys.* **77**, 769 (1992).

[52] Tuckerman, M.; Berne, B. J. and Martyna, G. J., *J. Chem. Phys.* **97**, 1990 (1992).

[53] Nosé, S., *J. Chem. Phys.* **81**, 511 (1984).

[54] Nosé, S., *Mol. Phys.* **52**, 255 (1984).

[55] Hoover, W. G., *Phys. Rev. A* **31**, 1695 (1985).

[56] Gallo, P.; Ricci, M. A. and Rovere, M., *J. Chem. Phys.* **116**, 342 (2002).

[57] Hirunsit, P. and Balbuena, P. B., *J. Phys. Chem. C* **111**, 1709 (2007).

[58] Cicero, G.; Grossman, J. C.; Schwegler, E.; Gygi, F. and Galli, G., *J. Am. Chem. Soc.* **130**, 1871 (2008).

[59] Liu, Y. C.; Wang, Q.; Wu, T. and Zhang, L., *J. Chem. Phys.* **123**, (2005).

[60] Mashl, R. J.; Joseph, S.; Aluru, N. and Jakobsson, E., *Biophys. J.* **84**, 488A (2003).

[61] Vacha, R.; Horinek, D.; Berkowitz, M. L. and Jungwirth, P., *Phys. Chem. Chem. Phys.* **10**, 4975 (2008).

[62] Petersen, M. K.; Iyengar, S. S.; Day, T. J. F. and Voth, G. A., *J. Phys. Chem. B* **108**, 14804 (2004).

[63] Esai Selvan, M.; Liu, J.; Keffer, D. J.; Cui, S.; Edwards, B. J. and Steele, W. V., *J. Phys. Chem.C* **112**, 1975 (2008).

[64] Lee, H. S. and Tuckerman, M. E., *J. Phys. Chem. A* **113**, 2144 (2009).

[65] Miranda, P. B. and Shen, Y. R., *J. Phys. Chem. B* **103**, 3292 (1999).

[66] Gopalakrishnan, S.; Liu, D. F.; Allen, H. C.; Kuo, M. and Shultz, M. J., *Chem. Rev.* **106**, 1155 (2006).

[67] Tian, C. S.; Ji, N.; Waychunas, G. A. and Shen, Y. R., *J. Am. Chem. Soc.* **130**, 13033 (2008).

[68] Luz, Z. and Meiboom, S., *J. Am. Chem. Soc.* **86**, 4768 (1964).

[69] Striolo, A., *Nano Lett.* **6**, 633 (2006).

[70] Keffer, D.; McCormick, A. V. and Davis, H. T., *Mol. Phys.* **87**, 367 (1996).

[71] Petersen, M. K. and Voth, G. A., *J. Phys. Chem. B* **110**, 18594 (2006).

[72] Flyvbjerg, H. and Petersen, H. G., *J. Chem. Phys.* **91**, 461 (1989).

# Appendix E

## Tables and Figures

**Table 4.1.** Physical dimensions of the simulated CNTs [a]

| Tube radius (Å) | Length of tube (Å) | Radius accessible (Å) |
|---|---|---|
| 5.42 | 364.29 | 3.62 |
| 6.78 | 200.46 | 4.88 |
| 8.14 | 124.59 | 6.19 |
| 9.49 | 82.87 | 7.59 |
| 10.85 | 60.81 | 8.86 |

[a] All simulations have been performed at 300 K and a density of 0.9965 g/cc with 500 molecules of $H_2O$ or 499 $H_2O$ molecules and 1 $H_3O^+$ cation.

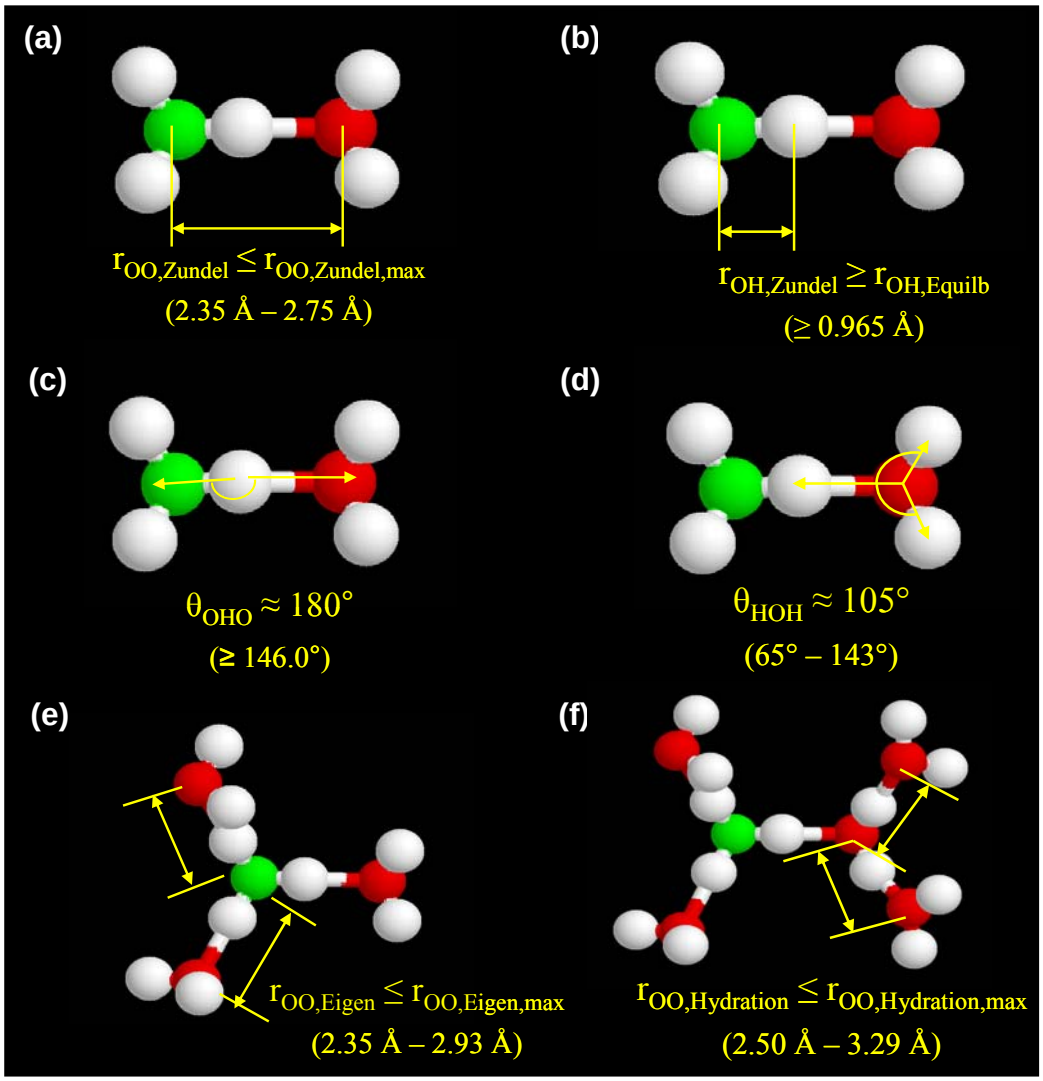


**Figure 4.1.** Graphical representation of six geometric triggers for structural diffusion: **(a)** O–O separation must form a Zundel ion, **(b)** $O^*$–H separation must exceed the equilibrium bond distance, **(c)** ∠OHO is nearly linear in the Zundel ion, **(d)** lone pair of electrons in the water should point towards the proton, **(e)** initial $H_3O^+$ forms an Eigen ion, and **(f)** Eigen ion is formed around final $H_3O^+$. These six geometric triggers must be satisfied along with the energetic trigger for the reaction to take place. The allowable range of the triggers is listed in parentheses. O of $H_3O^+$, green; O of $H_2O$, red; H, white.

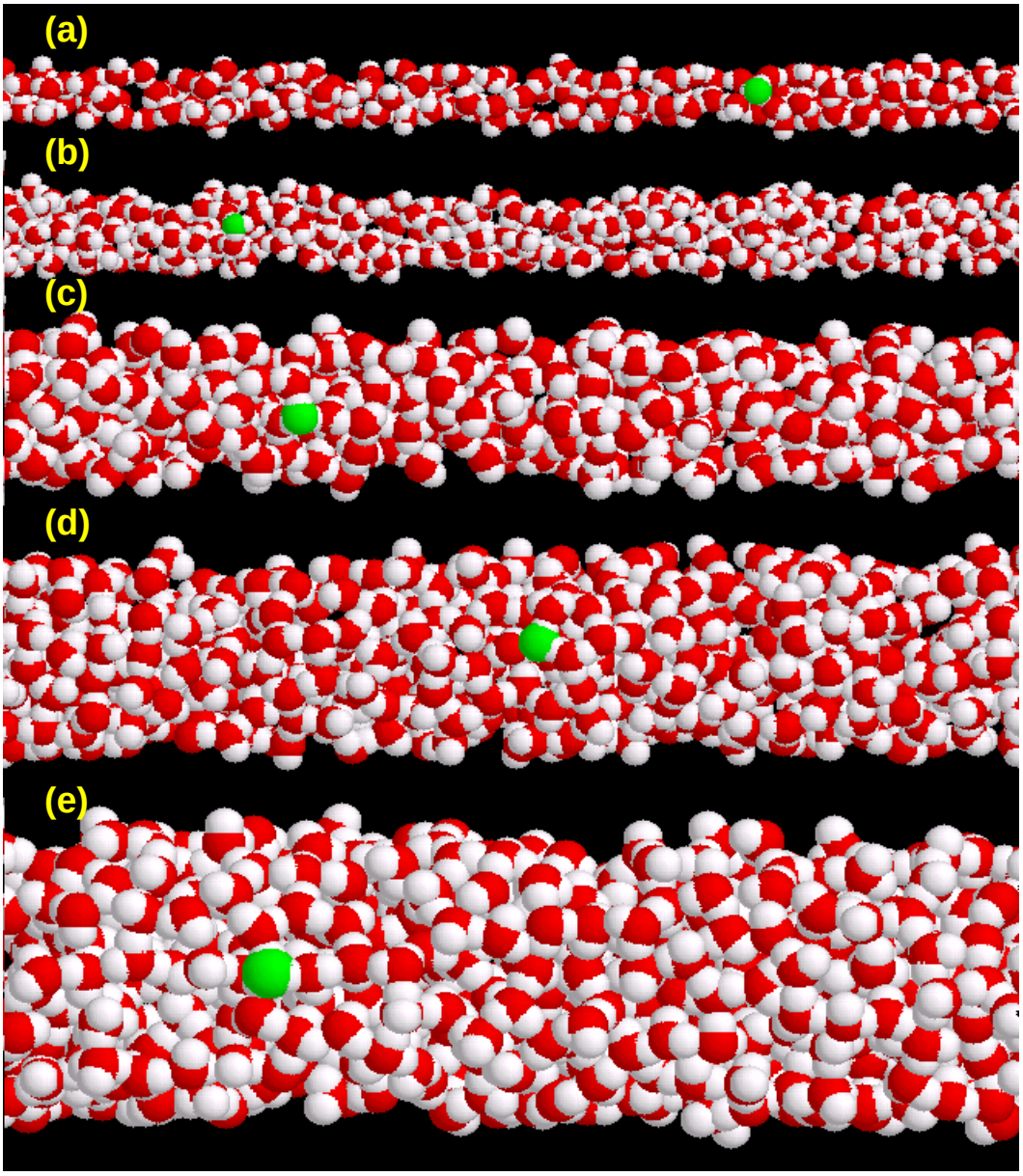


**Figure 4.2.** Snapshot of a portion of the CNTs studied whose radii are **(a)** 5.42 Å, **(b)** 6.78 Å, **(c)** 8.14 Å, **(d)** 9.49 Å, and **(e)** 10.85 Å. O of $H_3O^+$, green; O of $H_2O$, red; H, white.

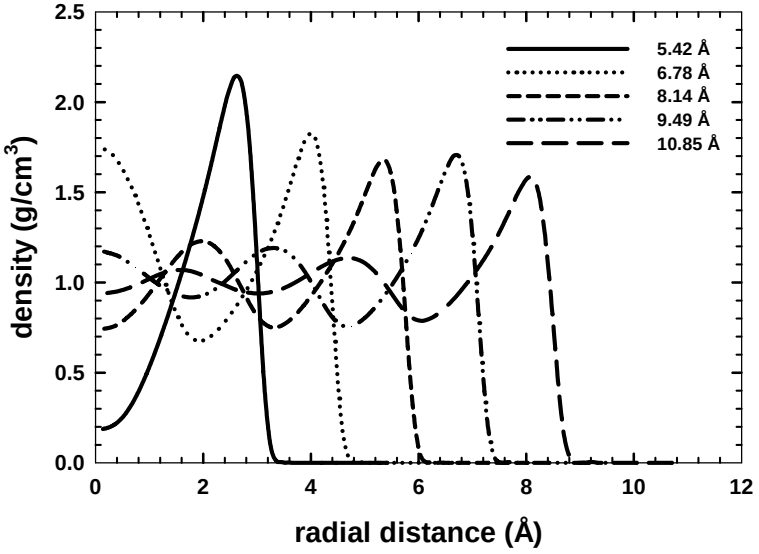


**(a)**

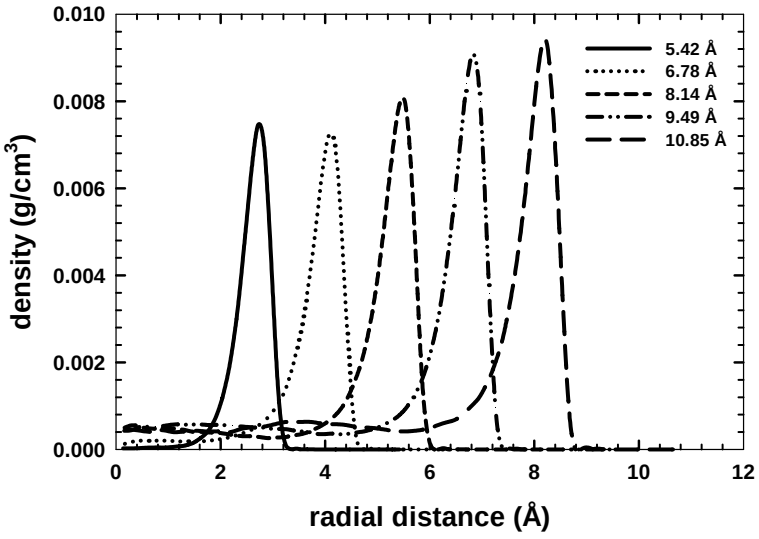


**(b)**

**Figure 4.3.** Radial density profile of **(a)** water and **(b)** hydronium confined in CNTs with different radii in the nonreactive system.

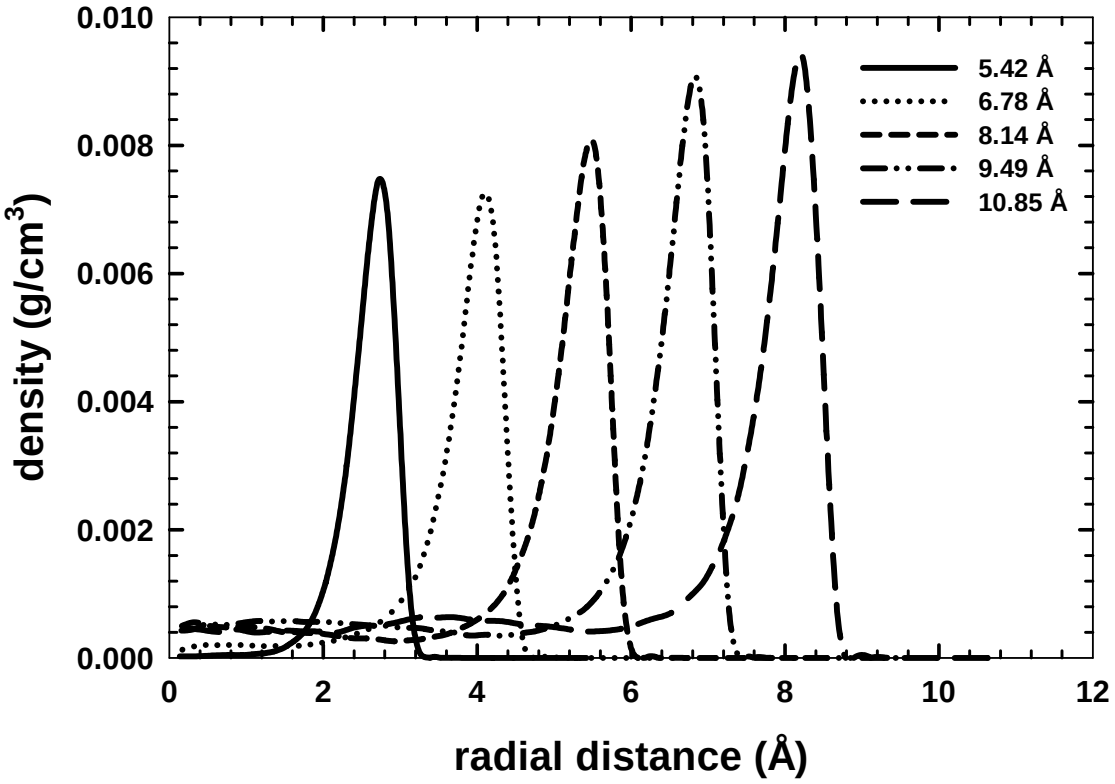


**Figure 4.4.** Probability distribution of the orientation of the hydronium ion with respect to the radial axis in the outer (dashed line) and inner layers (solid line) of the CNT with radius 10.85 Å. Measurement of cos $\theta = 1$ corresponds to the oxygen atom pointing towards the wall.

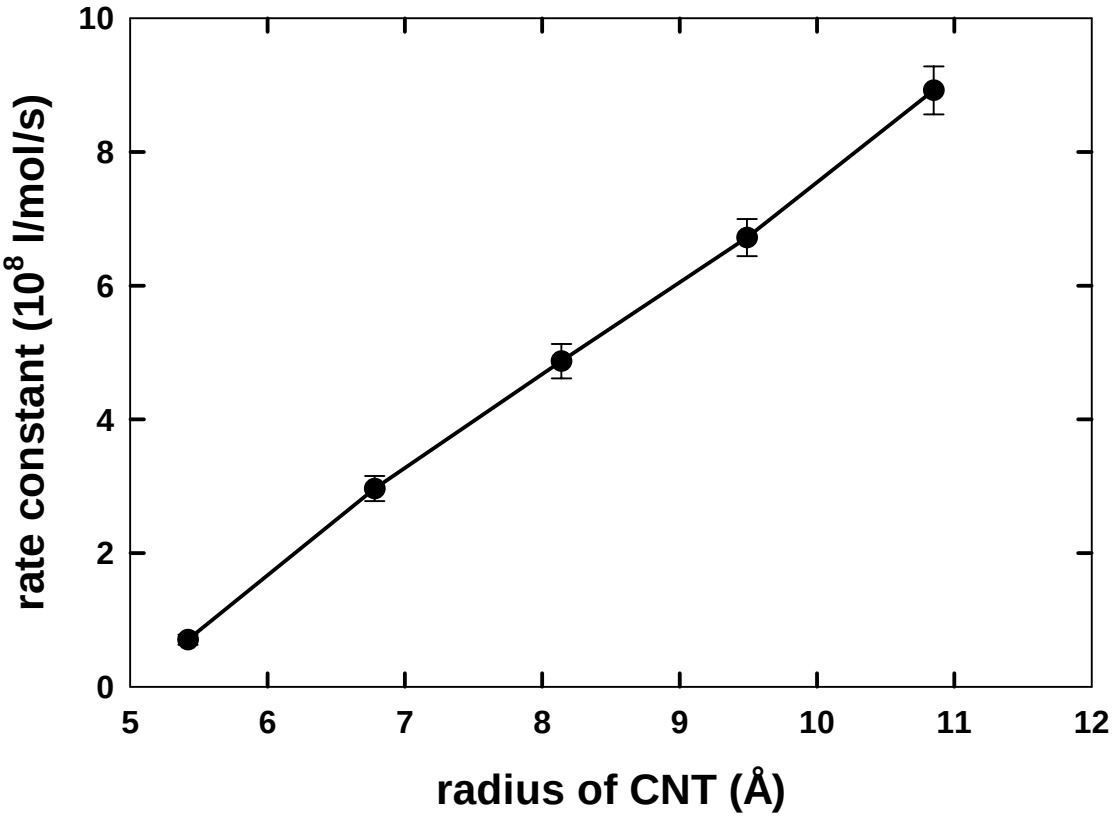


**Figure 4.5.** Reaction rate constant, *k*, as a function of CNT radius. An increase in the *k* is observed with the increase the radius.

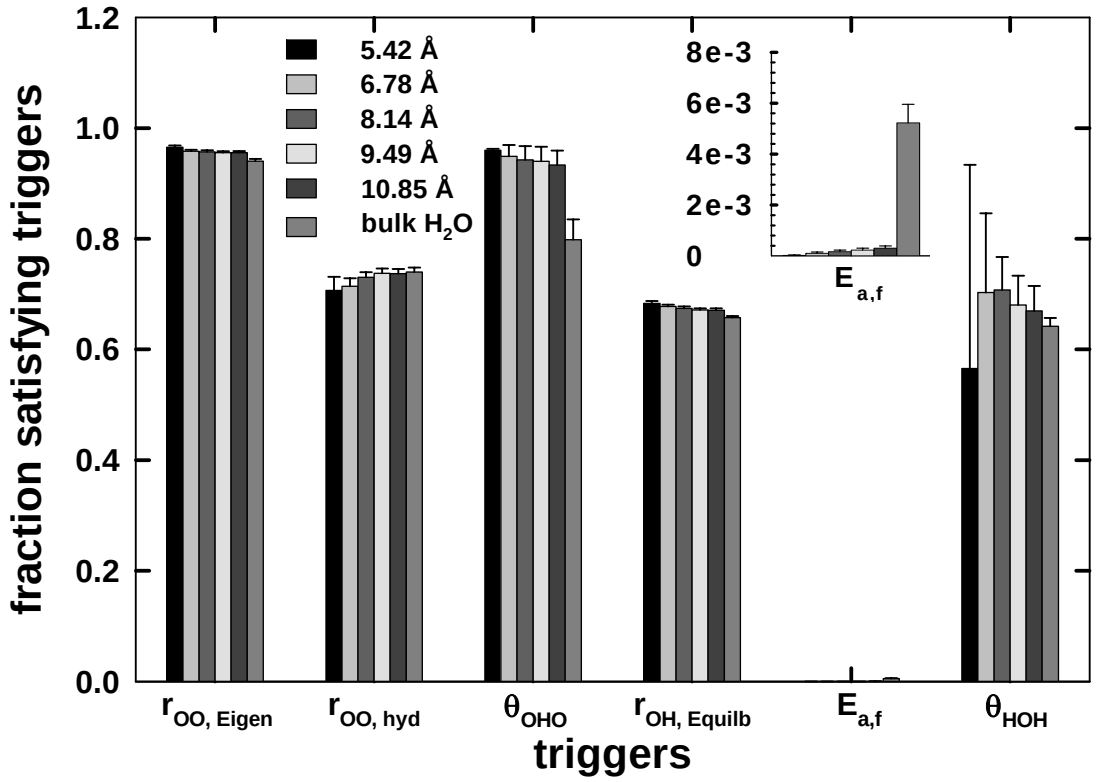


**Figure 4.6.** Histogram of the fraction satisfying the geometric and energetic triggers in the various CNTs studied. Each fraction is calculated based on the satisfaction of the previous trigger. Data from bulk water are also included to observe the effect of confinement on trigger satisfaction.

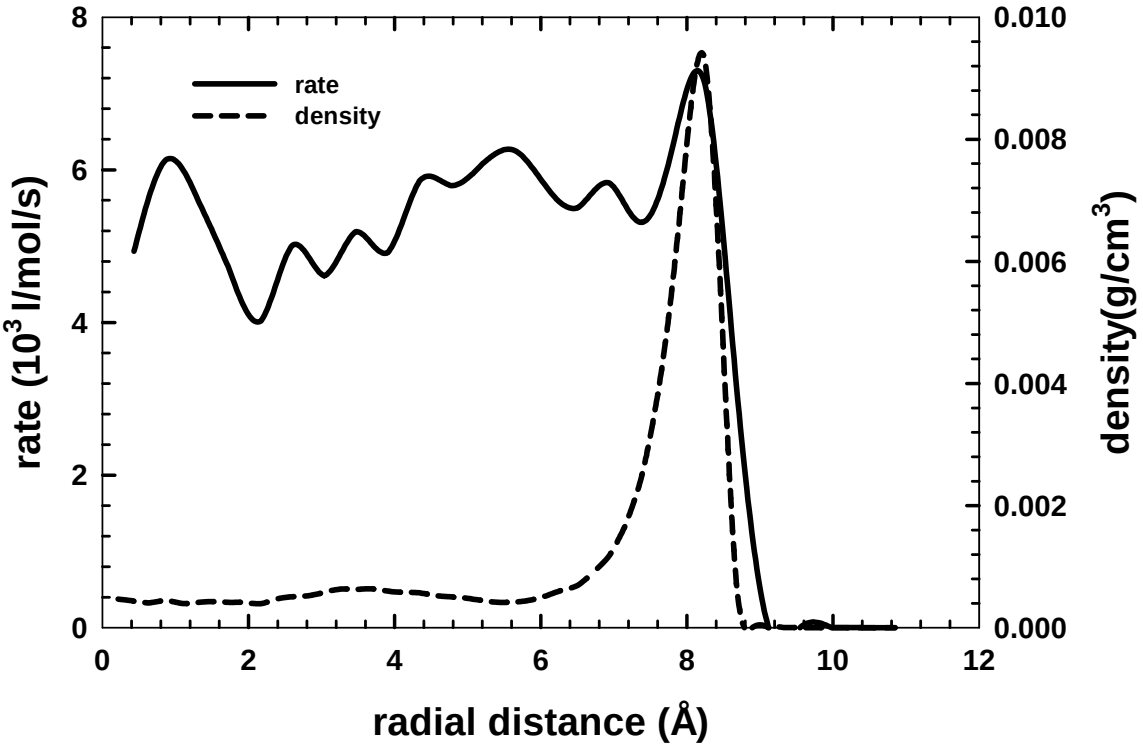


**Figure 4.7.** Rate, *r*, profile (solid line) along the radial distance of CNT of radius 10.85 Å. The radial hydronium concentration profile (dotted line) is provided to analyze the effect of the concentration on rate under confinement.

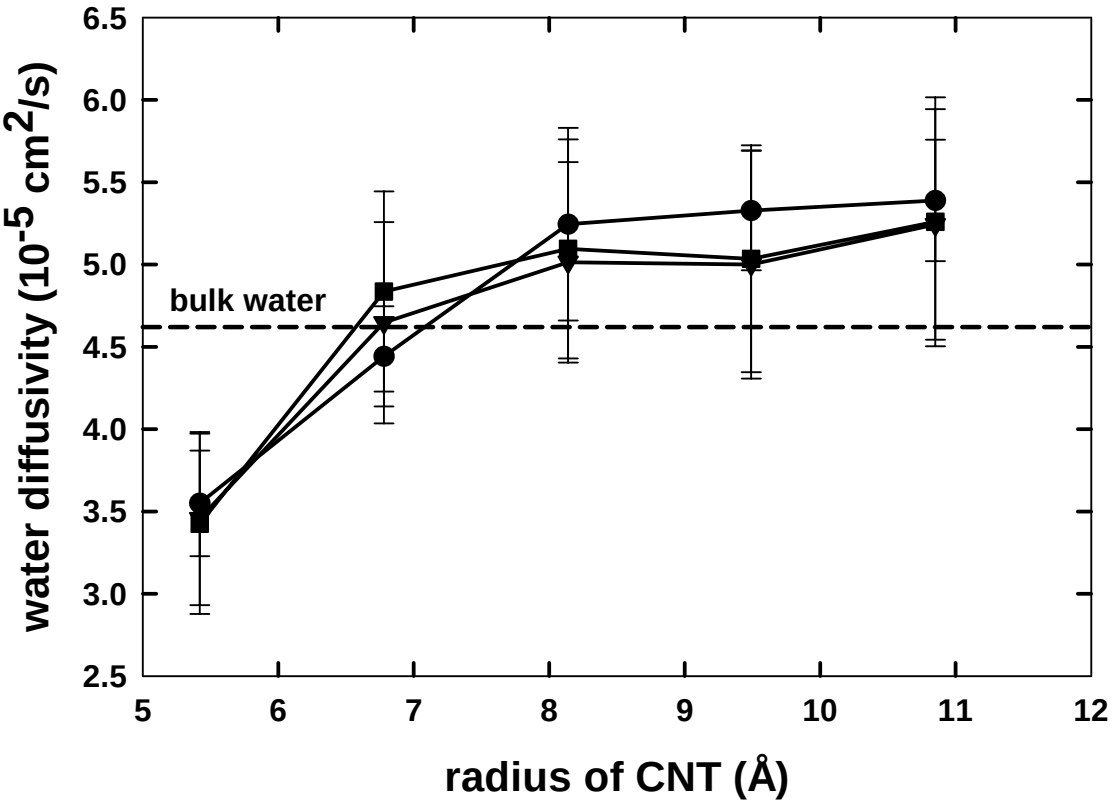


**Figure 4.8.** Water diffusivity along the tube axis for the (i) pure confined water system, solid circle; (ii) nonreactive system, solid triangle; (iii) reactive system, solid squares expressed as a function of CNT radius. The dashed line represents the bulk water diffusivity of a TIP3P model at 300 K.

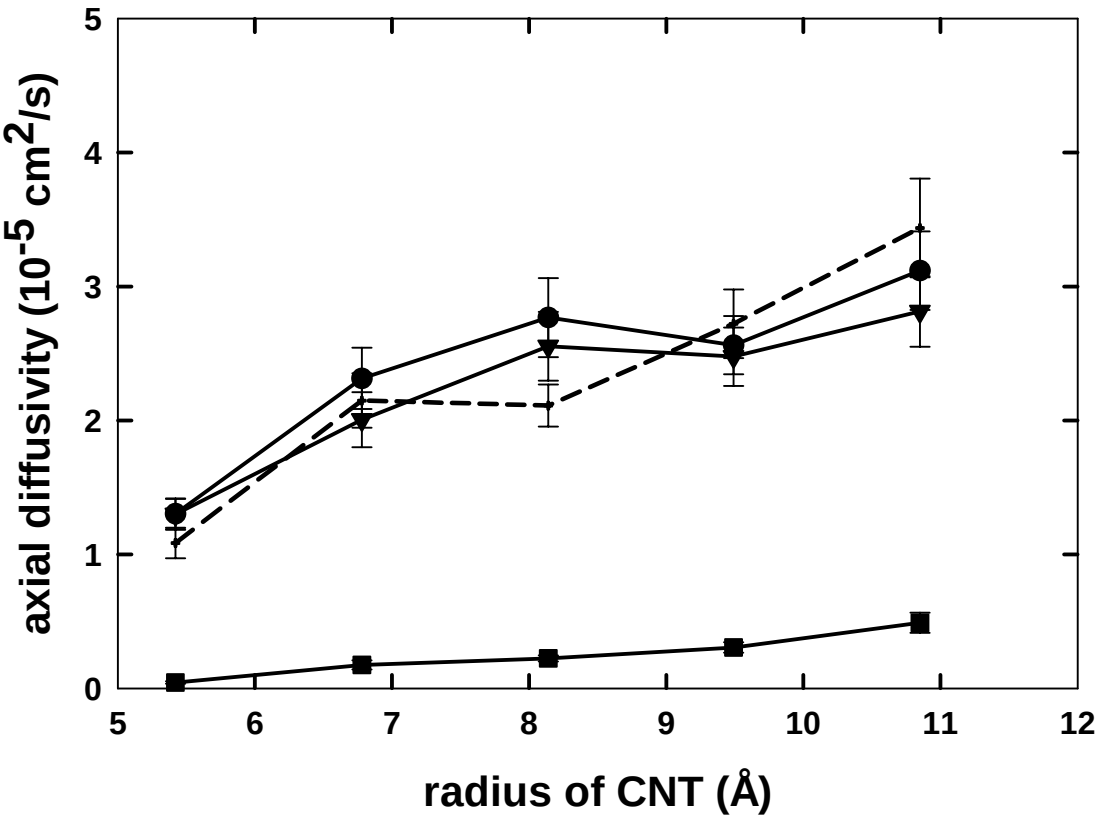


**Figure 4.9.** The axial total charge diffusivity (solid circles) and its two components (i) vehicular (solid triangles) and (ii) structural component (solid squares) for the various CNTs studied in a reactive system. The dashed line represents the vehicular diffusion of $H_3O^+$ in the nonreactive system.

# CHAPTER 5

# A Reactive Molecular Dynamics Study of Proton Transport in Polymer Electrolyte Membrane

This chapter is a revised version of a paper (minor revisions to reflect its inclusion as a chapter in the dissertation) by the same title in preparation for a journal by Myvizhi Esai Selvan, David J. Keffer, Shengting Cui, and Stephen J. Paddison:

The use of "we" in this part refers to the co-authors and the author of this dissertation. My primary contributions to this paper include (1) all of the simulation work (2) analysis of data, and (3) most of the writing

**Abstract**

The transport properties of water and protons in Nafion with an equivalent weight of 1144 are studied using a recently developed reactive molecular dynamics (RMD) algorithm. The algorithm takes input from both quantum mechanical and macroscopic models of structural diffusion of a proton and incorporates them in a classical MD simulation *via* three steps (i) trigger satisfaction, (ii) instantaneous reaction, and (iii) local equilibration. Previously the algorithm has effectively captured the individual effect of temperature, confinement and acidity on the structural diffusion of a proton and is currently applied to Nafion 1144, which contains an aqueous domain influenced both by acidity and confinement at 300 K for $\lambda$ = 6, 9, 15, and 22. We have modeled the structural diffusion of protons via a mechanism similar to that observed in bulk aqueous systems. The reactivity of the structural diffusion is measured in terms of a rate constant and is found to increase with hydration level. The contribution of the structural and vehicular components and their correlation to the total charge diffusion are discussed. The components are found to be anti-correlated with the correlation decreasing with an increase in water content. The total charge diffusivity is higher than the experimentally measured values due to a high vehicular component that resulted from insufficient local equilibration. A similar increase is reflected in the water diffusivity of current system when compared to the diffusivities from classical MD simulation. We have also analyzed various local equilibration schemes to lower the water diffusivity and identified that the minimization of energy plays significant role in the re-establishment of a stable hydrogen bond network after reaction.

## 5.1 INTRODUCTION

Proton exchange membrane fuel cells (PEMFC) are compact and highly efficient power generators for stationary and transportation applications at low temperature operating conditions with tremendous potential to reduce oil dependence and carbon emissions [1]. The proton exchange membrane (PEM) is the polymer electrolyte employed in a PEMFC and in a hydrated state is responsible for the conduction of proton from anode to cathode. An ideal PEM is expected to have mechanical integrity, chemical stability, long term durability, high proton conductivity at extreme operating conditions of low humidity or high temperature and low cost of production. Currently, no existing membrane exhibits all of the above properties. The proton conduction critically depends on the PEM morphology which in turn is influenced by the water content [2-5] and polymer chemistry [6-9]. Toward this end, a molecular level understanding of the structure-property relationship is not only important for the improvement in performance of the existing PEMs but also in the design of novel PEMs with superior characteristics [10,11].

Proton diffusion in bulk water occurs through a combination of both vehicular (conventional mass diffusion as $H_3O^+$ ion) and structural diffusion (translocation of $H^+$ from a water molecule to another through rearrangement of hydrogen bonds) [12,13] mechanisms. Structural diffusion is responsible for the anomalous high transport mobility of protons in aqueous solutions compared to other cations of same size [14]. The mechanism involves continual interconversion between the two limiting configurations namely Zundel and Eigen complexes accompanied by breaking and forming of hydrogen bonds in the solvation shells around the excess charge [12,15]. In a PEM fuel cell, the proton diffuses from the anode to cathode through the aqueous domain in a PEM. These aqueous clusters differ from that of bulk water because of their dimension in nanometers and presence of acidic moiety from the side chain of PEM. There is evidence from theory and simulation suggesting that both proton transport mechanisms are active in PEM [16-18] with an increase in structural diffusion occurring at high hydration level [7].

Experimentally proton conductivity can be measured through electrochemical impedance spectroscopy [19], DC four-point probe electric conductivity [20], high throughput screening [21], and nuclear magnetic resonance (NMR) technique [22,23]. Diffusion coefficients of the charge can be measured through pulsed field gradient NMR spectroscopy but they are lower than

the diffusivities calculated from ionic conductivity through Nernst-Einstein equation due to the failure to capture the Grotthuss mechanism [22,23]. The experimental measurements do not provide direct information regarding the molecular-level interpretation of proton transport mechanism. To understand the connection between the structure and transport, the contribution and behavioral change in the two components of proton diffusion within the highly acidic and confined aqueous domains of the membrane needs to be studied.

Simulation or molecular modeling of proton transport needs to capture the disparate time scales associated with vehicular diffusion (nano scale) and structural diffusion (pico time scale). Modeling techniques like Car–Parinello *ab initio* molecular dynamics (CPAIMD) [13,24], mixed quantum and classical mechanics technique (QM/MM) [25,26], EVB [27] and its family [28,29], mixed MD/MC algorithm [30] and Q–HOP MD [31] made significant contribution towards understanding of proton transport in bulk water and some of them have been extended to study proton transport in PEM [32-34]. Other theoretical methodologies like electronic structure calculations [35], *ab initio* molecular dynamics [36,37] and meta-dynamics [38], and nonequilibrium statistical models [39,40] have also been implemented. Molecular-level modeling of proton transport in perfluorosulfonic acid (PFSA) membranes has been reviewed by Elliott and Paddison [41]. Classical MD simulations [5,8,9] have been used to study proton dynamics but they can only follow the vehicular diffusion since structural diffusion cannot be dictated by classical mechanics. Vehicular diffusion has been studied as a function of polymer chemistry (EW, monomeric sequence), hydration and temperature. Vehicular diffusion increases with water content and temperature [42] but are much lower than experimental values at high $\lambda$ because of the absence of structural diffusion in the models. There is experimental [43] and theoretical evidence [40] that separation of sulfonic acid groups can affect the transport properties and the vehicular component increased with the decrease in EW of the polymer at intermediate and high water content [8]. Q-HOP MD has been used to study the activation energy and mean residence times for proton transfer reaction as a function of hydration and temperature with a single $H_3O^+$ undergoing structural diffusion. The authors have also discussed the effect of water percolation network in Nafion on proton conductivity [34]. A strong anticorrelation between the structural and vehicular component was found by the application of

self-consistent multistate EVB and the effect of sulfonate ion on charge diffusion by acting as traps has been analyzed [32].

This work uses a newly developed reactive molecular dynamics (RMD) algorithm to analyze proton transport in PEM, Nafion. RMD algorithm models the structural diffusion of a proton as a chemical reaction and implements the reactivity through a three step procedure instead of the manipulation of interactive potential or empirical formulations. The algorithm has been initially parameterized for structural diffusion of a proton in bulk water and extended to other systems which have the same TS (Zundel and Eigen cations) involved, including aqueous hydrochloric acid solutions and water confined in carbon nanotubes (CNT) without any modification. This shows the adaptability of the algorithm to different local environments and physical conditions. Structural diffusion of protons in a PEM can take place either along the surface of a hydrophobic/hydrophilic interface or the core of the aqueous domain which has an different environment [44]. To implement the RMD algorithm one must know a priori the chemical reactions of interest. This can be taken as an advantage and disadvantage. The disadvantage is that we need to know all possible reactions taking place and a separate set of parameters is needed for each reaction. The advantage is that in a complex system like a PEM where confinement can dictate the aqueous environment and acidity can define the hydrophobic/hydrophilic interface understanding the individual contribution of reactions occurring in these regions will help us to relate structure to transport property. In the present work we have implemented structural diffusion via the same mechanism used in the studies of bulk water, bulk HCl solutions and water in CNTs.

The paper is organized as follows. The methodology, including a brief description of the RMD algorithm and the details of the simulations are described in Sec. 5.2. Results and discussion are presented in Sec. 5.3 and the findings are summarized in Sec. 5.4. The results obtained from the current simulation can be further improved by small changes in the RMD algorithm and this work is under progress. Section 5.5 discusses the influence of the modification algorithm (specifically local equilibration scheme) on the transport properties of water and hydronium ions in bulk water that would be reflected in PEMs.

## 5.2 SIMULATION METHODOLOGY

### 5.2.1 Reactive Molecular Dynamics Algorithm

RMD algorithm is a generalized algorithm that can represent any chemical reaction via three steps (i) satisfaction of a set of geometric and energetic triggers, (ii) instantaneous reaction, and (iii) local equilibration. The steps involved in the model have been discussed in detail in earlier publications [45,46]. The algorithm takes input from both macroscopic description (stochiometry, rate constant, $k$, activation energy, $E_a$, heat of reaction, $\Delta H_r$) and quantum mechanical (QM) description (transition state (TS), reactant and product structures) of a chemical reaction and reproduces a model that is far more detailed than a macroscopic model and less detailed than the QM model. RMD algorithm is implemented at the end of each classical MD step. Hence RMD simulations use the existing well parameterized nonreactive potentials and the reactivity is incorporated by the three step algorithm.

RMD algorithm models the structural diffusion of a proton in aqueous system as a chemical reaction,

$$H_3O^+ + H_2O \xleftrightarrow{nH_2O} H_2O + H_3O^+ \quad (1)$$

where $n$ is the additional number of water molecules present during the reaction. The first step of the algorithm is to check whether the reactants ($H_3O^+$ and $H_2O$) satisfy a set of geometric and energetic triggers. The energetic trigger ($E_{a,f}$) is identified from the $E_a$ required to overcome the energy barrier for the proton to be moved from one water molecule to the other. The geometric trigger checks whether the reactants are in a favorable configuration for the reaction to take place. The use of nonreactive potentials prevents the molecules from reaching the TS. Therefore for the structural diffusion of proton, six geometric triggers are chosen based on the equilibrium structures of $H_3O^+$, $H_2O$ [47] and the two protonated complexes – Zundel [48] and Eigen [49] cations that play a major role in charge diffusion [12,15]. We also concluded that presence of 4 minimum hydrating molecules ($n$) is necessary for the reaction to take place via RMD algorithm [46]. The six geometric triggers are: (1) $r_{OO,Zundel}$: checks the $O(H_3O^+)$-$O(H_2O)$ separation since the reactants must be close enough to form a Zundel ion, (2) $r_{OH,Equilb}$: checks whether the covalent bond distance between the $O(H_3O^+)$ and the proton to be transferred, H*, exceeds the

equilibrium bond distance, (3) $\theta_{OHO}$ : checks whether the angle formed by the $O(H_3O^+)$, H*, and $O(H_2O)$ is nearly linear similar to that observed in Zundel ion, (4) $\theta_{HOH}$ : checks whether the angles formed by the H*, the O of the $H_2O$, and each of the two H of the $H_2O$ is near the equilibrium H-O-H bond angles of $H_3O^+$ ion since lone pair of electrons in the water should point toward the H*, (5) $r_{OO,Eigen}$ : checks whether the each of the two nonreactive H atoms of reactant $H_3O^+$ ion forms hydrogen bond with $H_2O$ molecule since the reactant $H_3O^+$ ion forms an Eigen ion, and (6) $r_{OO,hyd}$ : checks whether each of the two H atoms of reactant $H_2O$ molecule forms hydrogen bond with $H_2O$ molecule since an Eigen cation is formed around the product $H_3O^+$ ion. These triggers are parameterized to reproduce the macroscopic property of $k$ and $E_a$. In the second step of the algorithm instantaneous reaction takes place where the proton is explicitly transferred from one water molecule to the other by converting the covalent bond between the H* and O of reactant $H_3O^+$ into a hydrogen bond and vice versa with O of reactant $H_2O$. Instantaneous reaction increases the potential energy of the system and disrupts the local hydrogen bonding network. Local equilibration is the final step that relaxes selected molecules to satisfy the target $\Delta H_r$ and re-establish a reasonable hydrogen bonding network. The specific details of the triggers and local equilibration can be found in our previous study conducted [46]. Parameterization of the triggers requires $k$ and $E_a$. Hence the algorithm was first applied to proton transport in bulk water which has the most reliable description from both experiment [50-52] and simulation [31,53]. In addition to the advantages of using the existing nonreactive potentials thereby reducing the development time involved in the parameterization of reactive potentials, which has higher degree of freedom than the triggers involved in step 1 of the algorithm. The methodology for a reaction can be extended from one environment (bulk water [46]) to the other (aqueous HCl [46] solution and water confined in CNTs [54]) as long as they have the same TS structures. The information regarding the TS is embedded within the triggers. Therefore, the algorithm has the benefit of identifying its local environment at least to capture the effect qualitatively.

The sensitivity and adaptability of the algorithm to different environment has been previously tested and proved [46,54]. The pH dependence on the structural diffusion of a proton was investigated by implementing the algorithm to aqueous HCl systems of different

concentrations (0.22 – 0.83 M) [46]. The algorithm qualitatively captured the decrease in structural diffusion with an increase in acidity of the HCl solution. Proton diffusion in water confined in CNTs of varying radii (5.42 – 10.85 Å) was studied to analyze the effect of confinement on structural diffusion [54]. The axial structural component of the total charge diffusion was found to increase with the decrease in confinement. Thus with the aid of the geometric and energetic triggers the model is able to capture the essential features of the structural diffusion of proton irrespective of its surroundings and physical conditions that can affect the energy and solvation structure of the proton. Having analyzed the individual effects of confinement and acidity, the RMD algorithm is applied in this work to study proton transport in PEMs, where both nanoscale confinement and acidity are present.

### 5.2.2 Proton Transport in PEM

We have categorized the structural diffusion of a proton in a PEM into the following three reactions based on the reactants, hydration level and hydrating molecules,

$$H_3O^+ + H_2O \xleftarrow{nH_2O} H_2O + H_3O^+ \quad (2.a)$$

$$H_3O^+ + H_2O \xleftarrow{mH_2O/(n-m)SO_3^-} H_2O + H_3O^+ \quad (2.b)$$

$$SO_3H + H_2O \xleftarrow{nH_2O} SO_3^- + H_3O^+ \quad (2.c)$$

Reaction given by Eq. (2.a) is similar to that of bulk water (Eq. 1) where it is hydrated only by the surrounding water molecules. Equations (2.b and c) may occur along the interface of hydrophobic and hydrophilic regions where the nonreactive H atoms of the reactants can be hydrated by the $O(SO_3^-)$ in addition to water molecules. Shown in Figure 5.1 are the snapshot of few of the possible combinations of the reactants and four hydrating molecules taken from a classical MD simulation. Only Eq. (2.a) will have TS structures of Zundel and Eigen cations similar to that found in bulk water, whereas Eq. (2.b) will have TS structures of "Zundel-like" and "Eigen-like" complexes, in which one or more of the hydrating water molecules are replaced by a sulfonate group. Since the algorithm has been parameterized for the structural diffusion of proton in bulk water only the reaction having the same transition state is modeled in this work. Separate set of triggers and parameter values are required for modeling the other two reactions. RMD simulation of the full set of reactions would enable us to understand the individual

contribution of the each reaction in Eq. (2) to the overall proton conductivity and will provide a better platform to modify the polymer chemistry to enhance or reduce the effect of specific reaction.

### 5.2.3 Computational Details

NVT simulations are performed of Nafion at 300 K for four hydration levels ($\lambda = H_2O/SO_3H$) of 6, 9, 15, 22. Lower hydration level than $\lambda = 6$ is not chosen since we are interested only in the structural diffusion of a proton following the mechanism similar to that observed in bulk aqueous system and finding protons following that mechanism might be difficult at $\lambda < 6$. In the simulations, we have used the same interaction potentials for the polymer electrolyte, water, and hydronium molecules as used earlier in the simulations of the bulk hydrated membrane [8]. Even the initial configurations for the current simulations are obtained from the production runs of the previous work. The equilibration details of the structure are not discussed here. The hydrated membrane simulations from our previous work is referred henceforth as nonreactive system since they were modeled using classical MD simulation and proton transport involved only the vehicular diffusion.

We consider a Nafion polymer with an equivalent weight (EW) of 1144 each consisting of 15 monomers. All the systems at $\lambda = 6$, 9, 15, and 22 have 40 Nafion ionomers, the corresponding 600 $H_3O^+$ ions and 3000, 4800, 8400, 12600 $H_2O$ molecules respectively. The densities are obtained from an empirical function derived from experimental results [55]. The justification of this model and the successful comparison with similar simulations performed has been discussed previously [3,8]. The $CF_X$ in the backbone is represented as an united atom with single Lennard-Jones (LJ) parameter [11,56] and the backbone does not carry any charge. The side chain of Nafion is modeled with parameters defined by Vishnyakov and Neimark [57,58]. The detailed potential model of Nafion and sources for the force constants are reported in our earlier work [8]. Water is modeled using the TIP3P model [47] with a flexible OH bond [59], while the $H_3O^+$ ions uses the same model with modified charges on O and H which is similar to that used by Urata *et al.* [2]. The bonded interactions include stretching, bending, and bond torsion. Lennard-Jones (LJ) and coulombic interactions contribute to non-bonded interactions.

The two time scale r-RESPA [60] approach with a time step of 2.0 fs for the large time step and 0.2 fs for the intramolecular interactions is used for the integration of the equations of motion. The temperature is maintained by the Nose´-Hoover thermostat [61,62]. LJ potentials are cut off at 10 Å. Site-site reaction field method is incorporated to account for electrostatic interactions [63] and long range LJ interactions are taken into account. The total length of the simulations at $\lambda$ = 6, 9, 15, and 22 are 0.86, 0.46, 0.40 and 0.27 ns. It is sufficient to run these simulations for a relatively short time since we are interested only in the dynamics of $H_2O$ and the $H_3O^+$ ion. A newly developed confined random walk (CRW) diffusion model [64] can be used to calculate the diffusivity in long time limit from short MD or RMD runs.

The parameters for the RMD algorithm are the same as that of bulk water, aqueous HCl and water confined in CNTs with a minor modification in the trigger values. We have the same six geometric triggers, one energetic trigger and objective function for the local equilibration. However, we have slightly modified the definition of a reaction in this work. Earlier, a reaction was taken into account for *k* calculation when the $H^+$ rattling between two molecules ended up with either of the parent molecule or another $H_2O$ molecule at the end of rattling. In the current work, we define a reaction taking place only when then the proton ends up with a molecule other than the parent molecule at the end of rattling. In short, only if a $H^+$ undergoes odd number of rattles it is considered as a reaction. Due to this change triggers were reparameterized ($r_{OO,Zundel} : 2.35 - 2.75\,Å$, $r_{OH,Equilb} :\geq 0.965\,Å$, $\theta_{OHO} :\geq 146°$, $\theta_{HOH} : 65 - 143°$, $r_{OO,Eigen} : 2.35 - 2.93\,Å$, $r_{OO,hyd} : 2.50 - 3.27\,Å$, $E_{a,f} :\geq -23.719$ kcal/mol) to match the experimental rate constant. At the end, we got a better agreement of the total charge diffusivity with the experimental value because of the better contribution of the structural component compared to the old definition of reaction. Since the parameterization process, system size, density, potentials and explanation of each trigger is discussed in great detail in the earlier study [46], they are not reported again in this work. However, the fitted *k* and measured transport property are discussed here. Figure 5.2 compares the fitted *k* with the experimental measurements [51]. We find that they are in good agreement with an average relative error of 5%. Total charge diffusivity, structural component and vehicular component along with their corresponding reference values are plotted in Figure 5.3. The total charge diffusivity is compared

to that experimental value [14,65], structural diffusivity is compared to the value estimated from Einstein relation using the average lifetime of proton [12,66] and vehicular diffusivity is compared to the difference between the experimental value and structural component (under the assumption they are uncorrelated). As can be seen from Figure 5.2 the current definition of reaction and new trigger values were able to reproduce the transport property of the charge and its two components with better match to the reference values by fitting to the experimental rate constant.

In Sec. 5.4, to test different local equilibration schemes bulk water simulations at infinite dilute concentration were run. The potential models and system size are the same as the previous work [46]. Since only preliminary runs were needed the properties were calculated from 40 – 48 independent runs containing one $H_3O^+$ ion in 650 molecules. The production runs were 0.5 – 1 ns long.

## 5.3 RESULTS AND DISCUSSION

In this section we mainly concentrate on transport properties of water and hydronium ions since the structural properties like radial distribution function (RDF), density profile, hydration histograms and cluster size distributions have been discussed in detail by the earlier work of classical MD simulations [3,8].

### 5.3.1 Rate Constant

The reactivity in an RMD algorithm is set by the triggers as described above. Therefore, the number of reactions and the transport associated with a reaction are uniquely determined. However, if one wishes to extract a rate constant from the simulation data, one must formulate the expression for a rate constant describing the reaction in Eq. (1). The rate constant for the proton transfer reaction in Nafion of EW1144 given by Eq. (2.a) is calculated using the formula

$$k = \frac{N_{react}}{time \cdot V_{aq}} \times \frac{1}{[H_2O]_{Bulk}[H_3O^+]_{Bulk}} \tag{3}$$

where $[H_2O]_{Bulk}$ and $[H_3O^+]_{Bulk}$ are the concentrations along the bulk-like regions of the aqueous domains, $V_{aq}$ corresponds to aqueous phase volume in the system, $N_{react}$ represents the number of reactions with only odd number of rattles and *time* represents the length of the

simulation. $V_{aq}$ has been reported previously and is calculated using a zero-volume probe molecule approach [8]. There is no clear boundary distinguishing the interfacial and bulk-like regions in the aqueous domains. Using the RDFs of $O(SO_3^-) - O(H_2O)$ and $O(SO_3^-) - O(H_3O^+)$ with the cut-off distances of 3.2 and 2.9 Å respectively (corresponding to first peak) the interfacial volume of $H_2O$ and $H_3O^+$ ions is calculated using the definition,

$$\text{Interfacial Volume} = \text{Volume of cut - off distance} \times \text{No. of } SO_3^- \times \text{Overlap factor} \quad (4)$$

Here the overlap factor is taken as 3 assuming the O atoms are far apart in the $SO_3$ group. Thus by subtracting the interfacial volume from total aqueous volume, the bulk volumes of $H_2O$ and $H_3O^+$ ions can be obtained. The volume balance in the aqueous domains is explained using Table 5.1. Both volume and mass balances are required for the calculation of $[H_2O]_{Bulk}$ and $[H_3O^+]_{Bulk}$. The number of $H_2O$ and $H_3O^+$ ions per $O(SO_3^-)$ group can be calculated from the radial distribution functions and the number of $H_2O$ and $H_3O^+$ ions along the interface is given as follows:

$$\text{Molecules at Interface} = \text{No. of molecules/}SO_3^- \times \text{No. of } SO_3^- \times \text{Overlap factor} \quad (5)$$

Similar to volume balance the mass balance can be generated and are reported in Table 5.2. The overlap factor is once again taken as 3. Table 5.3 lists the concentrations at the interface and bulk-like regions calculated using Tables 5.1 and 5.2. There is a steady increase in $[H_2O]$ in all the three regions with an increase in the water content of Nafion. Whereas, as λ increases $[H_3O^+]$ decreases. Figure 5.4 shows *k* calculated using these values as a function of λ. The rate constant increases with water content which is consistent with the increase in number of $H_3O^+$ ions in bulk-like environment with increase in λ. Even at λ=22, *k* at 300 K is 10 times lower than that of bulk water ($k$ = 10.708 × $10^9$ L/(mol·s) [51]). The decrease in rate constant has been observed in aqueous HCl system and carbon nanotubes with increase in acidity and confinement respectively. So in a PEM where both confinement and acidity play vital roles similar trend is observed.

The concept of having geometric and energetic triggers satisfied for the occurrence of a reaction in the RMD algorithm helps us to identify the triggers that promote the increase in *k* with λ. In bulk HCl solutions, we observed that the energetic trigger (and not any of the six

geometric triggers) provided both the most severe limitation, preventing 99.9% of $H_3O^+$ ions from reacting, as well as the most sensitive to changes in acidity. In the RMD simulations of water in CNTs, we found an analogous result, namely that the single energetic trigger was the most limiting and the most sensitive to changes in confinement. In PEMs, the same result is once again observed. The energetic trigger is most sensitive to changes in water content, reflecting changes in both acidity and confinement. The fraction satisfying each trigger discussed in Sec. 5.2.1 is shown in Figure 5.5 for all the water contents. Each fraction is calculated based on the satisfaction of earlier triggers and that is why only six triggers are presented in the plot. The hierarchy of the trigger is based on the manner they were tested in the code and was chosen for computational efficiency.

The reactivity of the structural diffusion can also be measured in terms of lifetime of proton, $\tau_P$. And the *k* for a first order of reaction of structural diffusion of proton is $1/\tau_P$. The $\tau_P$ for bulk water at 300 K is around 1.7 ps [51]. Devanathan *et al.* applied Q-HOP MD to study proton transport in a system of four Nafion polymers each with 10 side chains. They allowed structural diffusion of a single proton while the rest of them were allowed to diffuse only through vehicular mechanism. At λ = 5, 10, and 15 they measured the mean $\tau_P$ of the proton to be 250, 6.6, 2.9 ps respectively. We have considered the structural diffusion of proton as second order reaction and hence $\tau_P = 1/(k[H_2O]_{Bulk})$. The $\tau_P$ for λ= 6, 9, 15, and 22 is calculated as 310.8, 86.7, 40.3 and 23 ps respectively. An order of magnitude difference between the two systems at highest and lowest water content might be due to the fact we are considering the diffusion of proton following only Eq. (2.a).

### 5.3.2 Water Diffusivity

Diffusion of protons and water in the aqueous domains of a PEM undergoes non-linear time dependent confined diffusion initially, and then they follow Einstein's linear relation in the infinite time limit. The water diffusion coefficient in a nonreactive system can be unambiguously calculated using Einstein expression,

$$D = \lim_{\tau \to \infty} \frac{\left\langle [r(t+\tau) - r(t)]^2 \right\rangle}{2d\tau} \tag{6}$$

where *d* is the dimensionality of the system, τ is the observation time and $\left\langle \left[ r(t+\tau) - r(t) \right]^2 \right\rangle$ is the mean square displacement (MSD). In a reactive system since the molecules undergo change in identity whenever the reaction takes the diffusivity is measured in the time segments in which they did not react. The production run of nonreactive system by Liu *et al.* [8] was run 2 ns long, which is sufficient for the structural data analysis but was found insufficient for the diffusion coefficient calculation. The exponent, *m*, in $\text{MSD} \propto \tau^m$, falls in the sub-diffusive range of 0.69 – 0.85 for λ = 3 – 22. Recently, we have developed and implemented a CRW simulation approach [64] that can extend the short-time MSD data for diffusion in the presence of nanoscale confinement obtained from MD simulation to statistically reliable MSDs for longer time limit. Therefore, instead of running the simulation longer than 2 ns for sole purpose of MSD data collection a simple confined random walk (CRW) simulation can be integrated with classical MD simulation of short time scale to get diffusivities in the long time limit where *m* is 1 – MD/CRW algorithm. The computational expense added to the classical MD simulation by the RMD algorithm can be overcome by CRW approach too. Currently we have not applied the CRW simulation to obtain the diffusivities in the long time limit. The MD/CRW algorithm applied to nonreactive system did not affect the diffusivities significantly since *m* was in the range of 0.69 – 0.85 [64]. The reactive system though was run for a shorter time than the nonreactive has *m* in the range of 0.60 – 0.95.

Water diffusivity in nonreactive system [8], reactive system and experimentally measured [17] values are shown in Figure 5.6 as a function of water content. We find the water diffusivities in all three systems to increase with the hydration level. TIP3P water model [47] inherently has higher diffusivity value than experimentally measured bulk water value [67,68]. Therefore, water diffusivity in the nonreactive system is higher than experimental value at all λ but qualitatively follows the same trend. Implementation of the RMD algorithm is not expected to affect the water diffusivity in a reactive system from that of a nonreactive system. However, in the current reactive system the water diffusivity is found to be nearly 4.25 times higher than the nonreactive system at the highest water content. This increase can be attributed to the improper local equilibration which seems to be insufficient in a complex system like Nafion unlike the simple system of bulk water for which triggers were parameterized. The proof for lowering the

water diffusivity in a reactive system to match the nonreactive system by improving the local equilibration scheme is discussed later.

### 5.3.3 Charge Diffusion

One of the features of the RMD algorithm is that one can be specific about the chemical reactions that take place in a system. Only the structural diffusion of a proton having the same TS as that of bulk water is included in this work. So the total charge diffusion measured is a combination of vehicular component and structural diffusion contributed only by the reaction given by Eq. (2.a.) The total charge diffusion can be measured using the Einstein's relation in Eq. (6) by following the trajectory of the center of mass position of $H_3O^+$ ion. To decouple the individual contributions of the vehicular and structural component to the total charge diffusion, the total displacement of the $H_3O^+$ ion in each step can written as [32]

$$\Delta\vec{r}_{\text{tot}} = \Delta\vec{r}_{\text{veh}} + \Delta\vec{r}_{\text{struct}} \tag{7}$$

where $\Delta\vec{r}_{\text{veh}}$, is the displacement due to vehicular diffusion or in other words correspond to the displacement due to classical MD simulation and $\Delta\vec{r}_{\text{struct}}$, is the structural component Displacement. Whenever there is no reaction $\Delta\vec{r}_{\text{struct}} = 0$ and $\Delta\vec{r}_{\text{veh}}$ becomes the sole contributor to $\Delta\vec{r}_{\text{tot}}$. When a reaction takes place in a particular MD step $\Delta\vec{r}_{\text{struct}}$ is approximately equal to 2.55 – 2.65 Å which is the distance between $O(H_3O^+)$–$O(H_2O)$ and $\Delta\vec{r}_{\text{tot}}$ is the sum of both $\Delta\vec{r}_{\text{veh}}$ and $\Delta\vec{r}_{\text{struct}}$. Therefore the trajectory of $\vec{r}_{\text{veh}}$ is continuous and $\vec{r}_{\text{struct}}$ is discontinuous. By substituting Eq. (7) in Eq. (6), total charge diffusivity, $D_{\text{tot}}$, can be rewritten as

$$D_{\text{tot}} = \lim_{\tau\to\infty} \frac{\left\langle \Delta\vec{r}_{\text{veh}}^{\,2} \right\rangle + \left\langle \Delta\vec{r}_{\text{struct}}^{\,2} \right\rangle + 2\left\langle \Delta\vec{r}_{\text{veh}} \Delta\vec{r}_{\text{struct}} \right\rangle}{2d\tau} \tag{8}$$

The above definition can be decomposed as,

$$D_{\text{veh}} \equiv \lim_{\tau\to\infty} \frac{\left\langle \Delta\vec{r}_{\text{veh}}^{\,2} \right\rangle}{2d\tau} \tag{9.a}$$

$$D_{\text{struct}} \equiv \lim_{\tau\to\infty} \frac{\left\langle \Delta\vec{r}_{\text{struct}}^{\,2} \right\rangle}{2d\tau} \tag{9.b}$$

$$D_{\text{corr}} \equiv \lim_{\tau\to\infty} \frac{2\left\langle \Delta\vec{r}_{\text{veh}} \Delta\vec{r}_{\text{struct}} \right\rangle}{2d\tau} \tag{9.c}$$

where $D_{\text{veh}}$ and $D_{\text{struct}}$ are vehicular and structural diffusion coefficients respectively. $D_{\text{corr}}$ is the correlation term that denotes the coupling between the structural and vehicular contributions. The discussion on $D_{\text{corr}}$ is provided later in the paper.

Figure 5.7 shows the experimental charge diffusivities [17,69], $H_3O^+$ ion diffusivities from the nonreactive system of Liu *et al.* [8], and $D_{\text{tot}}$ from the reactive system along with $D_{\text{veh}}$ and $D_{\text{struct}}$ as a function of water content. Experimentally the charge diffusivity is found to increase with water content and the same trend is followed by all the diffusivities shown in the figure. Addition of RMD algorithm was found to have no effect on the vehicular diffusion of $H_3O^+$ ions in the past. Both in bulk water [46] and water confined in CNTs [54] the vehicular component of the charge diffusion was almost equal to the $H_3O^+$ ion diffusivities from the nonreactive system. In the application to PEMs, the vehicular diffusion coefficients are higher than the diffusivities in the nonreactive system for the same reason of finding increase in the water diffusivities of a reactive system from that of a nonreactive system which is due the insufficient relaxation of the molecules during local equilibration and is discussed in Sec. 5.4. Corresponding to the increase in rate constant with λ, $D_{\text{struct}}$ increases with the hydration level. $D_{\text{tot}}$ is higher than the experimentally observed values because the $D_{\text{veh}}$ is too high. For now we are satisfied with qualitative agreement between $D_{\text{tot}}$ and experimental values because we expect $D_{\text{veh}}$ to lower with an improved local equilibration scheme which in turn would result in a better quantitative agreement between simulation and experiment.

### 5.3.4 Correlation

The correlation between the structural and vehicular components of the total charge diffusion can be obtained from the $D_{\text{corr}}$ term in Eq. (9.c). $D_{\text{corr}}$ is calculated from the relation

$$D_{\text{corr}} = D_{\text{tot}} - \left(D_{\text{veh}} + D_{\text{struct}}\right) \tag{10}$$

If $D_{\text{corr}} = 0$, then both the components of the total charge diffusion are uncorrelated. Proton transport in the previously studied system like bulk water [46], aqueous HCl and water confined

in CNTs[54] exhibited uncorrelation between the two components of $D_{tot}$. MS-EVB2 has also observed negligible negative correlation of the two components in bulk water [32]. Figure 5.8 plots the $D_{corr}/D_{tot}$ as a function of hydration level. The plot shows a decrease in $D_{corr}/D_{tot}$ with λ implying they are anti-correlated at low water contents and at high water content as they approach bulk water behavior their anti-correlation diminishes. *Petersen et al.* [32] observed similar strong anticorrelation between the two components in Nafion at λ = 15 and quantified the time scale of these correlated motions as 425 ps using the distinct portion of the van Hove correlation function.

Understanding the anti-correlation between the two components can not be done with direct decoupling. Hence, we formulated two functions to study the correlation between the $O(H_3O^+)$ and almost stationary point in the system like $S(SO_3^-)$ for the structural ($f_{struct}$) and vehicular components ($f_{veh}$). After every reaction we identify the $S^*(SO_3^-)$ that is closest to the product $O(H_3O^+)$. $f_{struct}$ is calculated as

$$f_{struct} = \left(\vec{r}_{O(H_3O^+)_{pdt}} - \vec{r}_{S^*(SO_3^-)}\right) - \left(\vec{r}_{O(H_2O)_{pdt}} - \vec{r}_{S^*(SO_3^-)}\right) \quad (11)$$

where $\vec{r}$ is the position vector of the corresponding molecule. When $f_{struct}$ is less than zero it means the reaction is bringing the $H_3O^+$ ion closer to the sulfonic group and when $f_{struct}$ is greater than zero it implies the product $H_3O^+$ ion is moving towards the sulfonic group. $f_{struct}$ averaged over all reactions is plotted as a function of λ in Figure 5.9. We find the $f_{struct}$ to approach zero from a negative value implying the tendency of the reaction to bring the $H_3O^+$ ion closer to the hydrophobic/hydrophilic interface reduces or the cluster size is big enough to avoid the effect of sulfonate ions. It is to be kept in mind the numbers in the plot are not supposed to be taken quantitatively but qualitatively since they represent the overall effect of numerous reactions and tend to have high standard deviations. Moreover we are taking a reference point that is unique to each $H_3O^+$ ion at every reaction and might depend on the aqueous domain size that varies with λ. Since the two components are anti-correlated if the structural diffusion tends to bring the $H_3O^+$ ion closer to the sulfonic group then the vehicular diffusion has to move the

$H_3O^+$ ion away from the sulfonic group. The above phenomenon can be tested by measuring $f_{veh}$ as function of time, where

$$f_{veh}(t) = X(t) - X(0), \left[ X(t) = \left| \vec{r}_{O(H_3O^+)_{pdt}} - \vec{r}_{S^*(SO_3^-)} \right|_t \right] \quad (12)$$

In other words $f_{veh}$ tracks the trajectory of the $H_3O^+$ ion relative to $S^*(SO_3^-)$. If $f_{veh}(t)$ is negative then $H_3O^+$ ion is moving towards the sulfonic group and if $f_{veh}(t)$ is positive then $H_3O^+$ ion is moving away from the sulfonic group. Figure 5.10 shows the $f_{veh}$ as function of time at different λ. $f_{veh}$ is averaged over the trajectories of all $H_3O^+$ ions after each reaction and is calculated for a time period of 1000 fs or shorter if they undergo another reaction within the specified timeframe. From the plot we can see that as λ increases the magnitude of $f_{veh}$ increases and are always positive. Combining the results shown in Figures 5.9 and 5.10 we can confirm that the structural diffusion brings the $H_3O^+$ ion closer to the sulfonic group while vehicular diffusion moves in the opposite direction. Though the decrease in anti-correlation can not be described quantitatively by the above formulations, they at least explain the reason behind the negative coupling of $D_{veh}$ and $D_{struct}$. A similar conclusion was deduced by *Petersen et al.* [32] from the distinct portion of the van Hove space-time correlation for the hydronium-sulfonate ion pair where they observed the fluctuating bond topology resetting the hydronium ion back to a position relative to the sulfonate ion preventing it from diffusing away as $H_3O^+$ ion.

## 5.4 METHODS OF LOCAL EQUILIBRATION

The RMD algorithm allows a reaction to take place whenever a set of geometric and energetic triggers are satisfied. The instantaneous reaction involves change in identity of the molecules (potentials and charges), movement of proton and breaking of bonds that cannot be captured by the classical MD simulation. Therefore, a reaction is always accompanied by the change in potential energy of the system and disturbance to the complex 3-D hydrogen bonding network. For example, the O–O RDF for $H_2O$–$H_2O$ is different than that for $H_3O^+$–$H_2O$. The first peak in the O($H_2O$)–O($H_2O$) RDF is at 2.8 Å, whereas the first peak in the O($H_3O^+$)–O($H_2O$) is at 2.55 Å in bulk water. Since we know the heat of reaction, $\Delta H_r$, for the structural diffusion of a

proton and local structure from the RDF, a local equilibration scheme can be devised to restore the equilibrium structure and satisfy the target $\Delta H_r$. For this purpose, we have identified an objective function, $F_{obj}$, that has an energetic and geometric component as follows:

$$F_{obj} = w_1 \Delta g(r)^{RMS} + w_2 \Delta U^{RMS} \tag{13}$$

The energetic component, $\Delta U^{RMS}$, is the root mean square (RMS) error of the energy difference of the system before ($U_{before}$) and after ($U_{after}$) the reaction (since $\Delta H_r$=0),

$$\Delta U^{RMS} = \sqrt{\left( \frac{U_{after} - U_{before}}{U_{before}} \right)^2} \tag{14}$$

The structural component, $\Delta g(r)^{RMS}$, is the RMS error of the current distance ($r_{ij}$) between two atoms, *i* and *j* and the expected distance ($r_{ij}^{target}$) from the RDF and can be described as,

$$\Delta g(r)^{RMS} = \sqrt{\frac{1}{N_{pairs}} \sum_{j=1}^{j=N_{pairs}} \left( \frac{r_{ij} - r_{ij}^{target}}{r_{ij}^{target}} \right)^2} \tag{15}$$

where $N_{pairs}$ refers to the number of pairs of atom considered. The satisfaction of energy or structural component is distributed by the weighting factors, $w_1$ and $w_2$. There are many variables that need to be defined in $F_{obj}$: (1) selection of molecules to be relaxed, (2) identification of the structural points ($N_{pairs}$), and (3) specification of $w_1$ and $w_2$. Therefore, it is possible to approach the execution of local equilibration in numerous ways. One way to confirm the selection of scheme for the structural diffusion of a proton is to compare the water diffusivities in a reactive and nonreactive system (where protons are not allowed to hop) or pure water (TIP3P model). Experimentally, the self-diffusion coefficient of water is not affected by protons at dilute concentrations [70]. Hence the addition of the RMD algorithm should not alter the water diffusivities in a reactive system from that of a nonreactive system.

The structural diffusion of a proton in bulk systems and in CNTs was modeled with a local equilibration that relaxed the four hydrating molecules and $H^+$ transferred with $N_{pairs}$=12, $w_1$ = 1 and $w_2$ = 10. The restructuring of hydrogen bonds in the solvation shell around the excess charge with the transfer of $H^+$ has been observed by *ab initio* studies [15,71]. Therefore, we

decided to relax the four hydrating molecules and with preliminary short runs chose the other parameters in $F_{obj}$ by trial and error until a reasonable water diffusivity was obtained. The chosen local equilibration method seemed sufficient in a simple system of bulk water at infinite dilute concentration and proved efficient in aqueous HCl and water confined in CNTs. But when moved to complex system of PEM (Nafion) which has both confinement and acidity the current choice of the scheme failed as can be seen from the results discussed above. We can confirm our theory of poor local equilibration causing increase in diffusion coefficients by trying other local equilibrations methods and showing a decrease in water diffusivities in a reactive Nafion system.

In this section, the various possible local equilibration schemes are discussed. First they are tested on bulk water system and then applied to Nafion to prove they are efficient in both systems. We tried to improve the local equilibration in two ways: (1) Improving the structural component by increasing $N_{pairs}$ and number of molecules relaxed and (2) Improving the energetic component by increasing $w_2$. The above two approaches be denoted as Trials 1 and 2 respectively. The discussion highlights the significant results to draw a conclusion and proceed in the right direction.

In Trial 1, the final configuration of the products and surrounding molecules are improved by increasing $N_{pairs}$ to include more details of the solvation structure and relaxing more number of molecules to equilibrate the structure better. The high concentration of $H_3O^+$ ions in confined aqueous regions of PEM sometime places a $H_3O^+$ ion next to another ion after the reaction. Therefore, in order to have an environment in PEM similar to that of bulk water we decided to check hydration by six hydrating molecules instead of four hydrating molecules from the initial assessment. In other words, we check for the existence fourth coordinating $H_2O$ molecule. This can also be conceived as inclusion of two more geometric triggers. A typical structure of the reactants surrounded by six hydrating molecules in bulk water is shown in Figure 5.11. Each molecule and atom in Figure 5.11 are labeled for future reference. Table 5.4 lists the method number, molecules relaxed, the total degree of freedom, *N*, (number of atoms relaxed × dimensionality) and $N_{pairs}$. In order to make the description of each method easier, pictorial notation has been used. An empty triangle beneath a molecule number indicates the molecule is relaxed to minimize the $F_{obj}$ and a solid triangle denotes a molecule that has not been moved. In

certain cases an atom label is placed either next to a solid or empty triangle. This means, except for the specified atom, the rest of the atoms in the molecule follow the code of the triangle. The table shows that a number of approaches have been tried with $N$ and $N_{\text{pairs}}$ ranging from 3 – 72 and 12 – 26 respectively. A list of maximum $N_{\text{pairs}}$ are given in Table 5.5. The $r_{ij}^{\text{target}}$ values are obtained from the RDF between the atoms $i$ and $j$ from classical MD simulation discussed in our previous paper [46]. These values not only concentrate on first solvation shell but also on the second solvation shell. The methods are not individually described since they can be clearly understood from the table. For example, Method 1 which is the original method implemented in bulk water has empty triangle under molecule numbers III – VI and have solid triangles for other molecules except for molecule I which also has the atom label $H_5$ specified. The interpretation of the row corresponding to Method 1 is that four hydrating molecules and the proton transferred are relaxed while the rest of the molecules are kept stationary. We implemented these methods at three temperatures (280, 300, 320 K) in bulk water and their $k$ and water diffusivity are reported in Figure 5.12 and 5.13 respectively. The trigger values in each method were not particularly parameterized to match the experimental $k$ [51], but were chosen to yield reasonable $k$ as can be seen from Figure 5.12. We are satisfied with the approximation since we wanted to confirm the applicability of the method before going into the entire parameterization process. For this purpose we compared the water diffusivity from the reactive system to the pure water simulation of TIP3P model [46]. Irrespective of the large number of data in close range, Figure 5.13 shows that except for Method 1 all the other methods increased the water diffusivity in bulk water. Clearly, this is not the right direction to proceed for improving local equilibration. So we decided to pick Method 1 (scheme that is efficient in bulk water) and Method 10 (which has the highest $N$ and $N_{\text{pairs}}$) and implement Trial 2.

The importance of the energy term in the objective function minimized during local equilibration can be increased by increasing the corresponding weighting factor, $w_2$. After some preliminary runs we chose $w_2 = 100$ for Method 1 (Run 1) and $w_2 = 500$ for Method 10 (Run 2) in contrast to $w_2 = 10$ in Trial 1. Runs 1 and 2 were simulated at 300 K for bulk water at infinite dilute concentration. Figure 5.14 and 5.15 shows the rate constant and water diffusivity in Method 1, Method 10, Run 1 and Run 2 compared with the same reference values discussed in

Trial 1. Additionally we also applied Run 1 and Run 2 to Nafion at λ = 9 and 22 to test validity of the scheme in Nafion before investing further time in parameterization. The MSD of the water are plotted as a function of time for a nonreactive system, Method 1, Run 1 and Run 2 for λ = 9 and 22 in Figure 5.16 and 5.17 respectively. This appears to be a promising line of approach. Though the water diffusivities in a reactive bulk water and Nafion system are not an exact match to that of nonreactive system, we have significantly improved the MSD of water in a reactive system of Nafion.

We included the above description and analysis of various local equilibration schemes in order to point out that we understand the reason behind the quantitative disagreement between the simulation and experimental/estimated results and to prove the existence of ways to improve the results discussed in Sec. 5.3. Generally, implementation of the new local equilibration methods involves the following steps: (1) Define the parameters in $F_{\text{obj}}$, (2) Apply the method to bulk water system and confirm the water diffusivity is not affected, (3) Reparameterize the triggers to match the experimental $k$ and $E_{\text{a,f}}$, (4) Apply the method to PEM. As a conclusion of this section we have completed first two steps. Future work involves reparameterization and application of the new local equilibration scheme for modeling proton transport in Nafion.

## 5.5 CONCLUSIONS

Proton diffusion in Nafion occurs through a combination of both vehicular and structural diffusion mechanisms. We have differentiated the reactions involved in structural diffusion based on their hydration level and TS. In this work, the RMD algorithm is applied to model the structural diffusion of protons in Nafion (EW = 1144) that share the same TS as in bulk water at λ = 6, 9, 15, and 22 at 300 K. The algorithm partitions the structural diffusion of protons into threes steps: (i) trigger satisfaction (ii) instantaneous reaction (iii) local equilibration. The algorithm makes the reaction sensitive to its environment by embedding the information of the TS, geometric and energetic constraints within the triggers. The algorithm that had been parameterized for structural diffusion of proton in bulk water and extended to aqueous HCl and water confined in CNTs to study the independent effect of acidity and confinement, respectively

is now implemented without any modifications to model structural diffusion of proton within the aqueous regions of the membrane where both the above mentioned effects play a vital role.

This work mainly focuses on dynamics of water, proton transport and the correlated motion described by the structural and vehicular component of the charge diffusion. The rate constant for the structural diffusion of proton increased with water content. The triggers that slowed the reaction rate at lower water contents were the energetic trigger and geometric trigger that checked the hydration of reactant water molecule by two water molecules. Water diffusivities increased with the hydration level but were higher than the values from nonreactive system due to the insufficient relaxation of the molecules in the last step of the RMD algorithm. The contribution and correlation between the structural and vehicular component to the total charge diffusion were analyzed. The two components were found to be negatively correlated with their anticorrelation decreasing with increase in $\lambda$. Two simple functions were formulated with the $S(SO_3^-)$ as reference point to describe the anticorrelation. From the functions it was proved that as the vehicular diffusion tried to move the $H_3O^+$ ion away from the sulfonate group, the structural diffusion moved the $H_3O^+$ ion towards the sulfonate group. The total charge diffusivity was found to be higher than the experimental values at all water content. Though the dynamic properties of water and charge did not have a quantitative agreement with their reference values they qualitatively followed the same trend. Local equilibration scheme with greater importance to energetic component than the structural term of the objective function most likely seems to improve the results.

## 5.6 ACKNOWLEDGEMENT

This research project is supported by the U. S. Department of Energy's (DOE) Office of Basic Energy Sciences program (grant number DE-FG02-05ER15723). This work benefited from the resources of the Center for Computational Sciences at Oak Ridge National Laboratory, which is supported by the Office of Science of the DOE under contract DE-AC05-00OR22725.

# References

[1] Costamagna, P. and Srinivasan, S., *J. Power Sources* **102**, 253 (2001).

[2] Urata, S.; Irisawa, J.; Takada, A.; Shinoda, W.; Tsuzuki, S. and Mikami, M., *J. Phys. Chem. B* **109**, 4269 (2005).

[3] Cui, S. T.; Liu, J. W.; Esai Selvan, M.; Keffer, D. J.; Edwards, B. J. and Steele, W. V., *J. Phys. Chem. B* **111**, 2208 (2007).

[4] Fujimura, M.; Hashimoto, T. and Kawai, H., *Macromolecules* **14**, 1309 (1981).

[5] Devanathan, R.; Venkatnathan, A. and Dupuis, M., *J. Phys. Chem. B* **111**, 8069 (2007).

[6] Hristov, I. H.; Paddison, S. J. and Paul, R., *J. Phys. Chem. B* **112**, 2937 (2008).

[7] Kreuer, K. D., *J. Membr. Sci.* **185**, 29 (2001).

[8] Liu, J. W.; Suraweera, N.; Keffer, D. J.; Cui, S. T. and Paddison, S. J., *J. Phys. Chem. C* **114**, 11279 (2010).

[9] Jang, S. S.; Molinero, V.; Cagin, T. and Goddard, W. A., *J. Phys. Chem. B* **108**, 3149 (2004).

[10] Kreuer, K. D., *ChemPhysChem* **3**, 771 (2002).

[11] Li, Q. F.; He, R. H.; Jensen, J. O. and Bjerrum, N. J., *Chem. Mater.* **15**, 4896 (2003).

[12] Agmon, N., *Chem. Phys. Lett.* **244**, 456 (1995).

[13] Tuckerman, M.; Laasonen, K.; Sprik, M. and Parrinello, M., *J. Chem. Phys.* **103**, 150 (1995).

[14] Robison, R. A. and Stokes, R. H., *Electrolyte Solutions*, Butterworths, London (1959).

[15] Markovitch, O.; Chen, H.; Izvekov, S.; Paesani, F.; Voth, G. A. and Agmon, N., *J. Phys. Chem. B* **112**, 9456 (2008).

[16] Zawodzinski, T. A.; Springer, T. E.; Davey, J.; Jestel, R.; Lopez, C.; Valerio, J. and Gottesfeld, S., *J. Electrochem. Soc.* **140**, 1981 (1993).

[17] Kreuer, K. D., *Solid State Ionics* **97**, 1 (1997).

[18] Petersen, M. K.; Wang, F.; Blake, N. P.; Metiu, H. and Voth, G. A., *J. Phys. Chem. B* **109**, 3727 (2005).

[19] Lee, C. H.; Park, H. B.; Lee, Y. M. and Lee, R. D., *Ind. Eng. Chem. Res.* **44**, 7617 (2005).

[20] Slade, S.; Campbell, S. A.; Ralph, T. R. and Walsh, F. C., *J. Electrochem. Soc.* **149**, A1556 (2002).

[21] Ivanovskaya, A.; Fan, J.; Wudl, F. and Stucky, G. D., *J. Membr. Sci.* **330**, 326 (2009).

[22] Zawodzinski, T. A.; Neeman, M.; Sillerud, L. O. and Gottesfeld, S., *J. Phys. Chem.* **95**, 6040 (1991).

[23] Ochi, S.; Kamishima, O.; Mizusaki, J. and Kawamura, J., *Solid State Ionics* **180**, 580 (2009).

[24] Car, R. and Parrinello, M., *Phys. Rev. Lett.* **55**, 2471 (1985).

[25] Billeter, S. R. and van Gunsteren, W. F., *J. Phys. Chem. A* **102**, 4669 (1998).

[26] Intharathep, P.; Tongraar, A. and Sagarik, K., *J. Comput. Chem.* **27**, 1723 (2006).

[27] Warshel, A. and Weiss, R. M., *J. Am. Chem. Soc.* **102**, 6218 (1980).

[28] Schmitt, U. W. and Voth, G. A., *J. Chem. Phys.* **111**, 9361 (1999).

[29] Wu, Y. J.; Chen, H. N.; Wang, F.; Paesani, F. and Voth, G. A., *J. Phys. Chem. B* **112**, 467 (2008).

[30] Schmidt, R. G. and Brickmann, J., *Ber. Bunsen-Ges. Phys. Chem. Chem. Phys.* **101**, 1816 (1997).

[31] Lill, M. A. and Helms, V., *J. Chem. Phys.* **115**, 7993 (2001).

[32] Petersen, M. K. and Voth, G. A., *J. Phys. Chem. B* **110**, 18594 (2006).

[33] Seeliger, D.; Hartnig, C. and Spohr, E., *Electrochim. Acta* **50**, 4234 (2005).

[34] Devanathan, R.; Venkatnathan, A.; Rousseau, R.; Dupuis, M.; Frigato, T.; Gu, W. and Helms, V., *J. Chem. Phys. B* **114**, 13681 (2010).

[35] Paddison, S. J., *J. New Mater. for Electrochem. Syst.* **4**, 197 (2001).

[36] Roudgar, A.; Narasimachary, S. P. and Eikerling, M., *Chem. Phys. Lett.* **457**, 337 (2008).

[37] Choe, Y. K.; Tsuchida, E.; Ikeshoji, T.; Yamakawa, S. and Hyodo, S., *Phys. Chem. Chem. Phys.* **11**, 3892 (2009).

[38] Glezakou, V. A.; Dupuis, M. and Mundy, C. J., *Phys. Chem. Chem. Phys.* **9**, 5752 (2007).

[39] Eikerling, M.; Kornyshev, A. A.; Kuznetsov, A. M.; Ulstrup, J. and Walbran, S., *J. Phys. Chem. B* **105**, 3646 (2001).

[40] Paddison, S. J.; Paul, R. and Zawodzinski, T. A., *J. Chem. Phys.* **115**, 7753 (2001).

[41] Elliott, J. A. and Paddison, S. J., *Phys. Chem. Chem. Phys.* **9**, 2602 (2007).

[42] Venkatnathan, A.; Devanathan, R. and Dupuis, M., *J. Phys. Chem. B* **111**, 7234 (2007).

[43] Xu, H.; Kunz, H. R.; Bonville, L. J. and Fenton, J. M., *J. Electrochem. Soc.* **154**, B271 (2007).

[44] Perrin, J. C.; Lyonnard, S. and Volino, F., *J. Phys. Chem. C* **111**, 3393 (2007).

[45] Jiang, B. W.; Selvan, M. E.; Keffer, D. J. and Edwards, B. J., *J. Phys. Chem. B* **113**, 13670 (2009).

[46] Esai Selvan, M.; Keffer, D. J.; Cui, S. T. and Paddison, S. J., *J. Phys. Chem. C* **114**, 11965 (2010).

[47] Jorgensen, W. L.; J. Chandrasekhar, J.; Madura, J. D.; Impey, R. W. and Klein, M. L., *J. Chem. Phys.* **79**, 926 (1983).

[48] Zundel, G. and Metzger, H., *Z. Phys. Chem.* **58**, 225 (1968).

[49] Wicke, E.; Eigen, M. and Ackermann, T., *Z. Phys. Chem.* **1**, 340 (1954).

[50] Loewenstein, A. and Szoke, A., *J. Am. Chem. Soc.* **84**, 1151 (1962).

[51] Luz, Z. and Meiboom, S., *J. Am. Chem. Soc.* **86**, 4768 (1964).

[52] Glick, R. E. and Tewari, K. C., *J. Chem. Phys.* **44**, 546 (1966).

[53] Lapid, H.; Agmon, N.; Petersen, M. K. and Voth, G. A., *J. Chem. Phys.* **122**, (2005).

[54] Esai Selvan, M.; Keffer, D. J.; Cui, S. and Paddison, S. J., *Mol. Sim.* **36**, 568 (2010).

[55] Weber, A. Z. and Newman, J., *Chem. Rev.* **104**, 4679 (2004).

[56] Cui, S. T.; Siepmann, J. I.; Cochran, H. D. and Cummings, P. T., *Fluid Phase Equilib.* **146**, 51 (1998).

[57] Vishnyakov, A. and Neimark, A. V., *J. Phys. Chem. B* **105**, 9586 (2001).

[58] Vishnyakov, A. and Neimark, A. V., *J. Phys. Chem. B* **105**, 7830 (2001).

[59] Neria, E.; Fischer, S. and Karplus, M., *J. Chem. Phys.* **105**, 1902 (1996).

[60] Tuckerman, M.; Berne, B. J. and Martyna, G. J., *J. Chem. Phys.* **97**, 1990 (1992).

[61] Nosé, S., *Mol. Phys.* **52**, 255 (1984).

[62] Nosé, S., *J. Chem. Phys.* **81**, 511 (1984).

[63] Hummer, G.; Soumpasis, D. M. and Neumann, M., *Mol. Phys.* **77**, 769 (1992).

[64] Calvo-Munoz, E.; Esai Selvan, M.; Xiong, R.; Ojha, M.; Keffer, D. J.; Nicoloson, D. M. and Egami, T., *Phys. Rev. E* **under review**, (2010).

[65] Cornish, B. D. and Speedy, R. J., *J. Phys. Chem.* **88**, 1888 (1984).

[66] Meiboom, S., *J. Chem. Phys.* **34**, 375 (1961).

[67] Mahoney, M. W. and Jorgensen, W. L., *J. Chem. Phys.* **114**, 363 (2001).

[68] Markovitch, O. and Agmon, N., *J. Chem. Phys.* **129**, 084505 (2008).

[69] Kreuer, K. D.; Paddison, S. J.; Spohr, E. and Schuster, M., *Chem. Rev.* **104**, 4637 (2004).

[70] McCall, D. W. and Douglass, D. C., *J. Phys. Chem.* **69**, 2001 (1965).

[71] Tuckerman, M.; Laasonen, K.; Sprik, M. and Parinello, M., *J. Phys. Chem.* **99**, 5749 (1995).

# Appendix F

## Tables and Figures

**Table 5.1.** Volume balance of $H_2O$ molecules and $H_3O^+$ ions in the aqueous domains of Nafion (EW 1144) [a]

| λ | Total Volume[b] | Cut-off distance[c] between O($SO_3$) - *X* | | Interfacial Volume | | Bulk Volume | |
|---|---|---|---|---|---|---|---|
| | | O($H_2O$) | O($H_3O^+$) | $H_2O$ | $H_3O^+$ | $H_2O$ | $H_3O^+$ |
| 6 | 3.07 | 3.2 | 2.9 | 2.47 | 1.84 | 0.60 | 1.23 |
| 9 | 3.61 | 3.2 | 2.9 | 2.47 | 1.84 | 1.14 | 1.77 |
| 15 | 4.69 | 3.2 | 2.9 | 2.47 | 1.84 | 2.22 | 2.85 |
| 22 | 5.95 | 3.2 | 2.9 | 2.47 | 1.84 | 3.48 | 4.11 |

[a] All the volumes are expressed in $10^5$ Å$^3$. Distances are measured in Å. [b] Aqueous volume reported from Ref. 8, [c] Cut-off distances obtained from first peak of RDF.

**Table 5.2.** Mass balance of $H_2O$ molecules and $H_3O^+$ ions in the aqueous domains of Nafion (EW 1144) [a]

| λ | Total | | | Interface | | | | Bulk | |
|---|---|---|---|---|---|---|---|---|---|
| | $SO_3^-$ | $H_2O$ | $H_3O^+$ | $H_2O/O(SO_3^-)$ | $H_3O^+/O(SO_3^-)$ | $H_2O$ | $H_3O^+$ | $H_2O$ | $H_3O^+$ |
| 6 | 600 | 3000 | 600 | 1.481 | 0.128 | 2666.6 | 230.0 | 333.4 | 370.0 |
| 9 | 600 | 4800 | 600 | 1.627 | 0.064 | 2928.9 | 115.2 | 1871.1 | 484.8 |
| 15 | 600 | 8400 | 600 | 1.675 | 0.043 | 3015.6 | 76.9 | 5384.4 | 523.1 |
| 22 | 600 | 12600 | 600 | 1.708 | 0.033 | 3074.9 | 59.6 | 9525.1 | 540.4 |

[a] Number of $H_2O/O(SO_3^-)$ and $H_3O^+/O(SO_3^-)$ is calculated by integrating the area under the RDFs of $O(SO_3^-)-O(H_2O)$ and $O(SO_3^-)-O(H_3O^+)$ with the cut-off distances of 3.2 and 2.9 Å.

**Table 5.3.** Concentration of $H_2O$ molecules and $H_3O^+$ ions along the aqueous domains of Nafion (EW 1144) [a]

| λ | Total Concentration | | Interface Concentration | | Bulk Concentration | |
|---|---|---|---|---|---|---|
| | $H_2O$ | $H_3O^+$ | $H_2O$ | $H_3O^+$ | $H_2O$ | $H_3O^+$ |
| 6 | 9.77E-03 | 1.95E-03 | 1.08E-02 | 1.25E-03 | 5.56E-03 | 3.01E-03 |
| 9 | 1.33E-02 | 1.66E-03 | 1.19E-02 | 6.27E-04 | 1.64E-02 | 2.74E-03 |
| 15 | 1.79E-02 | 1.28E-03 | 1.22E-02 | 4.18E-04 | 2.43E-02 | 1.84E-03 |
| 22 | 2.12E-02 | 1.01E-03 | 1.24E-02 | 3.24E-04 | 2.74E-02 | 1.32E-03 |

[a] All the concentrations are expressed in molecule/$Å^3$.

**Table 5.4.** Description of the methods analyzed in Trial 1[a]

| Method | Molecule Number | | | | | | | | $N$ | $N_{\text{pairs}}$ |
|---|---|---|---|---|---|---|---|---|---|---|
| | I | II | III | IV | V | VI | VII | VIII | | |
| 1 | ▲ $H_5$ | ▲ | Δ | Δ | Δ | Δ | ▲ | ▲ | 39 | 11 |
| 2 | Δ | Δ | Δ | Δ | Δ | Δ | ▲ | ▲ | 57 | 20 |
| 3 | Δ $O_1$ | Δ $O_2$ | Δ | Δ | Δ | Δ | ▲ | ▲ | 51 | 19 |
| 4 | Δ $O_1$ | Δ $O_2$ | Δ | Δ | Δ | Δ | Δ | ▲ | 60 | 19 |
| 5 | ▲ $H_5$ | ▲ | Δ | Δ | Δ | Δ | Δ | ▲ | 48 | 17 |
| 6 | ▲ $H_5$ | ▲ | ▲ | ▲ | ▲ | ▲ | ▲ | ▲ | 3 | 19 |
| 7 | Δ $O_1$ | Δ $O_2$ | Δ | Δ | Δ | Δ | Δ | Δ | 69 | 19 |
| 8 | ▲ $H_5$ | Δ | Δ | Δ | Δ | Δ | Δ | Δ | 66 | 19 |
| 9 | Δ $O_1$ | Δ | Δ | Δ | Δ | Δ | Δ | Δ | 72 | 20 |
| 10 | Δ $O_1$ | Δ | Δ | Δ | Δ | Δ | Δ | Δ | 72 | 26 |

[a] Molecule labels are described in Figure 5.11. $N$ represents the degree of freedom of the $F_{\text{obj}}$. $N_{\text{pairs}}$ is the number of the structural points used to characterize the final configuration of products and hydrating molecules. ▲ – Molecule is kept stationary, Δ - Molecule is moved.

**Table 5.5.** Values of $r_{ij}^{target}$ used in Eq. (13) obtained from RDF between atoms *i* and *j*[a]

| $N_{pairs}$ | $i-j$ | $r_{ij}^{target}$ (Å) | $N_{pairs}$ | $i-j$ | $r_{ij}^{target}$ (Å) |
|---|---|---|---|---|---|
| 1 | $O_3-O_2$ | 2.80 | 14 | $O_6-O_2$ | 3.75 |
| 2 | $O_4-O_2$ | 2.80 | 15 | $H_4-O_2$ | 2.85 |
| 3 | $O_5-O_1$ | 2.55 | 16 | $H_3-O_2$ | 2.85 |
| 4 | $O_6-O_1$ | 2.55 | 17 | $H_4-O_5$ | 2.85 |
| 5 | $O_1-O_2$ | 2.55 | 18 | $H_5-O_5$ | 2.85 |
| 6 | $O_3-H_1$ | 1.85 | 19 | $H_3-O_6$ | 2.85 |
| 7 | $O_4-H_2$ | 1.85 | 20 | $H_5-O_6$ | 2.85 |
| 8 | $O_5-H_3$ | 1.60 | 21 | $O_1-O_8$ | 3.30 |
| 9 | $O_6-H_4$ | 1.60 | 22 | $O_2-O_7$ | 2.80 |
| 10 | $O_3-O_1$ | 4.90 | 23 | $H_5-O_3$ | 4.10 |
| 11 | $O_4-O_1$ | 4.90 | 24 | $H_5-O_4$ | 4.10 |
| 12 | $H_5-O_2$ | 1.60 | 25 | $H_5-O_7$ | 4.10 |
| 13 | $O_5-O_2$ | 3.75 | 26 | $O_2-H_6$ | 1.90 |

[a] All the distances are measured in Å. The labels appear in Figure 5.11.

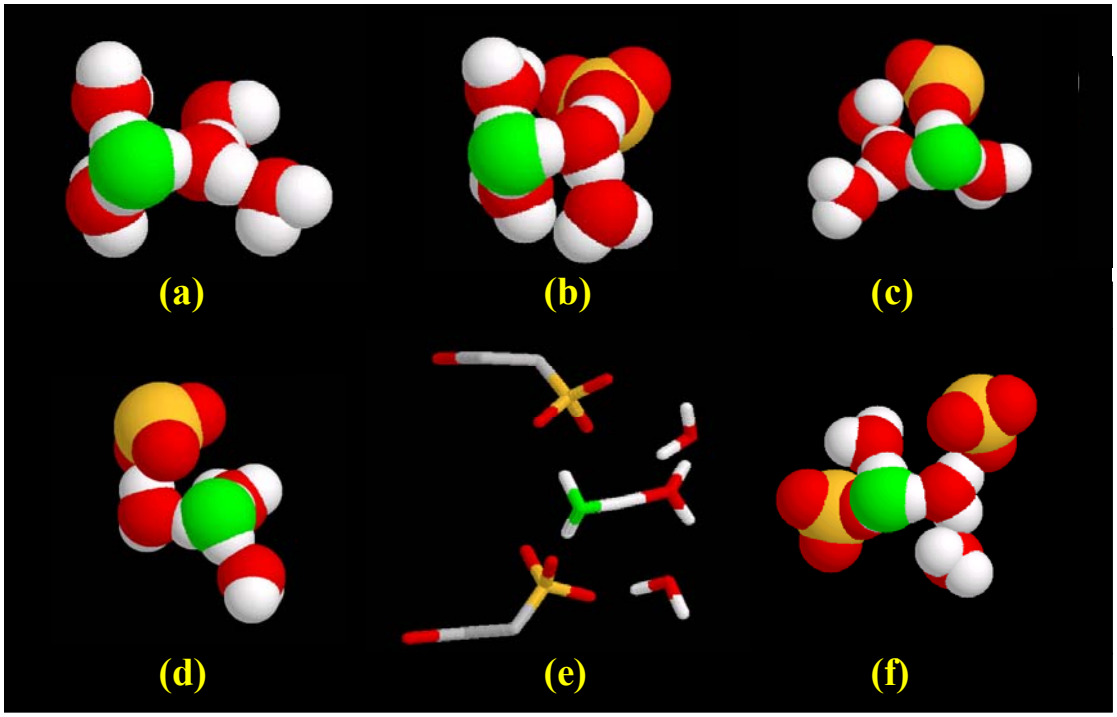


**Figure 5.1.** Snapshot of the reactant $H_3O^+$ ion and $H_2O$ molecule hydrated by various possible combinations of $H_2O$ molecules and $O(SO_3^-)$: **(a)** both reactants $H_2O$ and $H_3O^+$ ion hydrated by two $H_2O$ molecules, **(b)** reactant $H_2O$ hydrated by $H_2O$ and $O(SO_3^-)$ while $H_3O^+$ ion is hydrated by two $H_2O$ molecules, **(c)** reactant $H_2O$ hydrated by two $H_2O$ molecules while $H_3O^+$ ion is hydrated by $H_2O$ and $O(SO_3^-)$, **(d)** reactant $H_2O$ hydrated by two $O(SO_3^-)$ while $H_3O^+$ ion is hydrated by two $H_2O$ molecules **(e)** reactant $H_2O$ hydrated by two $H_2O$ molecules while $H_3O^+$ ion is hydrated by two $O(SO_3^-)$, and **(f)** both reactants $H_2O$ and $H_3O^+$ ion hydrated by $H_2O$ and $O(SO_3^-)$. O of $H_3O^+$, green; O of $H_2O/SO_3^-$, red; H, white; $CF_x$ of side chain, gray; S of $SO_3^-$, orange.

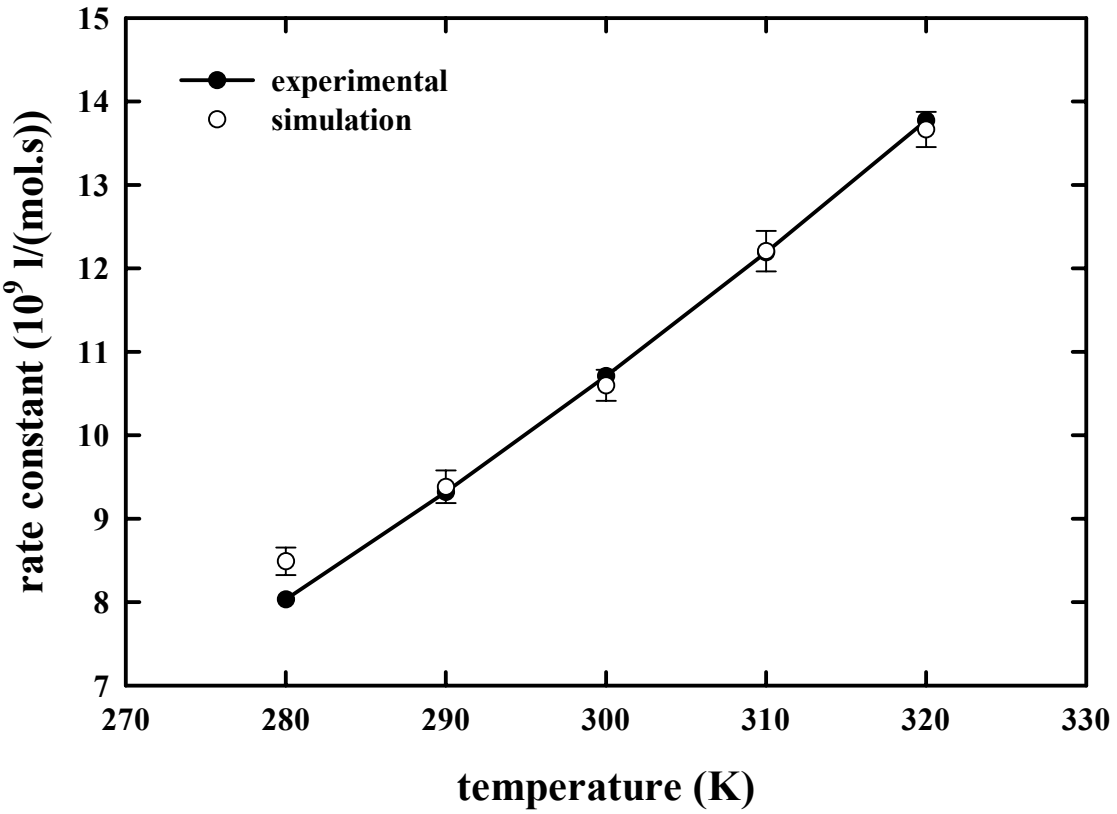


**Figure 5.2.** Fitting of the rate constant to experimental value for the new set of triggers that counts the occurrence of reaction only when there are odd number of rattles.

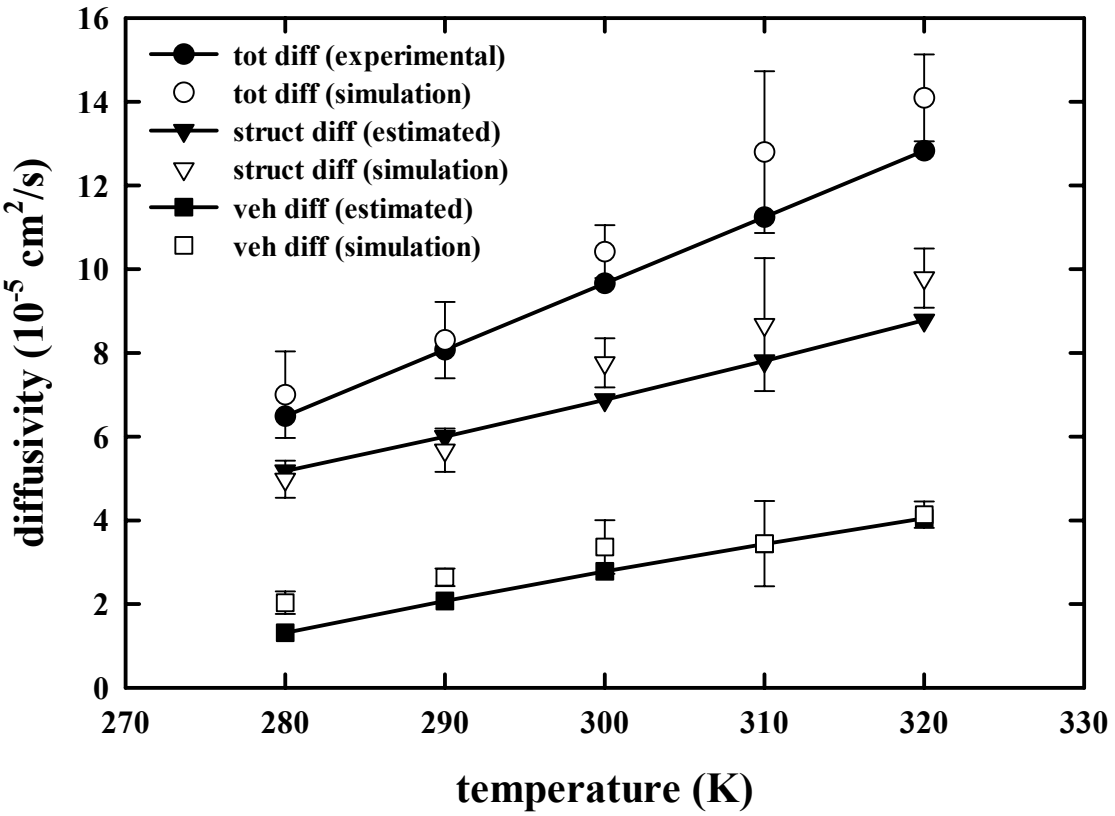


**Figure 5.3.** Charge diffusivity and it two components (vehicular and structural) as a function of temperature compared to the reference values. Solid symbols represent reference values and empty symbols correspond to simulation values. Details of the reference values can be found in the text.

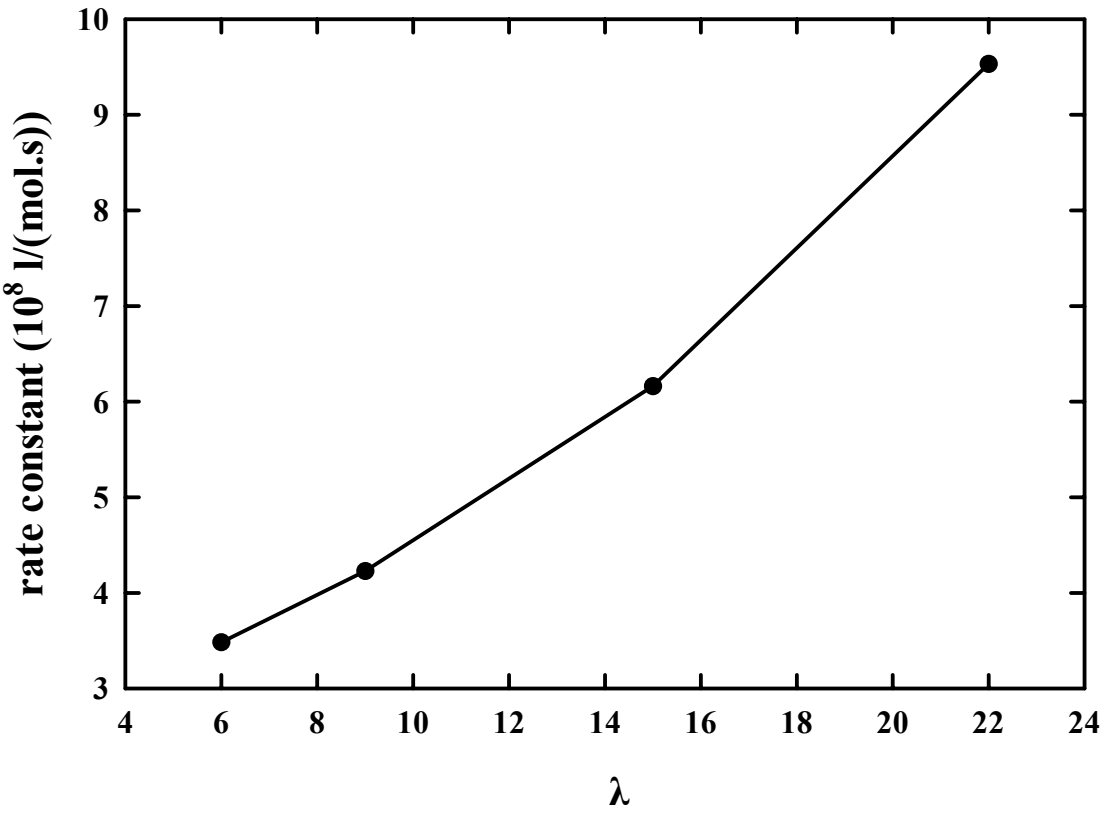


**Figure 5.4.** Rate constant, *k*, of the proton transfer reaction given by Eq. (2.a) in the aqueous domain (calculated using Eq. (3)) as a function of water content.

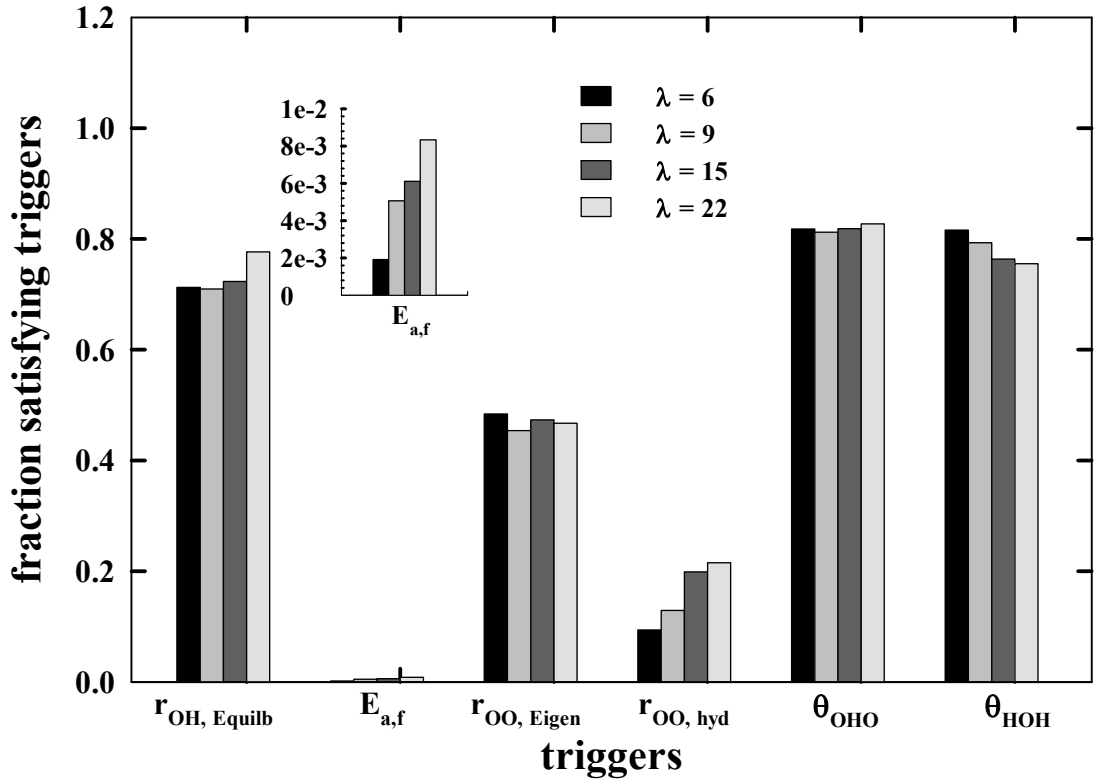


**Figure 5.5.** Histogram of the fraction satisfying the geometric and energetic triggers at various hydration levels in Nafion. Each fraction is calculated based on the satisfaction of the previous trigger. Description of the triggers can be found in Sec. 5.2.1.

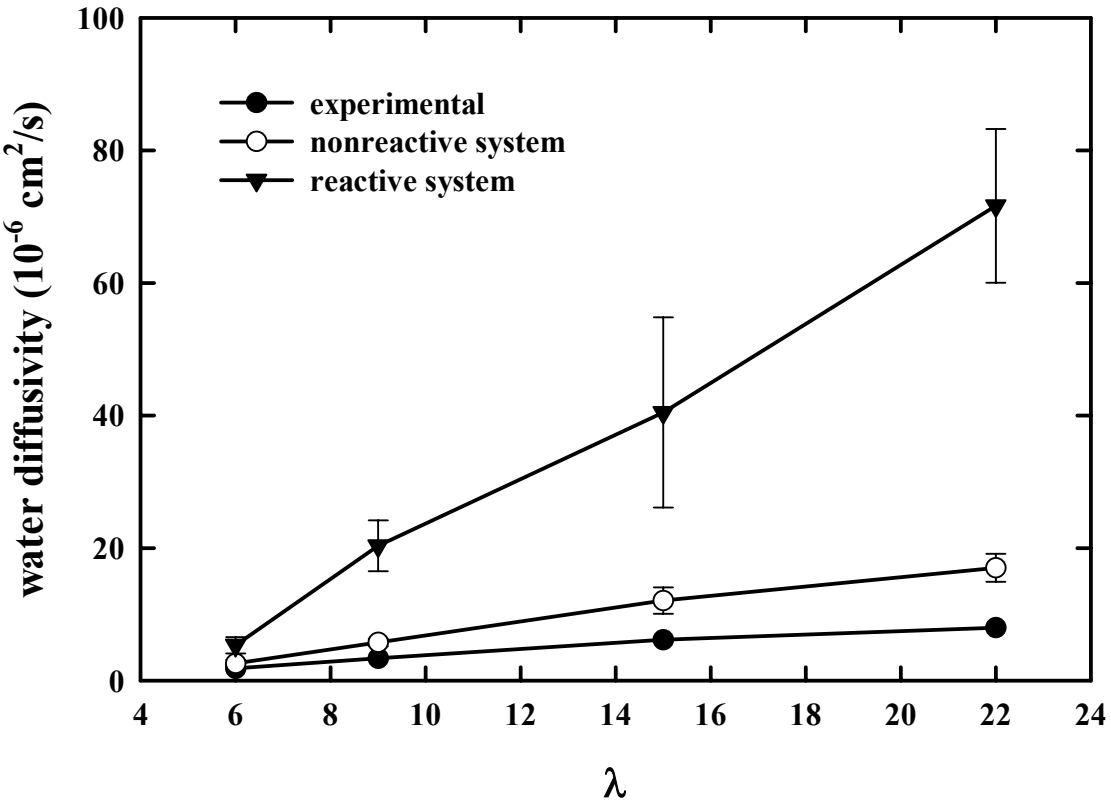


**Figure 5.6.** Comparison of diffusion coefficients of water from experimental, nonreactive and reactive systems at different hydration levels. The water diffusivity in nonreactive system is expected to be equal to that of reactive system.

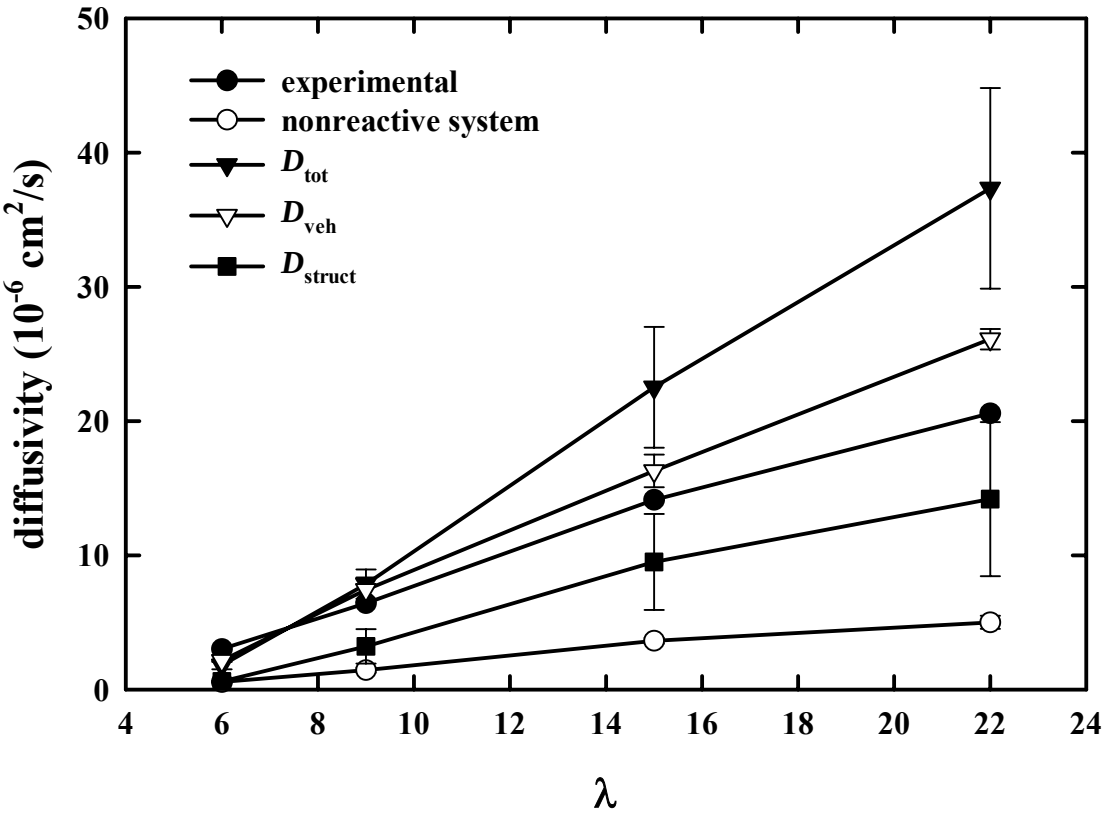


**Figure 5.7.** Charge diffusivity from experimental conductivity (Refs. 17 and 69), classical $H_3O^+$ ion diffusivity in a nonreactive system (Ref. 8), total charge diffusivity, $D_{tot}$, in a reactive system and its (i) vehicular component, $D_{veh}$, and (ii) structural component, $D_{struct}$, as a function of hydration level.

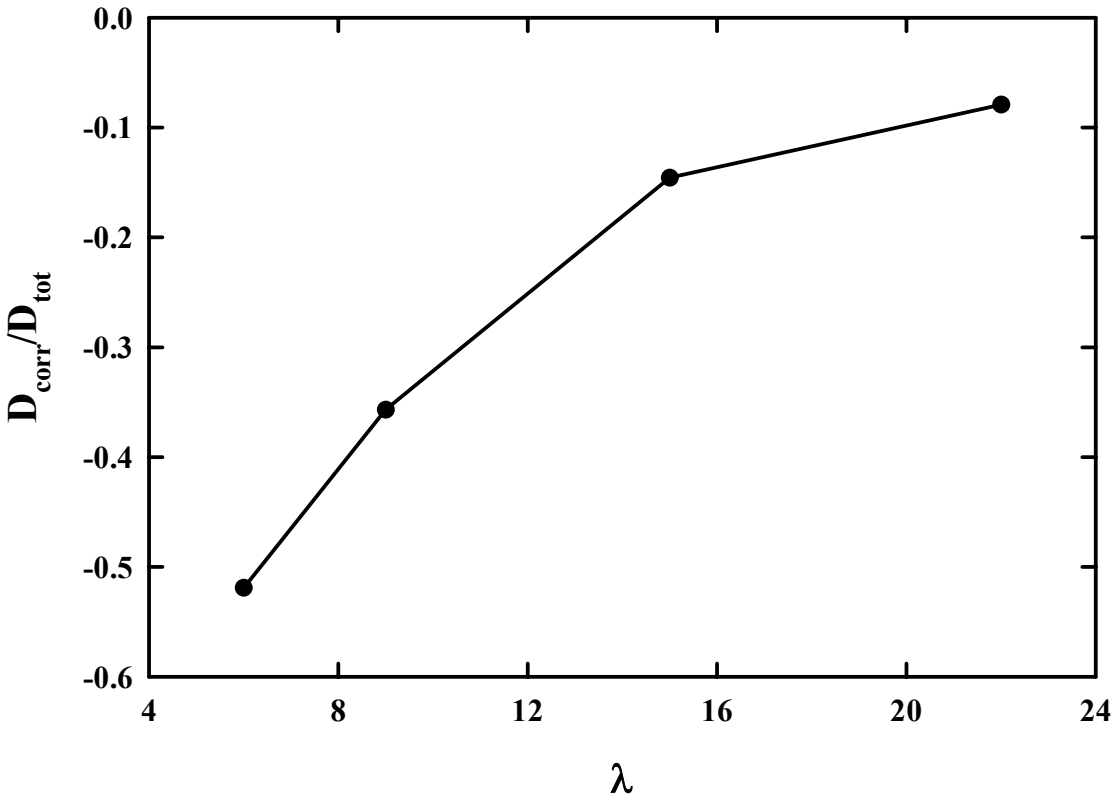


**Figure 5.8.** $D_{\text{corr}}/D_{\text{tot}}$ as a function of water content. If $D_{\text{corr}} = 0$, the structural and vehicular components are uncorrelated. Negative values indicate both components are anti-correlated.

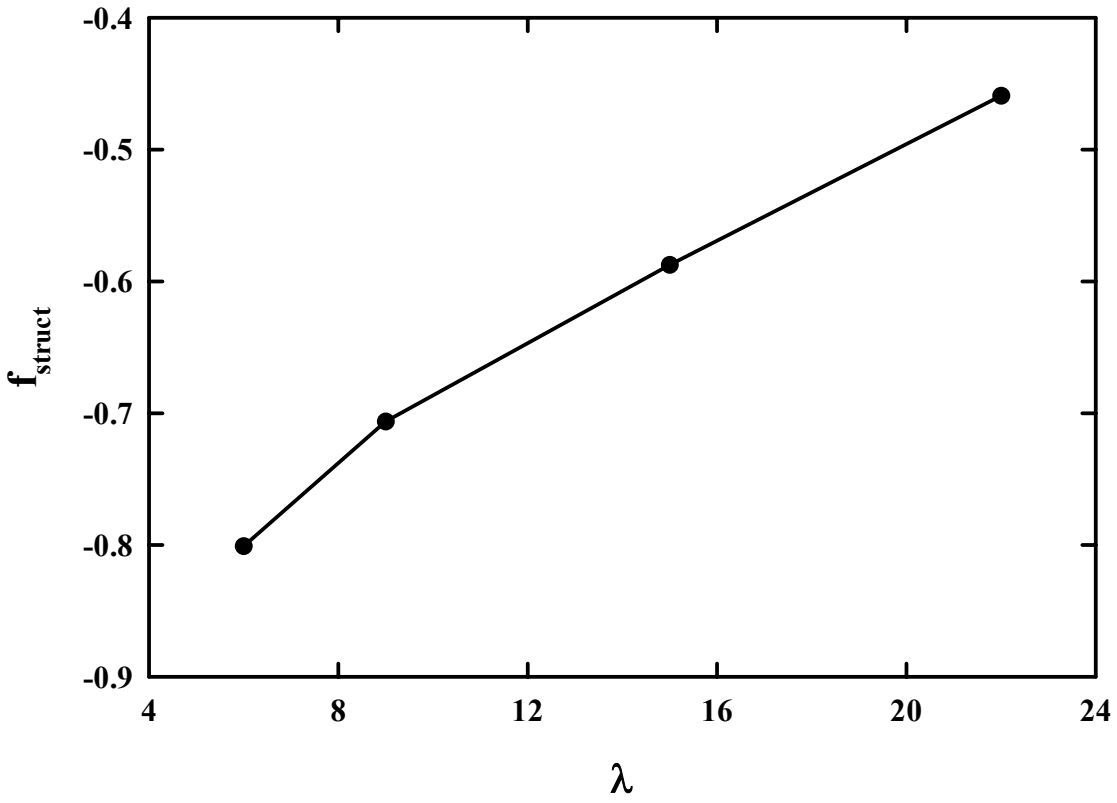


**Figure 5.9.** $f_{\text{struct}}$ as a function of hydration level. $f_{\text{struct}}$ measures the difference in position of the product $H_3O^+$ ion and $H_2O$ molecule relative to the S of the closest sulfonic group. If $f_{\text{struct}} < 0$ then $H_3O^+$ ion is moving towards $SO_3^-$ and if $f_{\text{struct}} > 0$ then $H_3O^+$ ion is moving away from $SO_3^-$ group.

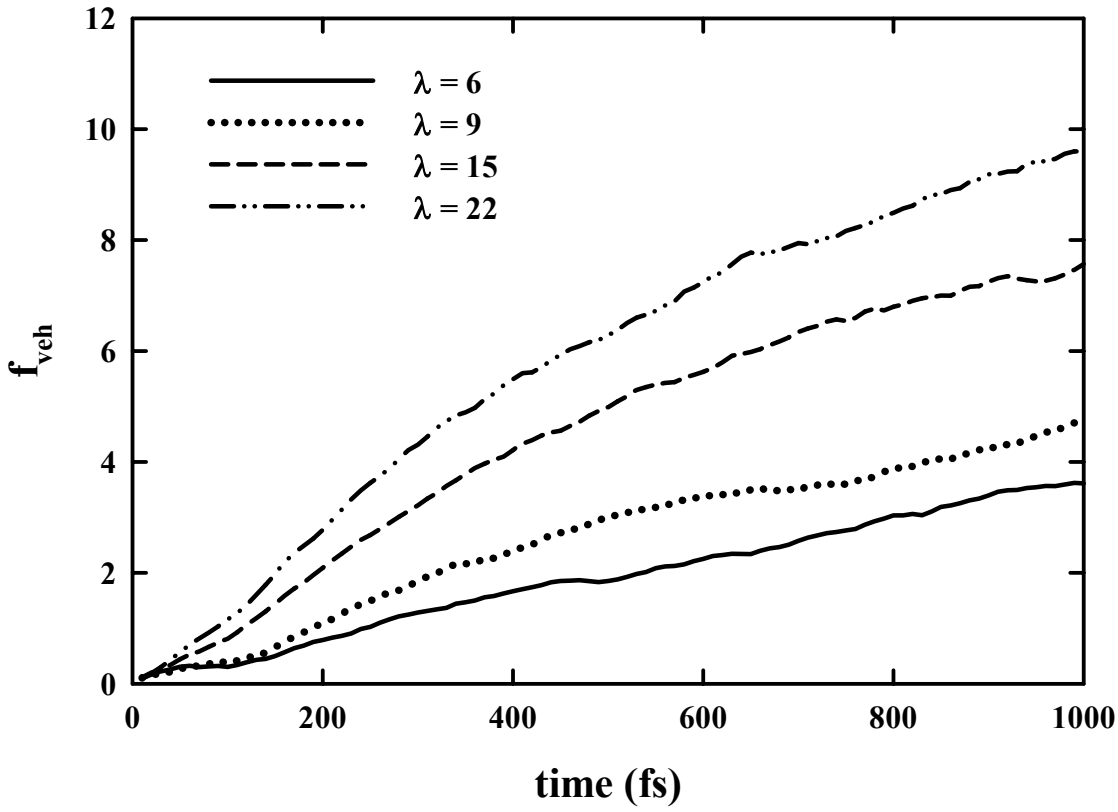


**Figure 5.10.** $f_{\text{veh}}$ as a function of hydration level. If $f_{\text{veh}} < 0$ then $H_3O^+$ ion is moving towards $SO_3^-$ and if $f_{\text{veh}} > 0$ then $H_3O^+$ ion is moving away from $SO_3^-$ group.

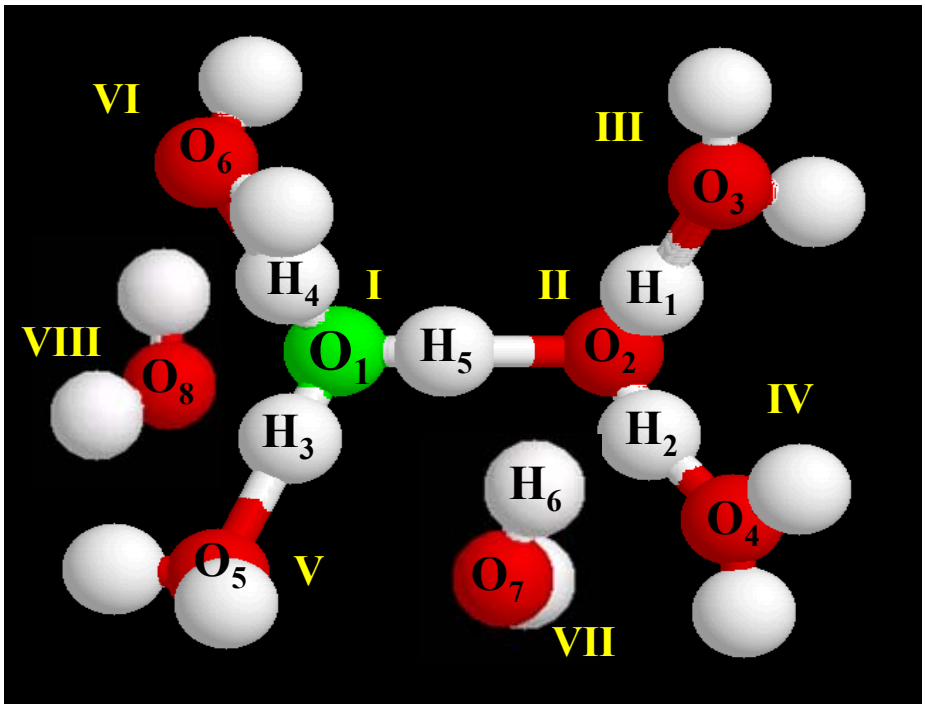


**Figure 5.11.** Typical structure of the reactants surrounded by six hydrating molecules in bulk water system. Atom and molecule labels serve for identification purpose in Tables 5.4 and 5.5. O of $H_3O^+$, green; O of $H_2O$, red; H, white.

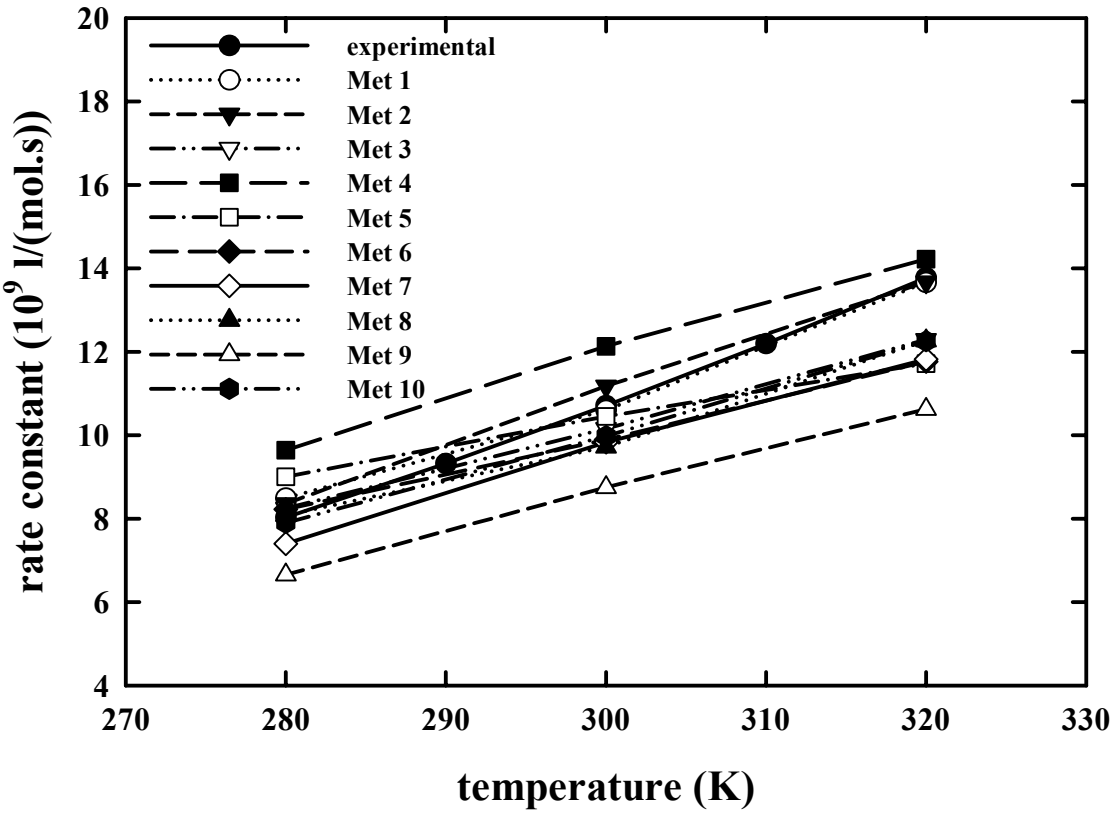


**Figure 5.12.** Rate constant, *k*, for the structural diffusion of a proton in bulk water as a function of temperature for the different methods in Trial 1 listed in Table 5.4. Experimental results are from Ref. 51. Triggers in each method have been modified to give reasonable *k* compared to experimental values.

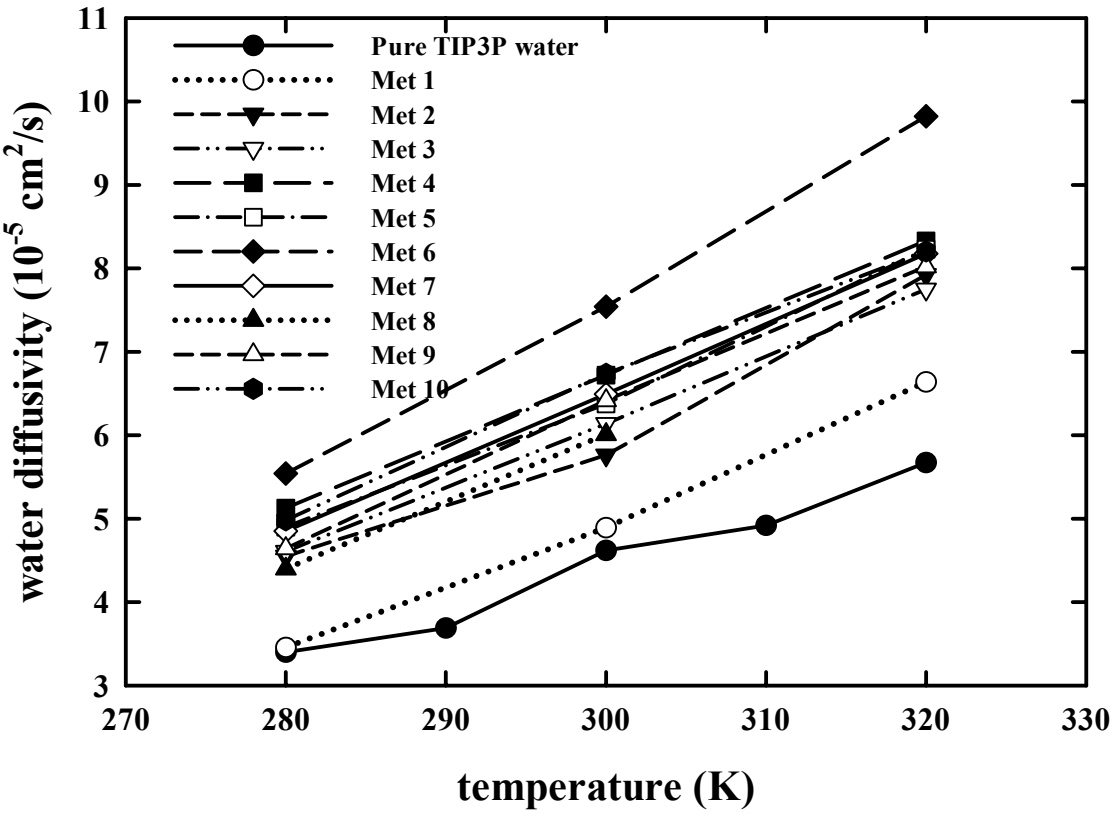


**Figure 5.13.** Water diffusivities in bulk water system at infinite dilute concentration as a function of temperature using different local equilibration schemes listed in Table 5.4. Pure water simulation using the TIP3P model is used as reference (Ref. 46). Method 1 is the only scheme that has the diffusivity closer to the reference value.

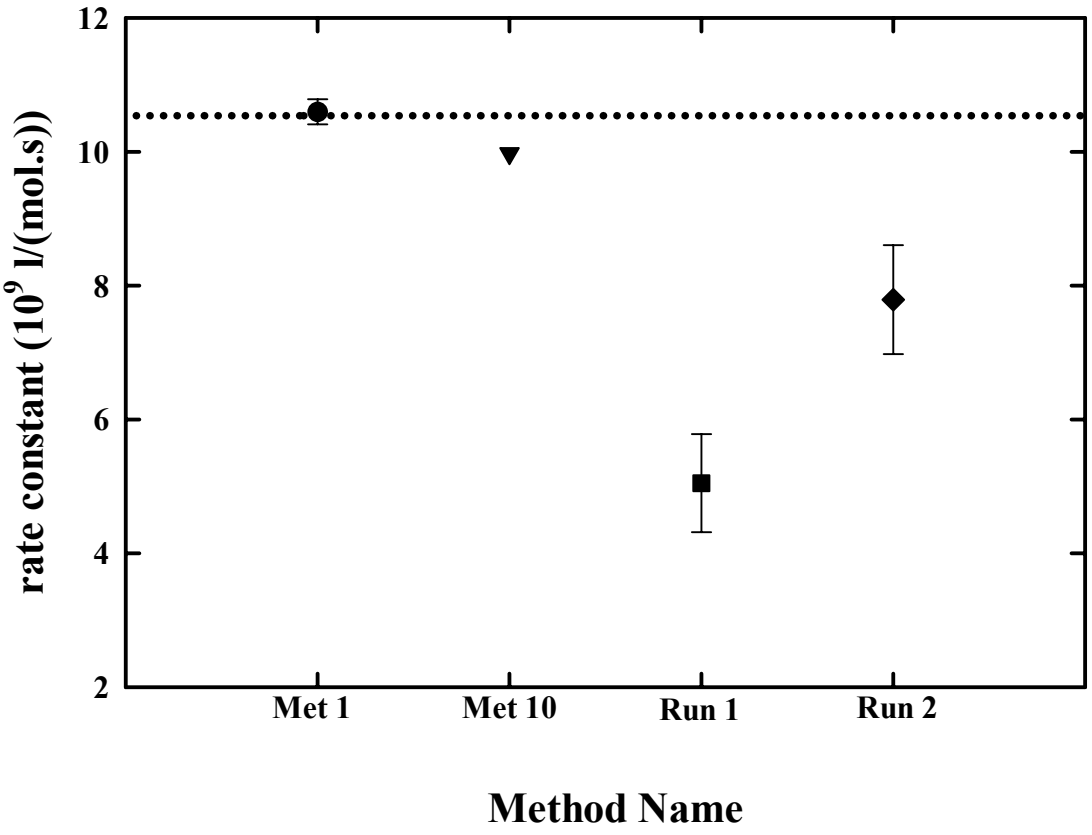


**Figure 5.14.** Comparison of the rate constant, *k*, for the structural diffusion of a proton in bulk water implementing different local equilibration methods in Trials 1 and 2 at 300 K. Dotted line refers to the experimental *k* (Ref. 51).

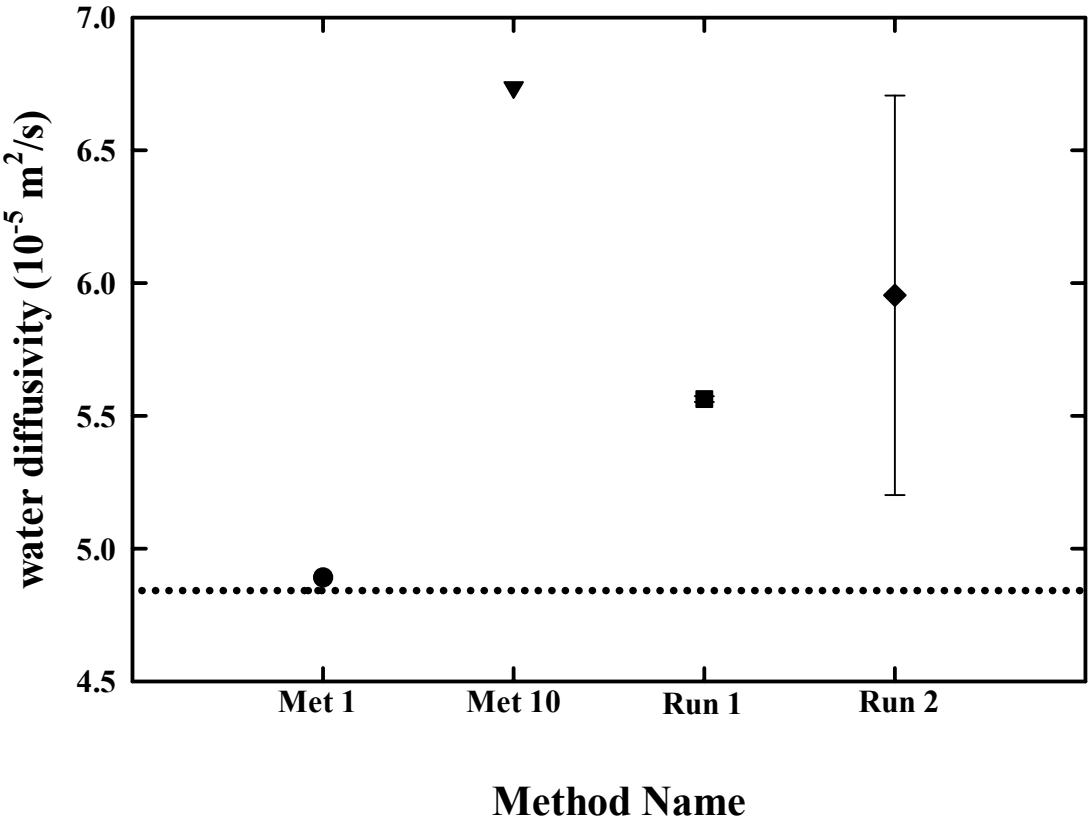


**Figure 5.15.** Water diffusivities in bulk water system at infinite dilute concentration as a function of local equilibration scheme in Trials 1 and 2 at 300 K. Dotted line refers to the diffusivity of pure TIP3P water model (Ref. 46).

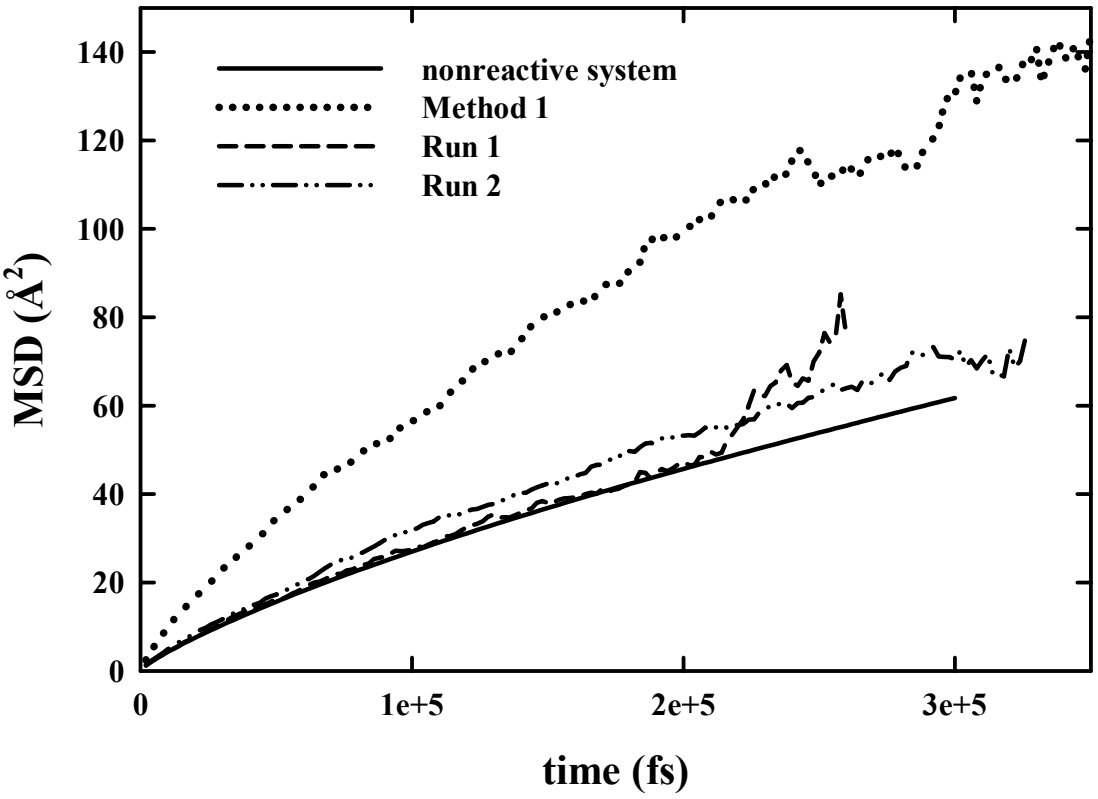


**Figure 5.16.** Comparison of MSDs for $\lambda = 9$ using various local equilibration schemes. Method 1 is described in Table 5.4 and has $w_2 = 10$, Run 1 – Method 1 with $w_2 = 100$, Run 2 – Method 10 described in Table 5.4 with $w_2 = 500$. MSD from a reactive system is expected to match that of nonreactive system.

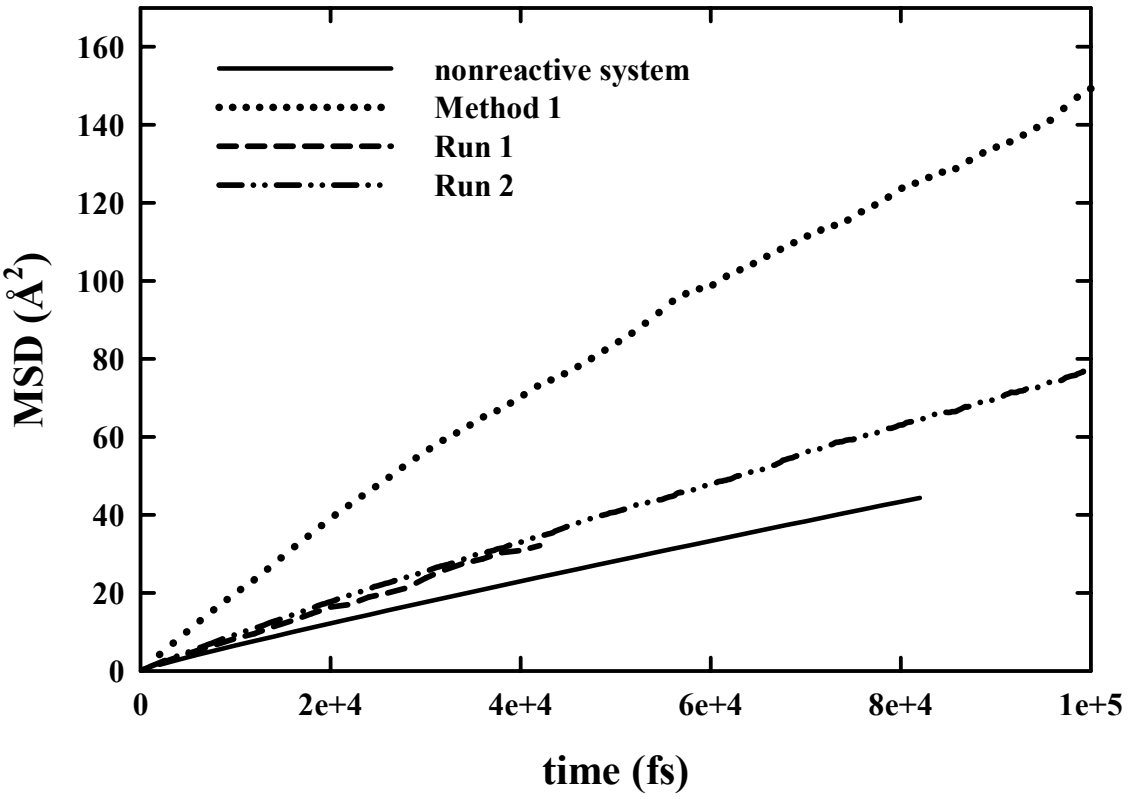


**Figure 5.17.** Comparison of MSDs for λ = 22 using various local equilibration schemes. Method 1 is described in Table 5.4 and has $w_2$ = 10, Run 1 – Method 1 with $w_2$ = 100, Run 2 – Method 10 described in Table 5.4 with $w_2$ = 500. MSD from a reactive system is expected to match that of nonreactive system.

# CHAPTER 6

# Conclusions

In this final part, the conclusion from each chapter is summarized, and then the overall aspects of the current achievement are presented, followed by some future proposed work.

## 6.1 CHAPTER SUMMARIES

Chapter 2 examines the structural and transport properties of $H_2O$ and $H_3O^+$ ions at the interface of a Nafion polymer electrolyte membrane (PEM) and a water vapor phase through the use of molecular dynamics (MD) simulation at the water contents of 5%, 10%, 15% and 20% by weight. The vehicular diffusion coefficients of $H_3O^+$ ions and $H_2O$ as components parallel and perpendicular to the interface are reported. In the interfacial region, for $H_3O^+$ ions, we find that the component of the vehicular diffusivity parallel to the interface is largely unchanged from that in the bulk hydrated membrane, but the component perpendicular to the interface has increased, due to local decrease in density. We find similar behavior with $H_2O$ in the interfacial region. Based on these diffusivities we concluded that there is no observable additional resistance to mass transport of the vehicular component of $H_2O$ and $H_3O^+$ ions at the interface. In terms of structure at the interface, we find that there is a decrease in the fraction of fully hydrated hydronium ions. This translates into a lower probability of formation of Eigen cations, which are necessary for structural diffusion. A region of water depletion in the membrane near the vapor interface is also observed. Finally, we observe that the $H_3O^+$ ions display a preferential orientation at the interface with their oxygen atoms exposed to the vapor phase.

Chapter 3 presents a model that incorporates the structural diffusion of a proton into a classical MD simulation using a reactive molecular dynamics (RMD) algorithm. The transition state for proton transfer obtained from *ab initio* calculations is mapped onto a set of geometric and energetic triggers to describe the structural diffusion of the proton in the simulation. Numerical values of these triggers are parameterized to satisfy the experimental values of rate constant and activation energy in order to capture the molecular and macroscopic features of structural diffusion. The algorithm partitions the structural diffusion of a proton into three steps: (i) satisfaction of the triggers, (ii) instantaneous reaction and (iii) local equilibration. The final step ensures that the ending point of the reaction provides the correct structure and heat of reaction. Hence, the reactivity is incorporated by the algorithm rather than through the development of a reactive potential. We have applied this scheme to study proton transport in

bulk water and hydrochloric acid (HCl) solutions. Total charge diffusion along with the structural and vehicular decomposition is studied as a function of temperature (280–320 K). The two components are found to be uncorrelated and the structural diffusion contributes 60–70% of the total charge diffusion in bulk water. The method is applied to HCl solutions (0.22–0.83 M) to study the effect of concentration on proton transport. The reduction in the total diffusivity of the charge with an increase in concentration is due to the reduction in structural diffusion.

Chapter 4 studies the effects on the structural and transport properties of a proton in water confined in carbon nanotubes (CNTs) of radii ranging from 5.42 to 10.85 Å by employing a recently devised RMD scheme. The formation of distinct layers is observed in the computed radial density profile of water. Affinity of $H_3O^+$ ions towards the tube/water interface and its preferential orientation with the oxygen atom protruding towards the wall is observed. The axial water diffusivity is found to decrease with increasing confinement of water. Analysis of the axial charge diffusivity and its two components (structural and vehicular) are also performed. Confinement is found to have a more significant effect on structural diffusion than on vehicular diffusion. The axial vehicular component of the charge diffusivity in the nanotube of radius 10.85 Å, is found to be equal to the value computed in bulk water while structural component was 12% of the value observed in bulk water, which resulted in a total charge diffusivity of 42% of the diffusion in bulk water. The confined geometry affects the system energetically and perturbs the solvation structure around the proton from that found in bulk water. The RMD algorithm, which defines the occurrence of a proton transfer reaction based on the satisfaction of a set of triggers, identified the energetic factor to be greatly responsible for the decreased structural diffusion of a proton.

Chapter 5 investigates the transport properties of water and protons in Nafion with an equivalent weight of 1144 using a recently developed RMD algorithm. The algorithm takes input from both quantum mechanical and macroscopic models of structural diffusion of a proton and incorporates them in a classical MD simulation via three steps. Previously the algorithm has qualitatively captured the individual effect of temperature, confinement and acidity on the structural diffusion of a proton and is applied to Nafion 1144, which contains an aqueous domain influenced both by acidity and confinement at 300 K for $\lambda = 6$, 9, 15, and 22. We have modeled the structural diffusion of protons via a mechanism similar to that observed in bulk aqueous

systems. The reactivity of the structural diffusion is measured in terms of a rate constant and is found to increase with hydration level. The contribution of the structural and vehicular components and their correlation to the total charge diffusion are discussed. The components are found to be anti-correlated with the correlation decreasing with an increase in water content. The total charge diffusivity is higher than the experimentally measured values due to a high vehicular component that resulted from insufficient local equilibration. A similar increase is reflected in the water diffusivity of current system when compared to the diffusivities from classical MD simulation. We have also analyzed various local equilibration schemes to lower the water diffusivity and identified that the minimization of energy plays a much more significant role in the re-establishment of a stable hydrogen bond network after reaction.

## 6.2 SIGNIFICANCE

In conclusion, the present work is focused on modeling proton transport in perfluorosulfonic acid PEM. It is approached as two tasks. The first task is to understand the complex heterogeneous morphology in a PEM. An atomistic description of a membrane/vapor interface using classical MD simulation is modeled for this purpose. The selection of the above system also aids in the investigation of the presence of any intrinsic resistance to the transport of $H_2O$ and $H_3O^+$ ions at the interfacial region. Moreover, an understanding of the molecular-level structure and dynamics of protons at the electrode/electrolyte interface will offer new insights into the mechanisms that control the important electrochemical and electrocatalytic processes which ultimately dictate the performance of a fuel cell. From this work, we find enhanced vehicular diffusion of both water and hydronium ions perpendicular the membrane/vapor interface at all water than the diffusivities in bulk membrane, implying there is no observable additional resistance to the vehicular diffusion. This might be attributed to the density gradient that exits in the direction perpendicular to the interface.

The second task is to develop an algorithm to model proton transport that occurs as a combination of vehicular and structural diffusion. The structural diffusion of a proton cannot be captured by classical mechanics since it involves dynamic rearranging of covalent and hydrogen bonds. Therefore, we have developed a new RMD algorithm to implement the reactivity involved in the structural diffusion in a classical MD simulation. The proton transport through

aqueous domains in PEM is governed by acidity of the terminal acid group in the side-chain and confinement due to aqueous region which are a few nanometers in dimension. To understand better the effect of these factors on proton mobility in PEM and to confirm the validity of the algorithm, the RMD scheme was applied to systems in which the acidity and confinement can be independently varied. For this purpose, three systems following similar mechanisms but with different physical environment has been identified: (1) bulk water which has influence of neither confinement nor acidity, (2) aqueous HCl which has only the influence of acidity, (3) water confined in CNTs which has only the influence of confinement. The parameters involved in the RMD algorithm are reaction specific, *i.e.*, the methodology and parameters can be extended to any system as long as the reaction follows the exact mechanism (or transition state) irrespective of physical conditions and environment. The algorithm successfully captured the qualitative features of the structural diffusion in all the above three systems and was applied to model the structural diffusion of proton in PEM. By being able to model proton transport in fuel cell membranes it is possible to understand the relationship between the elementary acts of proton transport in individual pores and the nanostructure of the humidified membrane

From this work, we observe that increasing acidity in bulk HCl solutions causes a reduction in the total diffusivity of the charge, as has been observed experimentally [1,2]. Furthermore, these simulations add to our understanding because they show that the majority of the decrease is associated with structural diffusion. The vehicular component is constant irrespective of the change in the given range of concentration. The two components remain uncorrelated in bulk systems. We also observe that increasing confinement of water in CNTs results in a reduction in the total diffusivity of the charge, as has been observed from EVB simulations [3]. These simulations help us understand the proton transport processes better because they again show that the majority of the decrease is associated with structural diffusion. It is only in very small pores that the vehicular component begins to decrease. The structural and vehicular components remain uncorrelated at all degrees of confinements. When the RMD algorithm is applied to Nafion, we observe that decreasing water content in the hydrated PEM causes a reduction in the total diffusivity of the charge, as has been observed experimentally [4]. These simulations offer insight into the proton transport mechanisms and demonstrate that the reduction in the total charge diffusivity of the charge is contributed to the reduction in both

structural and vehicular diffusion. The vehicular component that is not so sensitive to acidity (in the range 0.22–0.84 M) and confinement (for CNT of radius > 8.42 Å) unlike the structural component showed a steady decrease in Nafion with decrease in hydration level. The two components are negatively correlated at all water contents because as structural component tends to move the proton towards the sulfonate group, the vehicular tends to move them away from the sulfonate group. The negative correlation decreases as they approach bulk-like behavior (increase in water content). The charge diffusion in Nafion is different from the bulk HCl solution and water confined in CNTs in terms of the acid group, confinement in an irregular geometry and an additional factor of connectivity of the aqueous domains.

All these studies will eventually provide guidance leading to the (i) synthesis of novel PEMs with superior characteristics like high ionic conductivity, good chemical stability, mechanical integrity, improved durability, and the capability to operate at high temperatures without the external humidification of the incoming reactant gases, (ii) manufacture of PEM fuel cells with improved performance that will enable the large scale commercialization, and (iii) recognition of proton transport mechanism at molecular scale.

## 6.3 FUTURE WORK

The success of the current work has enabled us to foresee the following future work. First, the RMD algorithm can be used to model the structural diffusion of proton in the nanoscale domains within the membrane enabled by the "Zundel-like" and "Eigen-like" structures formed with the oxygen atoms of the sulfonate groups instead of depending only on the neighboring water molecules as in bulk aqueous systems. This can lead to the basic understanding of the individual contributions of the vehicular mechanism, structural diffusion via bulk-like mechanism, and structural diffusion by surface-like mechanism to the overall proton transport in a PEM. Therefore, the design of the future polymer membrane materials can be based on water uptake and enhancing the particular mechanism contributing the most to the proton conductivity.

Second, proton transport in various interfacial regions between the electrode and electrolyte of a membrane electrode assembly such as the membrane/vapor interface discussed in chapter 2 can be studied by employing the RMD algorithm. An understanding of the structure and dynamics of protons in the multi-phase electrode/electrolyte interface consisting of PEM,

vapor, water, electrodes, and catalyst surface will aid in the development of a predictive, continuum-level model of PEMFC operation.

Third, the RMD algorithm is generalized for all chemical reactions and has been proven effective (qualitatively) in recognizing the surrounding and physical parameters of the system. Therefore, the application of the approach can be extended into a variety of research fields including complex biological systems (enzymes and proteins) because it is based on the classical molecular mechanics and avoids the parameterization involved in defining the reactive potentials.

# References

[1] Cornish, B. D. and Speedy, R. J., *J. Phys. Chem.* **88**, 1888 (1984).

[2] Dippel, T. and Kreuer, K. D., *Solid State Ionics* **46**, 3 (1991).

[3] Brewer, M. L.; Schmitt, U. W. and Voth, G. A., *Biophys. J.* **80**, 1691 (2001).

[4] Kreuer, K. D., *Solid State Ionics* **97**, 1 (1997).

# Vita

Myvizhi Esai Selvan was born in Madurai, Tamil Nadu (India) on October 4, 1983. She grew up in the same city and did her schooling in VMJ Higher Secondary School. After graduating high school in 2001, she went to Anna University, Chennai, Tamil Nadu (India). She received a Bachelor of Technology Degree in Chemical Engineering in 2005. In January 2006, she was admitted into the Ph.D. program in the Department of Chemical and Biomolecular Engineering at the University of Tennessee, Knoxville, TN (USA) and accepted assistantship at the Computational Materials Research Group.

Myvizhi Esai Selvan completed her doctorate in Chemical Engineering at the University of Tennessee, Knoxville, TN, in December, 2010.